

COMPACT ACTUATION THROUGH
MAGNETORHEOLOGICAL FLOW CONTROL AND
RECTIFICATION OF MAGNETOSTRICTIVE VIBRATIONS

A Thesis

Presented in Partial Fulfillment of the Requirements for
the Degree Master of Science in the
Graduate School of The Ohio State University

By

David T. Nosse, B.S.

* * * * *

The Ohio State University

2005

Master's Examination Committee:

Dr. Marcelo Dapino, Adviser

Dr. Krishnaswamy (Cheena) Srinivasan

Approved by

Adviser

Graduate Program in
Mechanical Engineering

© Copyright by

David T. Nosse

2005

ABSTRACT

There is currently a need for compact actuators capable of producing large deflections, large forces, and broad frequency bandwidth. In all existing active or “smart” materials, large force and broadband responses are obtained at small displacements and methods for transmitting very short transducer element motion to large deformations need to be developed. This research addresses the development of a hybrid actuator which provides virtually unlimited deflections and large forces through magnetorheological (MR) flow control and rectification of the resonant mechanical vibrations produced by a magnetostrictive Terfenol-D pump. The device is a compact, self-contained, fly-by-wire unit which is capable of producing large work output concurrently with stiffness and damping control. To achieve large output force, hydraulic advantage is created by implementing a driven piston diameter that is larger than the drive piston. Since the optimal pump operating range occurs at high speeds in the low kHz range, a fast-acting MR fluid valve is required. This research therefore includes the design and development of a magnetorheological fluid valve, Terfenol-D fluid pump, various experimental setups, and a system-level model. Experimental testing and model results validate the hybrid actuator concept and highlight the fundamental properties and issues of the actuator.

I dedicate this to my late Godmother, Lynn Nosse.

ACKNOWLEDGMENTS

The success of this research is attributed to the helpful assistance received from many individuals.

I thank the project adviser and Master's Examination Committee member, Prof. Marcelo Dapino, for his guidance, reliability, support, and for the great research opportunity which I feel has been second to none. I also want to thank the second member of my Master's Examination Committee, Prof. Cheena Srinivasan, for inquisitive questions and comments on the content of this research.

I wish to thank my family and friends whom have loved and supported me. Thank you Mom, Dad, Kelly, Lindsay, and Amy for everything you helped me become. You motivate me to accomplish the extraordinary.

I would also like to thank all my lab colleagues throughout the two year span of this project for their advice and friendship. In particular, thank you Anthony Mortensen for your mechanical design thoughts, DataPhysics instruction, and music. Thank you Brett Burton for your help during the project transition phase from an undergraduate project to this Masters Thesis. Thank you Mike Rupinsky for your experimentation help.

I wish to acknowledge my roommates, Steve Martisauskas and Scott Wolfer, for there support, friendship, and for going through this experience with me. Thank you Steve for your instruction and assistance with LabVIEW.

I am grateful to the Mechanical Engineering department for providing the instruction, facilities, and resources which assisted this research. I thank Prof. Mark Walter for the open use of the MTS machine. I thank Gary Gardner and Keith Rogers for fulfilling

several machining tasks, without whom component fabrication would have been tedious and cumbersome.

I would also like to thank the funding sources of this research. Thank you DARPA for the project grant. Thank you Delphi for the magnetorheological fluid donation. Thank you Etrema for the use of a Terfenol-D transducer.

VITA

March 8, 1980 Born - Cleveland, Ohio, U.S.A.

June 2003 B.S. Mechanical Engineering with Dis-
tinction, The Ohio State University

2003-present Graduate Research Associate, The
Ohio State University

PUBLICATIONS

D.T. Nosse, M.J. Dapino, “Compact Actuation Through Magnetorheological Flow Control and Rectification of Magnetostrictive Vibrations.” *Proceedings of SPIE Smart Structures and Materials*, Paper #5764-31, San Diego, CA, March 2005.

D.T. Nosse, M.J. Dapino, “Compact Actuation Through Magnetorheological Flow Control and Rectification of Magnetostrictive Vibrations.” *Proceedings of ASME*, Paper #61534, Anaheim, CA, November 2004.

B. Burton, D.T. Nosse, M.J. Dapino, “High Power Density Actuation Through Terfenol-D Resonant Motion and Magnetorheological Flow Control.” *Proceedings of SPIE Smart Structures and Materials*, Vol. 5390, pp. 104–115, San Diego, CA, March 2004.

FIELDS OF STUDY

Major Field: Mechanical Engineering

Studies in Smart Materials and Structures: Prof. Marcelo Dapino

TABLE OF CONTENTS

	Page
Abstract	ii
Dedication	iii
Acknowledgments	iv
Vita	vi
List of Tables	x
List of Figures	xii
Chapters:	
1. Introduction	1
2. Background Information	3
2.1 Motivation for Research	3
2.2 Project Objectives	5
2.3 Smart Materials	6
2.3.1 Overview	6
2.3.2 Magnetorheological Fluid	8
2.3.3 Terfenol-D	18
2.4 Motion Amplification Devices	23
3. Hybrid Actuator: Concept, Design, and Construction	27
3.1 Principle of Operation	27
3.2 Challenges	30
3.3 Actuator Design	31
3.3.1 Magnetorheological Fluid Valve - Design #1	31
3.3.2 Magnetorheological Fluid Valve - Design #2	34
3.3.3 Unidirectional Terfenol-D Fluid Pump	40

4.	Experiments	44
4.1	Fluid Valve Testing Using Manual Pump	44
4.1.1	Objective and Construction Details	44
4.1.2	Non-activated Fluid Valve Results	45
4.1.3	Activated Fluid Valve Results	47
4.2	Fluid Valve Testing with Output Piston and Automated Pump	49
4.2.1	Objective and Construction Details	49
4.2.2	Solenoid Timing	53
4.2.3	Input Waveform	54
4.2.4	Automated Solenoid Control	57
4.3	Variable Valve Resistance Measurements	59
4.3.1	Objective and Construction Details	59
4.3.2	MR Fluid Valve #1 Resistance	60
4.3.3	MR Fluid Valve #2 Resistance	65
4.4	Characterization of Unidirectional Magnetostrictive Pump	68
4.4.1	Objective and Construction Details	68
4.4.2	Terfenol-D Transducer Resonance	70
4.4.3	Operating Bias Pressure	72
4.4.4	Pump Performance	73
5.	Modeling	76
5.1	System Model #1 - Force Balance	76
5.1.1	Model #1 Development	76
5.1.2	Model #1 Results	80
5.2	System Model #2 - Volume Stored	83
5.2.1	Model #2 Development	83
5.2.2	Model #2 Results	87
6.	Concluding Remarks	89
6.1	Summary of Findings	89
6.2	Future Work	90
Appendices:		
A.	Actuator Component Design Details	92
A.1	MR Fluid Valve Design #1	92
A.2	MR Fluid Valve Design #2	101
A.3	Unidirectional Terfenol-D Fluid Pump Design	108

B.	Program Details	114
B.1	Labview	114
B.1.1	MTS and Solenoid Controlled Actuation Program	114
B.1.2	Variable Resistance Measurement Program	117
B.1.3	Terfenol-D Pump Controlled Actuation Program	117
B.2	Finite Element Modeling	120
B.3	Matlab	124
B.3.1	System Model #1 Details	124
B.3.2	System Model #2 Details	131
	Bibliography	139

LIST OF TABLES

Table	Page
2.1 Property comparison of MR and ER fluids [5]	11
4.1 Output piston displacement (in) from a ramp input of 2 in magnitude in the negative direction at a rate of 3.0 in/s.	54
4.2 Output piston displacement (in) from a ramp input of 2 in magnitude in positive direction at a rate of 3.0 in/s.	54
4.3 Net displacement produced by the output piston from a sinusoidal input piston waveform ($A = 0.5$ Hz, 2 in p-p amplitude, $B = 1.0$ Hz, 2 in p-p amplitude).	56
4.4 Net displacement produced by the output piston using the control strategy of left solenoid “on” for a negative MTS direction input and both solenoids “off” for a positive MTS direction, for a sinusoid input piston waveform (2 in p-p amplitude) of various frequencies.	56
4.5 Average resistance measurements ($\text{lbf}\cdot\text{s}/\text{in}^5$) of MR fluid valve #1 for fixed annular gap of 0.030 in, axial gap, solenoid voltage, and flow direction (F1, F2).	64
4.6 Average resistance measurements ($\text{lbf}\cdot\text{s}/\text{in}^5$) of MR fluid valve #1 for a modified fixed annular gap of 0.125 in, axial gap, solenoid voltage, and flow direction (F1, F2).	64
4.7 Average resistance measurements ($\text{lbf}\cdot\text{s}/\text{in}^5$) of MR fluid valve #2(A) for fixed annular gap of 0.030 in, axial gap, solenoid voltage, and flow direction (F1, F2).	66
4.8 Average resistance measurements ($\text{lbf}\cdot\text{s}/\text{in}^5$) of MR fluid valve #2(B) for fixed annular gap of 0.030 in, axial gap, solenoid voltage, and flow direction (F1, F2).	66

B.1	Magnetic properties assigned to material definitions in FEMM.	121
B.2	System inputs for model #1.	126
B.3	Relative approximations for variable left valve resistances. The right valve is similar.	130
B.4	Spring and damper (rigid housing constraint) look-up table values.	130
B.5	System inputs for model #2.	132
B.6	Variable left valve resistance look-up table index numbers based on flow direction and solenoid voltage.	132
B.7	Relative approximations for variable left valve resistances. The right valve is similar.	132

LIST OF FIGURES

Figure	Page
2.1 Picture of MR fluid as a function of applied magnetic field; (a) inactivated or no magnetic field state and (b) activated with a magnetic field (Lord Co.)	7
2.2 Schematic of SMA operation and material phases. The original, undeformed shape can be plastically deformed through mechanical forces. Application of heat returns the SMA to the memorized, undeformed shape.	9
2.3 Sequence showing the alignment of iron particles with respect to an external magnetic field (Lord Co.).	9
2.4 Comparison between Newtonian (unactivated MR fluid) and non-Newtonian viscoplastic (activated MR fluid) shear stress versus shear rate behavior. .	11
2.5 Properties of MRF-132AD (Lord Co.) magnetorheological fluid (a) magnetic flux B versus magnetic induction H , (b) shear stress versus shear rate with no applied magnetic field, and (c) yield stress versus magnetic induction H .	13
2.6 Two common flow-modes of MR fluid devices.	15
2.7 The <i>MagneRideTM</i> suspension implemented in select General Motors vehicles.	16
2.8 MR damper schematics for (a) small-scale/automotive and (b) large scale/seismic applications [15].	17
2.9 Schematic of magnetostriction stages; (a) paramagnetic state above T_c , (b) magnetic state below T_c with no field H , (c) reversible magnetic moment alignment with an applied magnetic field H , and (d) irreversible domain wall rotation from a saturating magnetic field H	18
2.10 Terfenol-D response (a) relative magnetization M/M_s and (b) the magnetostriction strain ε produced by a magnetic field H	20
2.11 Terfenol-D sonar transducers (a) flextensional type, (b) square-ring type, (c) Tonpilz type [8], and (d) hybrid (Terfenol-D and Piezoelectric) type [3].	21

2.12	Terfenol-D rotary transducers (a) elliptical rotary motor [1] and (b) rotary motor [30].	22
2.13	Schematic of inchworm operation cycle producing an 11 μm step of actuation [23].	24
2.14	Schematic of piezoelectric-hydraulic pump with active unimorph disk valves to control flow at inlet and outlet [19].	25
2.15	Schematic of complete actuator design consisting of a piezoelectric fluid pump and magnetorheological fluid valves [35].	26
3.1	(a) Hybrid MR fluid-magnetostrictive actuator. In (b), the drive piston connected to the Terfenol-D pump pushes the fluid through the left valve half and subsequently pushes the driven piston on the load end (left coil active), while the right valve half remains closed. In (c), the drive piston retracts while the MR fluid recirculates through the right half valve (right coil active). The driven piston stays fixed until step (b) starts again and the sequence is repeated. Permanent magnets inside the conical heads provide a bias force on the MR fluid.	28
3.2	Cutaway solid model of the MR fluid valve. The grooves in the conical valve ends are fitted with coils for enhanced flexibility compared with the initial concept, which employs permanent magnets.	32
3.3	Picture of (a) movable valve piece and removable housing piece and (b) the main housing piece of the MR fluid valve device #1.	32
3.4	Magnetic finite element analysis (FEMM V.3.4) result showing the routing of magnetic flux density lines perpendicular to the flow direction.	33
3.5	Illustration of MR fluid valve gap terminology.	34
3.6	Magnetic finite element analysis of non-implemented valve design (a) axis-symmetric model with external solenoid and permanent magnet for (b) the solenoid “off” case and (c) solenoid “on” case. Magnetic field is always present across gap.	36
3.7	Magnetic finite element analysis of MR fluid valve design #2 (a) axis-symmetric model with external solenoid for (b) the solenoid “on” case. The solenoid “off” case is exactly zero at all locations.	37

3.8	MR fluid valve design #2 (a) cutaway view of a solid model and (b) the actual fluid valve. Coil stacks were relocated to the inner housing surface to allow significant size reduction of the movable valve piece.	38
3.9	Picture of coil stack within a steel sleeve.	39
3.10	Picture comparing the size of valve design #1 and design #2. Design #2 has a 570 percent smaller volume.	39
3.11	Unidirectional Terfenol-D fluid pump design (a) solid model and (b) the actual Terfenol-D fluid pump. The Terfenol-D transducer was supplied by Etrema Products, Inc. (Ames, Iowa) as in-kind contribution.	41
3.12	Illustration showing the two stages of operation for the unidirectional Terfenol-D fluid pump design using directional check valves; (a) pump refill and (b) output flow stage.	42
3.13	Solid model of a typical Terfenol-D transducer design.	43
4.1	(a) Actual and (b) schematic of the experimental setup used for testing of an early double-sided MR fluid valve.	46
4.2	MR fluid valve motion from an oscillatory pressure and flow, but with no solenoid input voltage. Both initial valve positions, left closed (=0) and right closed (=1), were tested twice for repeatability.	47
4.3	(a) MR fluid valve motion under an oscillatory hydraulic input and a 20 V solenoid input voltage. (b) Recorded pressure from the right valve inlet and (c) recorded pressure from the left valve side from a similar run.	48
4.4	MR fluid valve (a) motion under an oscillatory hydraulic input and a 5 V solenoid input voltage and (b) recorded pressure from the right valve inlet.	49
4.5	Experimental setup with automated inputs used for controlled actuation.	51
4.6	Illustrations of (a) automated input piston experimental setup with double-sided valve and output piston, (b) actuation step of operation, and (c) the refill step needed to complete one actuation cycle. A positive input displacement produces flow F_2 and negative input displacement produces flow F_1	52
4.7	Actuation results (a) control strategy for 5 V dc solenoid input and negative (F_1) input piston loading (b) line pressures (c) valve location (-0.2 = left valve closed, +0.2 = right valve closed), and (d) output piston position.	58

4.8	Actuation results (a) control strategy - no solenoid inputs for either loading, (b) line pressures, (c) valve location (-0.2 inch is valve not in series with output piston closed), and (d) output piston position.	59
4.9	Illustration of setup used to determine MR valve resistance for (a) design #1 and (b) design #2. Arrows depict the two flow directions, F1 and F2, based respectively on negative and positive MTS input direction.	61
4.10	(a) Input waveform recorded with MTS machine's position transducer, and (b) the calculated input flow rate for resistance testing of MR fluid valve device #1.	62
4.11	MR fluid valve (#1), left valve, 10 V, 0.125 in gap resistance test data; (a) line pressure, (b) pressure differential, and (c) resistance data.	63
4.12	MR fluid valve device #2, 10 V input, 0.055 in axial gap resistance testing data; (a) input flow rate, (b) line pressures, (c) pressure differential, and (d) resistance.	67
4.13	Projected resistance fits to data for MR fluid valve #2 for (a) valve (A) and (b) valve (B).	68
4.14	(a),(b) Experimental setup used to characterize the performance limits of the unidirectional Terfenol-D fluid pump.	70
4.15	Frequency response for acceleration per current of Terfenol-D transducer (a) magnitude and (b) phase. This response shows resonance at 2660 Hz. The associated input current spectral density (c) magnitude and (d) phase. . .	72
4.16	Unidirectional Terfenol-D pump performance for varying pressure bias. . .	73
4.17	Performance of unidirectional Terfenol-D pump for (a) constant 5.8 V rms input, (b) constant 7.15 V rms input, and (c) constant 8.5 V rms input. . .	74
4.18	Performance of unidirectional Terfenol-D pump for (a) constant 30 Hz input, (b) constant 50 Hz input, (c) constant 60 Hz input, (d) constant 70 Hz input, and (e) constant 90 Hz input.	75
5.1	System-level representation of experimental setup using hydraulic input piston and double-sided valve design #1, without an output piston. The fluid flow is modeled by equivalent resistance and inductance elements.	77
5.2	Mechanical model of valve.	79

5.3	System-level model #1 output example (a) input volume flow rate, (b) input fluid pressure, (c) input voltages (solenoid “on”/“off”), (d) output valve position, (e) forces imposed on valve, and (f) the high amplitude, high frequency spring force used to simulate the motion limit imposed by rigid housing.	81
5.4	System-level model #1, comparison of actuator output with experimental data.	82
5.5	System-level representation of the experimental actuator used in model #2.	84
5.6	System-level model #2 results for (a) valve position, (b) input voltages (solenoid “on”/“off”), (c) volume flow rate, and (d) output valve position. .	88
A.1	Magnetorheological fluid valve design #1, Main assembly. An identical half is coupled to complete the double sided valve.	94
A.2	Valve housing subassembly.	95
A.3	Main housing piece (steel)	96
A.4	Main housing piece (steel), press fit and welded to previous housing piece. .	96
A.5	Removable housing end cap (steel).	97
A.6	Movabable valve piece subassembly.	98
A.7	Movable valve head piece (steel)	99
A.8	Movable valve rod piece (aluminum). Connected to head piece through set screw.	100
A.9	Schematic of solenoid stack assembly	102
A.10	Assembly of entire fluid valve (design #2)	103
A.11	Main housing (steel)	104
A.12	Housing end cap (steel)	105
A.13	Rod (steel)	106
A.14	Coupling piece (steel)	107

A.15 Solenoid stack sleeve (steel). The semi-circular cutout leaves space for the lead wires to be routed out of housing.	107
A.16 Assembly of unidirectional Terfenol-D fluid pump	110
A.17 Alignment block (aluminum). Used to rigidly hold Terfenol-D transducer and fluid chamber at a fixed spacing and inline.	111
A.18 Fluid chamber (steel). Detail-A shows the dimensions for the press-fit fluid check valves (Lee Co: CCRM1550200S and CCFM1550200S)	112
A.19 Piston (aluminum)	113
B.1 Screen capture of LabVIEW program developed and used for controlled actuation of the MR fluid valve’s solenoids.	115
B.2 Screen capture of LabVIEW interface panel that accompanies the controlled actuation program.	116
B.3 Screen capture of LabVIEW (a) program developed and used for fluid valve resistance measurements and (b) interface panel.	118
B.4 Screen capture of LabVIEW program developed for hybrid actuator control (unidirectional fluid pump).	120
B.5 Screen capture of FEMM solver boundaries.	122
B.6 Screen capture showing details of an actual FEMM model.	123
B.7 Outside program shell for system-level model #1, with 3 subprograms (Valve fluid resistance, Flow routing, and Mechanical).	125
B.8 Valve fluid resistance subprogram for system-level model #1.	126
B.9 Flow routing subprogram for system-level model #1.	127
B.10 Mechanical subprogram for system-level model #1, with 1 subprogram (damping coefficients).	128
B.11 Damping coefficients subprogram for system-level model #1, using the Bingham viscoplastic model.	129

B.12 Script file used to run Simulink program for system-level model #1 with defined coefficients	130
B.13 Outside program shell for system-level model #2, with 3 subprograms (Valve fluid resistance, Flow routing, and Valve subsystem).	134
B.14 Valve fluid resistance subprogram for system-level model #2.	135
B.15 Flow routing subprogram for system-level model #2.	136
B.16 Valve motion subprogram for system-level model #2.	137
B.17 Script file used to run Simulink program for system-level model #2 with defined coefficients	138

CHAPTER 1

INTRODUCTION

A transducer is a substance or device that converts input energy of one form into output energy of another. An engineering subdivision of transducers are actuators, or mechanisms that put something into automatic action. The automatic action can be linear or rotational, high or low force, macroscopic or microscopic displacement, continuous or discrete.

This paper presents a new class of linear actuator potentially capable of producing large deflection and large force over a broad bandwidth. Through concept development, component design and fabrication, experimental testing, and system-level modeling, a first generation actuator device was produced. The actuator is a hybrid design, consisting of two smart materials; Terfenol-D and magnetorheological (MR) fluid. Integration of these two types of active materials yields a self-contained, fly-by-wire (power delivered to the actuator through wire connections), compact actuator.

Background information is presented in Chapter 2 on the motivation for this research and for smart material properties and applications. A strong emphasis is given to magnetostrictive materials and magnetorheological (MR) fluids. Also reviewed are smart material actuators and components used in the development of our actuator.

Next, actuator concept of operation is discussed in Chapter 3. Also included are the components designed and fabricated for experimental testing and analysis. Specifically, two fluid valve devices and a fluid pump were developed and fabricated in-house.

Experimental testing and system-level modeling work were conducted concurrently, but are separated in this thesis for better clarity. All experimental work is included in Chapter 4. Objectives and results for each are presented in their respective sections. Four distinct experimental setups were sequentially constructed for testing of individual components. Testing progresses from a manual input piston to create fluid flow and pressure in Sect. 4.1 to automated flow inputs from a universal compression-tension machine in Sect. 4.2. A system-level model was created for behavior analysis and parameter identification in Chapter 5. Two variations of SIMULINK block diagrams were assembled for numerical solving. The second diagram was constructed from the general equation framework of the first model, but with significant enhancements aimed at improving stability. For both experimental testing and model simulations, data showing positive linear actuation was obtained.

To conclude, a summary of research results are presented in Chapter 6 and briefly discussed. Also, future work and ideas for project continuation are suggested.

CHAPTER 2

BACKGROUND INFORMATION

2.1 Motivation for Research

Actuators are routinely used in systems requiring automated displacement, force, rotation, and torque. Traditional actuators include, for example, DC motors, AC motors, hydraulic systems, and pneumatic systems. Varying application requirements have motivated numerous design variations and improvements. While traditional actuators are still widely acceptable for many applications, including those used in high technology fields, increasingly stringent requirements in emerging fields of application determine that traditional actuators are often no longer suitable.

In all existing smart (or active) materials, large force and broadband responses are obtained at small displacements. Methods for transmitting these very short transducer element motions to a large net displacement need to be developed. To improve actuator technology, Defense Advanced Research Projects Agency (DARPA) has sponsored the Compact Hybrid Actuator Program (CHAP) focused on the development of novel actuators possessing high power density and/or specific power, and actuation systems that exceed the specific power and power density of traditional electromagnetic devices by a factor of 10. The CHAP goals are to develop compact, efficient, high power density actuation devices with sufficient stroke length, actuation rate, operating bandwidth, and output force magnitude for implementation in new technologies.

Applications which can benefit from new actuator technologies include, among others, compact haptic interfaces, control surfaces for unmanned vehicles, actuator-based active suspension systems for heavy-duty commercial vehicles, adaptive airframes, and robotic locomotion components.

Performance and fuel efficiency of current aerospace designs can be improved with adaptive frames and components. The F-14 Tomcat military aircraft uses a mechanical linkage powered by traditional actuators to produce a variable sweep angle wing. The adaptive wing improves dynamic handling over a range of operating conditions, however the added mass and structural complexity downgrades much of the added benefits. In life-critical actuator applications, such as traditional hydraulic and pneumatic wing actuators, component and system redundancy is required to assure back-up (or “fail-safe”) operation in the event of component failure. For these reasons and others, production of the F-14 has ended. However, the attractive benefits of adaptive wings have not been abandoned. New military aircraft wing morphing technologies are being investigated through the Defense Advanced Research Projects Agency (DARPA) to create a shape changing, multi-mission aircraft [31]. In a similar fashion, the performance of helicopters can be increased with a morphing trailing edge flap on the rotor blades [24]. Specifically, rotor flap actuators can reduce rotor induced power loss [14] and provide control of dynamics from higher harmonics [13, 22]. Traditional actuators are often either too massive or unfeasible for such high acceleration and angular velocity environment.

There is a similar push by the automotive industry to improve fuel efficiency and vehicle dynamics. A new class of actuator is needed to replace the bulky hydraulic systems used for brakes and steering with a more compact, fly-by-wire design. The lack of sufficient response time has hindered the implementation of traditional actuators in active steering and active braking concepts. Removing hydraulic pumps takes more load off of the engine, resulting in greater efficiency. A more compact design can reduce vehicle weight and concentrate the

actuator in a particular location for better serviceability, opposed to having components distributed throughout the vehicle. Active suspension components (i.e. torsion bar) can increase both the handling of a vehicle and passenger safety and comfort.

For these types of applications to be justified, one needs a new class of actuator that is compact, light-weight, reliable, and capable of producing the desired stroke length, actuation rate, and output force. Otherwise, the performance increase by the adaptive frame, rotor, suspension, and numerous other applications is negated by the extra power consumption, weight, and system complexity.

2.2 Project Objectives

This research is supported by DARPA (John Main program manager) through the Air Force Research Laboratory, Space Vehicle Directorate grant FA9453-03-C-0333 (Scott Franke program monitor).

This project addresses the development of a compact, self-contained, fly-by-wire, hybrid smart material actuator which provides virtually unlimited deflections and large forces. The operation concept is presented in detail in Sect. 3.1. We expect the new hybrid actuator to provide performance similar to pneumatic actuators. Unlike pneumatic devices, however, the compression losses of the hybrid actuator are minimal since MR fluids are virtually incompressible. Furthermore, the hybrid actuator is self-contained and does not require external fluid lines and pumps. The output performance goal is to create linear actuation at a rate of 2.0 in/s (unloaded) with a maximum loaded blocking force of 3000 lbf. The actuator concept employs hydraulic advantage to amplify the force. The actuation rate and maximum loaded blocking force are scalable through adjustment of the hydraulic advantage ratio. A device capable of 4.5 in, yields a compact device with a high power density (comparable to pneumatic actuators). The total device size is dependent on the

maximum output actuation needed for a specific application. Larger output displacement ranges are scalable with a larger output piston.

2.3 Smart Materials

2.3.1 Overview

Advancements in composite and hybrid materials and solid-state physics have produced a class of materials known as “smart” materials. Alternate names include controllable, intelligent, active, adaptive, metamorphic, and compliant materials. The various scales of smart material classification range from microscopic to macroscopic and include alloys, transducers, and systems. At the functional materials level, smart materials are engineered hybrid substances which convert one form of an input energy (electrical, magnetic, thermal, mechanical) into a different output energy in a controllable manner. This description distinguishes these materials from those which are inert, but classifies smart materials as being purely reactive or instinctive, opposed to active, adaptive, and intelligent. A more holistic definition defines smart materials as those which show intelligence and life features integrated in or around it at various scales (from atomic to macroscopic) with the goal to meet stated objectives and to provide functional adaptability [6]. A brief overview of various smart materials is presented next to further define smart materials through examples.

Piezoelectric materials convert energy between the electrical and mechanical domains. Applying an electric field results in a mechanical deformation and applying a mechanical stress results in an electrical charge. Examples include Barium titanate ($BaTiO_3$), Lead zirconate titanate ($PbZrTiO_3$), Lead magnesium niobate ($PbMg_{1/3}Nb_{2/3}O_3$), and Polyvinylidene Fluoride. In their raw form, internal positive and negative ions are non-polarized and non-oriented. These materials are made active by polarizing the internal

ions by means of a large electric field at elevated temperatures (below the Curie temperature). When a stress is applied, the polarized ions are moved from material strain which creates an electrical output. Conversely, application of an electric field forces the polarized ions further into alignment creating a strain. Applications of piezoelectric materials include acceleration sensors, ultrasonic motors, vehicle yaw rate sensors, and active vibration control [32].

Magnetostrictive materials convert energy between the mechanical and magnetic domains through aligned magnetic moments. Greater detail of this material is presented in Sect. 2.3.3 as it is one of the two smart materials implemented in this study.

The second smart material used in the hybrid actuator design is magnetorheological (MR) fluid. MR fluid is a free-flowing (low viscosity) fluid that increases in fluid viscosity (thickens) through application of a magnetic field as shown in Fig. 2.1. Greater detail on this material and a similar smart material, electrorheological (ER) fluid, are presented in Sect. 2.3.2



Figure 2.1: Picture of MR fluid as a function of applied magnetic field; (a) inactivated or no magnetic field state and (b) activated with a magnetic field (Lord Co.)

Shape memory alloys (SMAs) are a class of smart materials which can undergo significant plastic deformations in the low-temperature martensitic phase, and which return the original un-deformed shape when transformed by heating to the high-temperature austenite phase. This process, known as the "shape memory effect," is illustrated in Fig. 2.2. The volume fraction of the two phases in a material depends on temperature and stress. As elevated temperatures (above the austenite transformation temperature), the SMA material has a cubic structure referred to as austenite. As the material is cooled (past the martensitic transformation temperature), atoms within the material tilt in alternating directions. This low-temperature martensitic phase maintains the same macroscopic shape as the high-temperature austenite phase. The application of a stress at low temperature plastically deforms the material through realignment of the internal martensite structure. To regain the original shape, heat should be added to the material. The shape memory effect can also produce a tensile recovery force from a pre-strained SMA [11, 32, 6]. In other words, a deformed SMA attached to two points of a structure will contract and pull from the two points upon application of heat. Examples of these materials include copper-zinc-aluminum, copper-aluminum-nickel, and nickel-titanium (or Nitinol). A current application challenge of SMA's is their low bandwidth due to the time needed to thermally cycle between the low and high temperature phases. Applications in which this limitation has been circumvented include synthetic jets, linear positioners, valves, switches, fire detectors, tunable vibration absorbers, intravenous stents, orthodontic braces, and flexible eyeglasses.

2.3.2 Magnetorheological Fluid

The class of fluids considered "controllable" are those which possess significant changes in their rheological behavior based on a direct input to the fluid. The magnitude of rheological change continuously depend on the value of the input, thus making the fluid

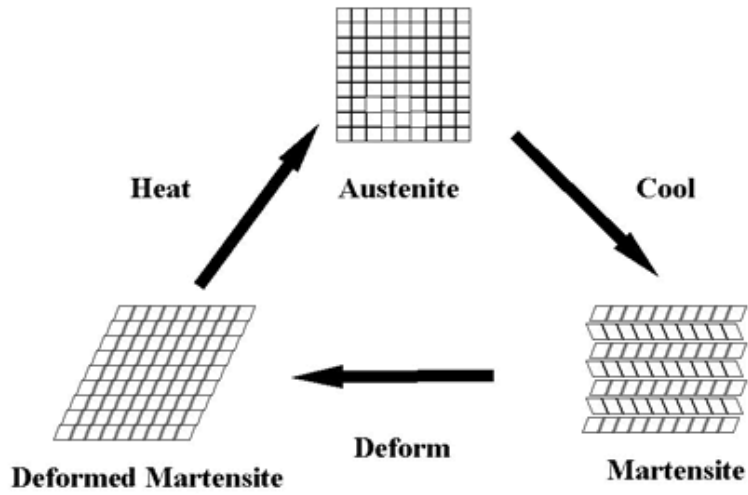


Figure 2.2: Schematic of SMA operation and material phases. The original, undeformed shape can be plastically deformed through mechanical forces. Application of heat returns the SMA to the memorized, undeformed shape.

controllable within an operating range. This section outlines two controllable fluids, justifies the selection of one for use in the hybrid actuator developed in this research, and presents fluid properties, models, and common applications.

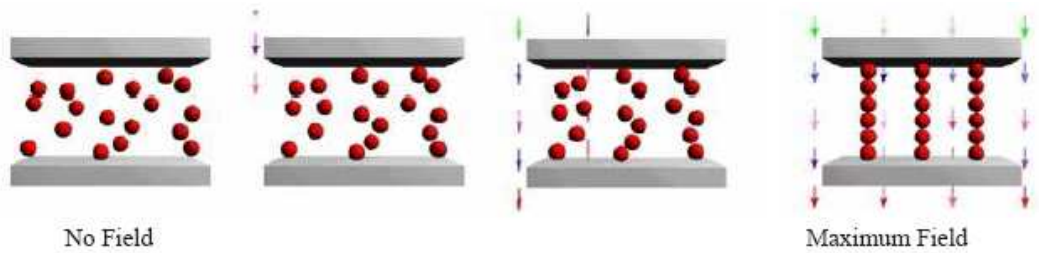


Figure 2.3: Sequence showing the alignment of iron particles with respect to an external magnetic field (Lord Co.).

In the 1940's, Willis Winslow patented electrorheological (ER) fluid, a mixture of non-conducting particles in a nonconducting liquid [12, 5]. When placed within an electric field,

the effective viscosity (measure of fluid resistance to flow) of ER fluid increases significantly within milliseconds. Furthermore, this rheological behavior is reversible as the effective viscosity increase can be reverted by removal of the electric field. Also patented in the 1940's was magnetorheological (MR) fluid. Jacob Rabinow is credited for the initial discovery and development of MR fluids [5], which are common free-flowing (Newtonian) fluids embedded with spherical, micron-sized, polarizable (iron) particles. Additional materials are often added to reduce settling of the particles. Upon application of a magnetic field the fluid viscosity increases, and similar to ER fluid, this behavior is reversible. Fig. 2.3 illustrates the controllable fluid behavior to an input field. With no applied magnetic field (or no electrical field in the case of ER fluid), the particles are randomly distributed throughout the carrier fluid. This maintains the Newtonian rheological behavior of the carrier fluid. Newtonian fluids are characterized by a linear relationship between the shear rate and shear stress by a constant viscosity η . As the field gradually increases, the particles begin to align with the field direction until the particles form columnar structures which resist the shearing motion of the carrier fluid. This mechanism thus effects a change of the fluid's effective viscosity without modifying the viscosity of the carrier fluid, as shown in Fig. 2.4.

While both ER and MR fluids exhibit similar rheological behaviors, each have specific properties which can motivate the use of one over the other. A chart comparing various material properties is shown in Table 2.1. ER fluids are energized by an electric field which can be applied through compact diodes, while MR fluids require bulky permanent magnets or solenoid coils to produce the energizing magnetic field. An advantage of MR fluids over ER fluids is that MR fluids can produce an order of magnitude higher yield strength, resulting in a significantly larger range of controllable operation. This is attributed to the high magnetic energy density established within the MR fluid being limited by the saturation of iron particles, opposed to the limitation of electric field breakdown observed in ER fluids [5, 33]. The minimum volume of activated fluid V_{min} required for an application

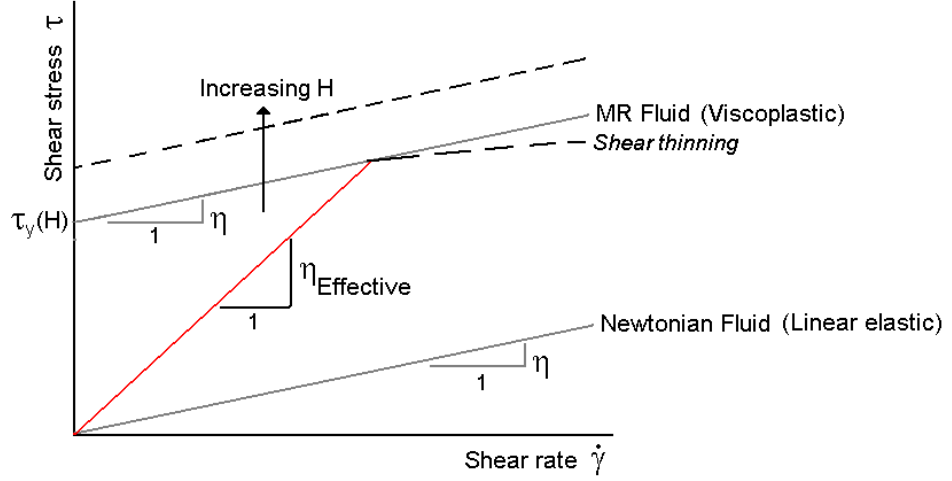


Figure 2.4: Comparison between Newtonian (unactivated MR fluid) and non-Newtonian viscoplastic (activated MR fluid) shear stress versus shear rate behavior.

Property	ER Fluid	MR Fluid
Yield Strength (with field)	2–5kPa (3–5kV/mm)	50–100kPa (150–250kA/m)
Viscosity (no field)	0.2 – 0.3Pa-s at 25C	0.2 – 0.3Pa-s at 25C
Operating temperature	-25 – +125C	-40 – +150C
Specific gravity	1 – 2.5	3 – 4
Color	Any, opaque, transparent	Brown, black, gray/opaque

Table 2.1: Property comparison of MR and ER fluids [5]

is proportional to the fluid viscosity η and inversely proportional to the square of yield stress τ_y , as shown by [5]

$$V_{min} = k\lambda W_m \eta / \tau_y^2. \quad (2.1)$$

Therefore, the minimum active volume of fluid in an MR fluid device is two orders of magnitude less than in a comparable ER device, resulting in a more compact system. MR fluids also have a broader usable temperature span in which the rheological behavior variations can be considered negligible and are less sensitive to impurities.

For this research, MR fluid was selected as the controllable fluid in order to achieve the highest possible yield strength. Property data for a commercially available hydrocarbon-based (oil carrier) MR fluid is shown in Fig. 2.5. Yield strength refers to the magnitude of stress required to produce deformation, or yielding of the material. Similar to solids, liquids can have various stages of deformation which include rigid, elastic, and plastic regions. Fig. 2.5(a) shows the magnetic induction versus magnetic field for a typical MR fluid manufactured by Lord Co. of Cary, North Carolina. Fig. 2.5(b) shows the Newtonian behavior of the inactivated MR fluid. As the shear rate is increased, the shear stress increases at a rate equal to the fluid viscosity η (≈ 0.09 Pa·s). Fig. 2.5(c) shows the large increase in yield stress as a result of an increase in applied magnetic field, where a saturation value near 45 kPa is observed.

One model for capturing the basic rheological behavior of MR fluid is the Bingham (viscoplastic) model, which is illustrated in Fig. 2.4 and modeled by the equations

$$\tau = \tau_y(H) + \eta\dot{\gamma} \quad \tau > \tau_y, \quad (2.2)$$

$$\tau = G\gamma \quad \tau < \tau_y, \quad (2.3)$$

or

$$\tau = \tau_y(H)\text{sgn}(\dot{\gamma}) + \eta\dot{\gamma}, \quad (2.4)$$

where τ_y is the field dependent yield stress, γ and τ represent the shear strain and stress, G is the complex material modulus, $\dot{\gamma}$ is the shear rate, and η is the zero field viscosity [29, 33, 16, 25]. The application of a force (shear rate) causes no deformation until the magnitude exceeds that which can be resisted by internal friction, or the yield stress, at which point the fluid yields linearly. If the force is removed, the material deformation seizes until the friction element is again overcome by a sufficient force.

Although real MR fluids exhibit some departures from the behavior predicted by the Bingham model, especially concerning the non-Newtonian behaviors often observed in these

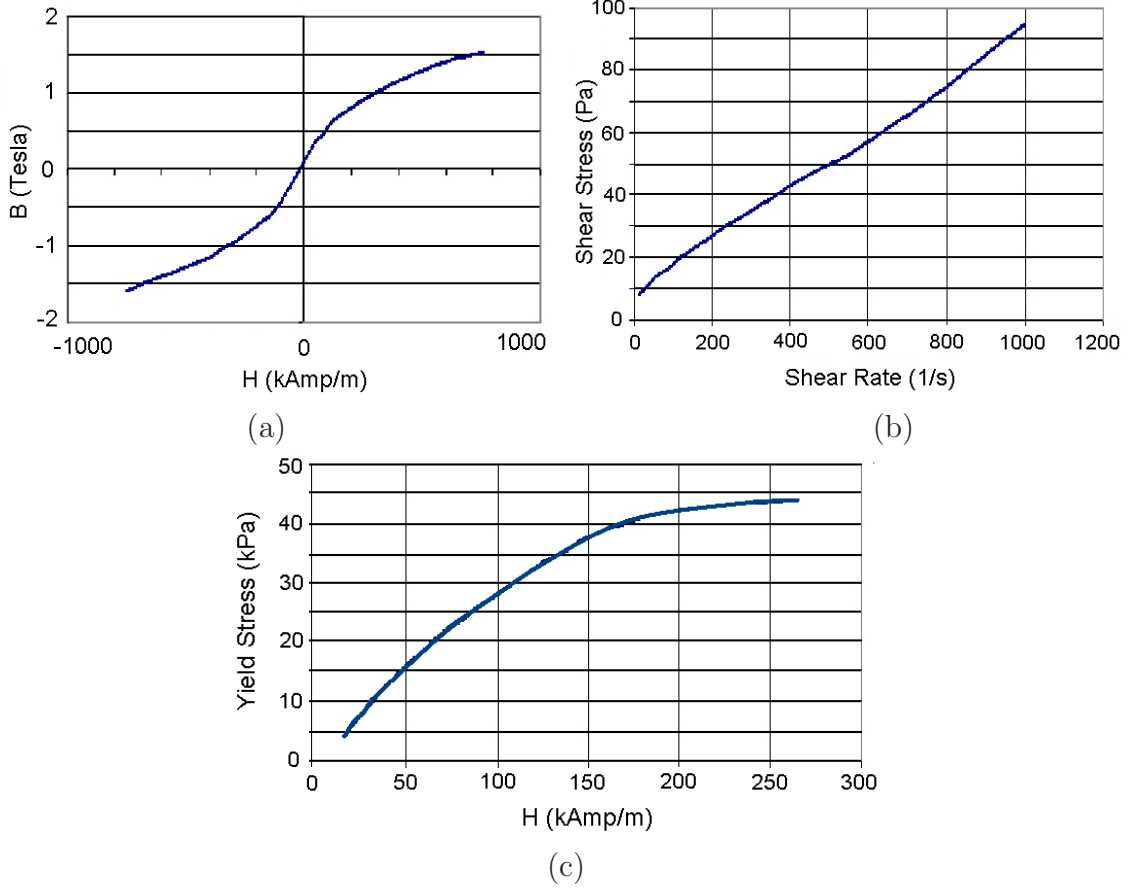


Figure 2.5: Properties of MRF-132AD (Lord Co.) magnetorheological fluid (a) magnetic flux B versus magnetic induction H , (b) shear stress versus shear rate with no applied magnetic field, and (c) yield stress versus magnetic induction H .

fluids [17], the Bingham model provides a starting point for studying the suitability of commercial MR fluids for use in various applications. MR fluid, as shown by the varying slope of Fig. 2.5(c), experiences shear thinning. Shear thinning is the continually decreasing fluid viscosity (slope) as a function of increasing shear rate. An expansion of the Bingham viscoplastic model is the the Herschel-Bulkley viscoplastic model which accounts for shear thinning, as well as shear thickening, through a power law dependant on shear strain rate [33]. The model is represented by

$$\tau = (\tau_y(H) + \eta_e \dot{\gamma}) \text{sgn}(\dot{\gamma}) \quad \tau > \tau_y, \quad (2.5)$$

where

$$\eta_e = K|\dot{\gamma}|^{(\frac{1-m}{m})}, \quad (2.6)$$

and m and K (both always positive) are fluid parameters and $m > 1$ produces a shear thinning viscoplastic model. It is noted that when $m = 1$, the Herschel-Bulkley model simplifies to the Bingham model.

In general, MR fluid is activated across a certain gap to resist or impede the flow rate. As illustrated in Fig. 2.6, there are two basic flow modes that describe how MR fluid operates within a controllable device. Flow mode, or fixed plate mode, employs a pressure differential which pushes fluid across a fixed gap. This mode is common for fluid valves, shock absorbers, and dampers. The pressure drop across the fluid gap has been approximated by the sum of a viscous component, ΔP_η common to newtonian flow, and a yield stress component $\Delta P_\tau(H)$ induced by a magnetic field. The resulting equation is

$$\Delta P = \Delta P_\eta + \Delta P_\tau(H) = \frac{12\eta QL}{g^3 w} + \frac{c\tau_y(H)L}{g}, \quad (2.7)$$

where Q is volume flow rate and geometric parameters L , g , and w are as defined in Fig. 2.6. Depending on the value of $(\Delta P_\eta/\Delta P_\tau(H))$, parameter c ranges from 2 to 3 [15]. The second basic flow mode is shear mode or moving plate mode. Common applications for this mode are clutches and brakes. This employs a relative position change between the fluid gap walls which “stretches” the fluid. The force required to slide or rotate one plate with respect to the other has been approximated with a viscous component F_η and field dependent component $F_\tau(H)$,

$$F = F_\eta + F_\tau(H) = \frac{\eta SA}{g} + \tau_y(H)Lw, \quad (2.8)$$

where S is relative plate (pole) velocity [15]. It is noted that applications can also employ a mix of both modes. A third, lesser employed mode of MR flow operation is squeeze mode. This has been used in small amplitude vibration dampers.

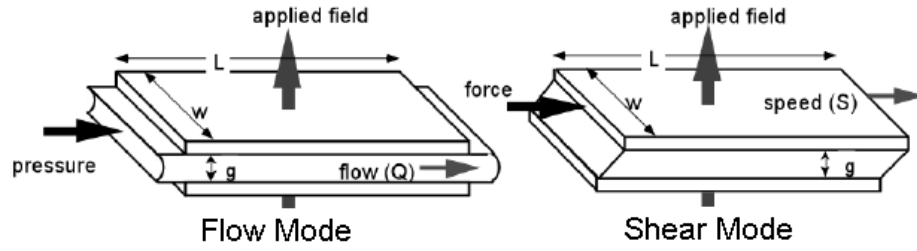


Figure 2.6: Two common flow-modes of MR fluid devices.

MR fluids have been used in many commercial applications, most of which include semiactive dampers. Passive dampers, such as rubber mounts and standard shocks, are uncontrollable past the physical design. However, in the event of power loss, they are “fail-safe” in that they can still operate as designed. Fully active dampers have minimal passive performance, thus requiring a power source for the designed operation. However, under controlled operation the active damper has a significant increase in damping performance based on its rapid adjustability to the present condition. Semi-active dampers are often preferred because they offer the adjustability of active systems when powered and the safety of passive damping without power. General Motors and Delphi Corp. have commercially implemented MR fluid in a semiactive damper shown in Fig. 2.7 for the suspension system of select high performance vehicle models, which include 2002 Cadillac Seville, 2003 50th Anniversary Corvette, 2004 Cadillac XLR and SRX, and 2005 Cadillac STS and Corvette. The automotive advantage of these semiactive damping suspensions is that they provide changes in the vehicle handling and ride comfort based on real-time information on driving conditions. In other words, during smooth, light driving conditions, a soft suspension damper is desired for a comfortable ride. During aggressive driving maneuvers a soft suspension produces excessive vehicle roll and reduction in handling. Therefore a stiff

suspension damper is desired and can be accomplished by energizing the MR fluid within the damper. A similar damper manufactured by Lord Co. is shown in Fig. 2.8(a).



Figure 2.7: The *MagneRideTM* suspension implemented in select General Motors vehicles.

Larger scale MR fluid dampers have been used in various civil engineering structures to better mitigate vibrations from large seismic activity, such as earthquakes and strong wind. Fig. 2.8(b) shows a schematic of a large-scale damper. Full-scale application examples include the cable-stayed Dongting Lake Bridge and the Tokyo National Museum of Emerging Science and Innovation building [16]. Using a similar design, MR fluid brakes and clutches have been designed to eliminate many of the moving parts associated with classical mechanical contact designs.

The ability of MR fluid to cycle between large viscosity ranges within milliseconds, has also motivated its use as fast acting fluid valve with no moving parts. By effectively activating fluid through an orifice, the viscosity change increases the flow resistance through

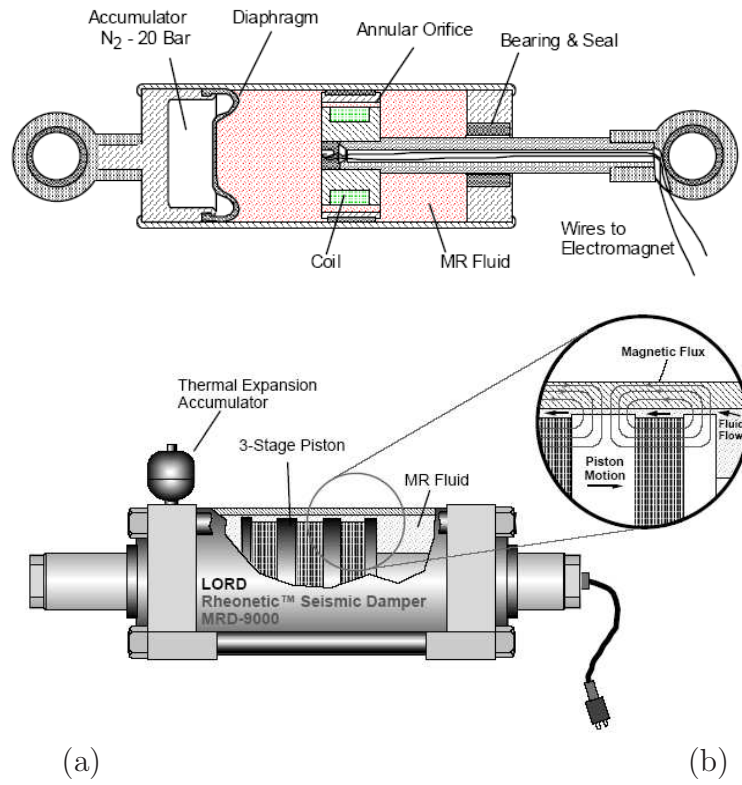


Figure 2.8: MR damper schematics for (a) small-scale/automotive and (b) large scale/seismic applications [15].

the fluid path. Ideally, the ability to create a blocked flow is desired for most valve applications so that all flow gets redirected through an alternate route. In this study, an MR fluid valve design with one moving part was developed for actuation purposes.

2.3.3 Terfenol-D

Magnetostrictive materials are metallic alloys that strain, or deform, when exposed to magnetic fields. When magnetostrictive materials are cooled through their Curie temperature T_c , the magnetic moments lose their energetically-favorable random orientation and become clustered into domains, or discrete volumes of atoms with aligned magnetic moments which are separated by domain walls as shown in Fig. 2.9. It is noted that the magnetization M of a material is the net effect of the individual domain magnetic moments m along a given direction. When the magnetostrictive material is subjected to a small magnetic field, the magnetic moments of individual domains rotate. Removal of the low level field allows the domains to return to the original magnetic state, thus being reversible. At high magnetic field levels, both domain rotation and domain wall translation are observed. This movement of domain walls produces irreversible material deformation, since an external magnetic force is required to return the material to its original state [7].

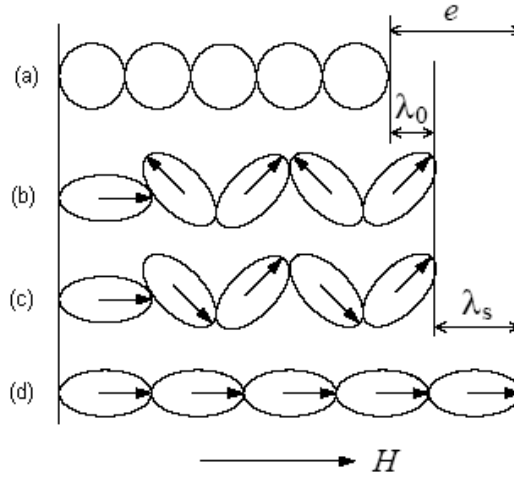


Figure 2.9: Schematic of magnetostriction stages; (a) paramagnetic state above T_c , (b) magnetic state below T_c with no field H , (c) reversible magnetic moment alignment with an applied magnetic field H , and (d) irreversible domain wall rotation from a saturating magnetic field H .

Although magnetostriction is an inherent property of ferromagnetic materials, only a small number of compounds containing rare earth elements can produce “giant” strains in excess of $1,000 \mu\epsilon$. Terfenol-D, developed by the Naval Ordnance Laboratory, is a compound of terbium, iron, and dysprosium ($\text{Te}_{0.3}\text{Dy}_{0.7}\text{Fe}_{1.9-1.95}$). Terfenol-D actuators can produce dynamic deformations up to $3,600 \mu\epsilon$ at room temperature and can have a resonance frequency in the tens of kHz range when laminated, or multiple concentric shells pressed together. Other rare earth-iron alloys do exhibit larger strains than Terfenol-D, however they do so at cryogenic temperatures [8].

For these reasons, Terfenol-D has found uses where small axial deformations are required. Such deformations are known as the Joule magnetostriction effect. The material can also be used for sensing applications through the Villari effect, which manifests itself as a change in magnetization from an imposed stress. Magnetostriction is, in fact, one manifestation of the more general phenomenon of magnetoelastic coupling.

The magnetostriction of Terfenol-D has a highly non-linear and hysteretic behavior as shown by the magnetic induction ($M - H$) and total strain ($\epsilon - H$) curves in Fig. 2.10. It is noted that mechanical pre-loading is necessary with Terfenol-D because it has low strength in tension. A pre-load keeps the material under compression throughout an entire magnetization cycle resulting in a more reliable operating regime. For both positive and negative magnetic fields, Fig. 2.10(b) shows that strain of Terfenol-D is always positive. Therefore, for a sinusoidal input magnetic field, the strain frequency is twice that of the input. For biased, low drive levels, the magnetic behavior can be modeling using the linear constitutive equations

$$\epsilon = s^E \sigma + qH, \quad (2.9)$$

$$B = q^* \sigma + \mu^\sigma H, \quad (2.10)$$

where B is magnetic induction, σ is stress, μ^σ is magnetic permeability at constant stress, s^H is compliance at constant field, and q and q^* are the piezomagnetic (or magnetoelastic) coefficients [28, 9]. Piezomagnetic coefficients are first order coupling coefficients relating the magnetic and mechanical regimes. These equations are linear and do not incorporate hysteresis and nonlinearities found over large drive levels. More advanced models have been developed to capture these magnetostrictive behaviors. The reader is directed to [4, 9, 7, 28] for details.

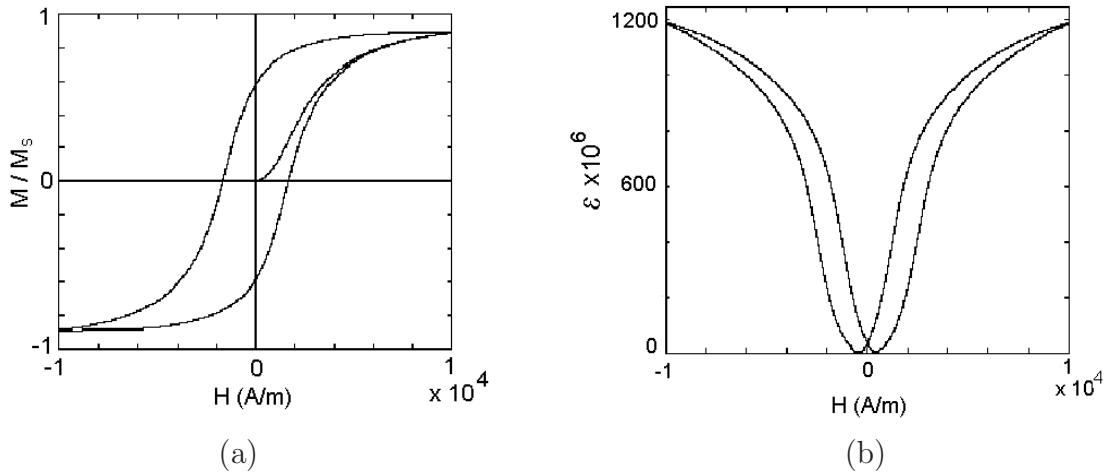


Figure 2.10: Terfenol-D response (a) relative magnetization M/M_s and (b) the magnetostriction strain ε produced by a magnetic field H .

Examples that implement the Joule magnetostriction property of Terfenol-D include sonar transducers, rotary and elliptical motors, and inchworm linear motors. Fig. 2.11 illustrates various sound navigation ranging (sonar) transducer designs which use Terfenol-D as a high power, broadband frequency driving element. One main benefit of Terfenol-D for this application is the improved impedance matching compared to traditional electrodynamic sound transducers (speakers) better suited for use in air [18]. Fig. 2.11(a) is a

flextensional transducer, which is a magnetostrictive rod attached to a flexible shell. Linear vibrations generated by the rod are amplified by the shell, producing sound waves in all directions. Figs. 2.11(d) is a hybrid transducer design of Terfenol-D and PMN-PT (piezoelectric), which can also be used for underwater communications. This design uses two drive elements driven by the same input power. The inherent 90-degree phase shift between the drive elements velocities increase the transducers frequency bandwidth [10].

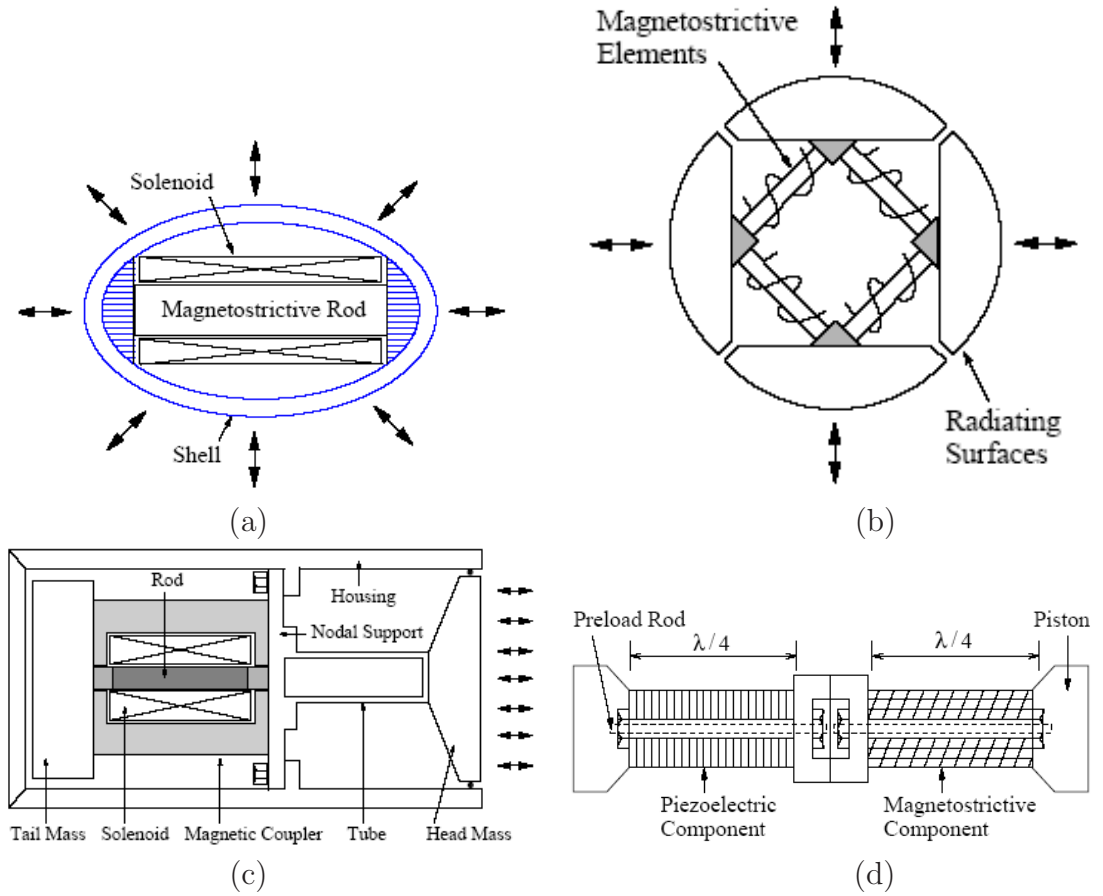


Figure 2.11: Terfenol-D sonar transducers (a) flextensional type, (b) square-ring type, (c) Tonpilz type [8], and (d) hybrid (Terfenol-D and Piezoelectric) type [3].

Another application of Terfenol-D is for rotary motors, as shown in Fig. 2.12. The benefits of using Terfenol-D to produce rotation opposed to conventional hydraulic and

electromechanical devices are higher controllability and the potentially simpler and more reliable design. Fig. 2.12(a) produces an elliptical output from two perpendicular Terfenol-D rods magnetized out of phase. The tip translates through an elliptical motion which rotates a shaft by frictional forces [1]. This has been used for ultrasonic cleaning devices. Fig. 2.12(b) operates by the inchworm concept, which involves clamping and rotation phases. When the clamping force is actuated, the Terfenol-D rods are able to rotate the shaft a discrete step [30]. Upon reaching their displacement limit, the clamp is removed and the Terfenol-D rods are able to retract without reverse rotation of the shaft. This inchworm concept has high torques at low speeds, but tends to lack efficiency. In this paper, Terfenol-D is used to create a high speed fluid pump for the purpose of linear actuation.

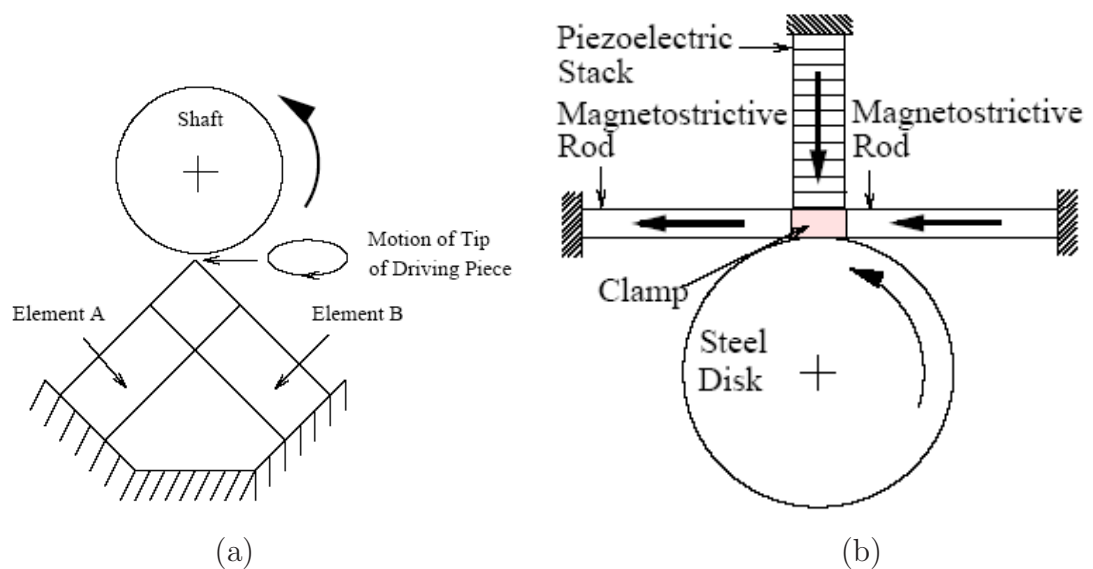


Figure 2.12: Terfenol-D rotary transducers (a) elliptical rotary motor [1] and (b) rotary motor [30].

2.4 Motion Amplification Devices

Smart material transducers are capable of producing large forces over a broad frequency bandwidth, but they do so only at small displacements. Therefore, efficient amplification mechanisms are needed to produce large output displacements concurrently with large forces. Furthermore, to justify the replacement of traditional actuators, smart material actuators must be extremely reliable and have improved bandwidth, power density, and efficiency over traditional actuators. This section presents current smart material amplification techniques being investigated by various researchers for large scale linear actuation.

Originally designed in 1975 by Burleigh Instruments Inc., the inchworm linear motor has been significantly improved with the aid of recent smart material developments. This concept utilizes frequency rectification of piezoelectric or magnetostrictive actuators to increase the displacement while retaining the high force output of the smart material. This is opposed to displacement amplification where additional deflection is at the expense of reduced force [23]. The concept of operation involves sequentially clamping, extending, and un-clamping an output actuator rod by means of piezoelectric or magnetostrictive materials as shown in Fig. 2.13. Each complete cycle extends the output rod a discrete, precise step (the length of the smart material deformation). Operation at high frequencies produces a pseudo-continuous output motion. Miesner and Teter [21] achieved a blocked load of 98 N and an unloaded speed of 2.54 cm/s using piezoelectric stacks for clamping and Terfenol-D for extension. The clamping system determines the force output of the actuator. Park, Carman, and Hahn [23] improved the inchworm clamping mechanism through the addition of micro ridges.

Piezoelectric and magnetostrictive materials have been used to develop a new class of fluid pump for actuation applications [2, 19, 34, 35, 20, 27]. This concept utilizes the active material to pump small volumes of fluid at high speeds, preferably at system resonance,

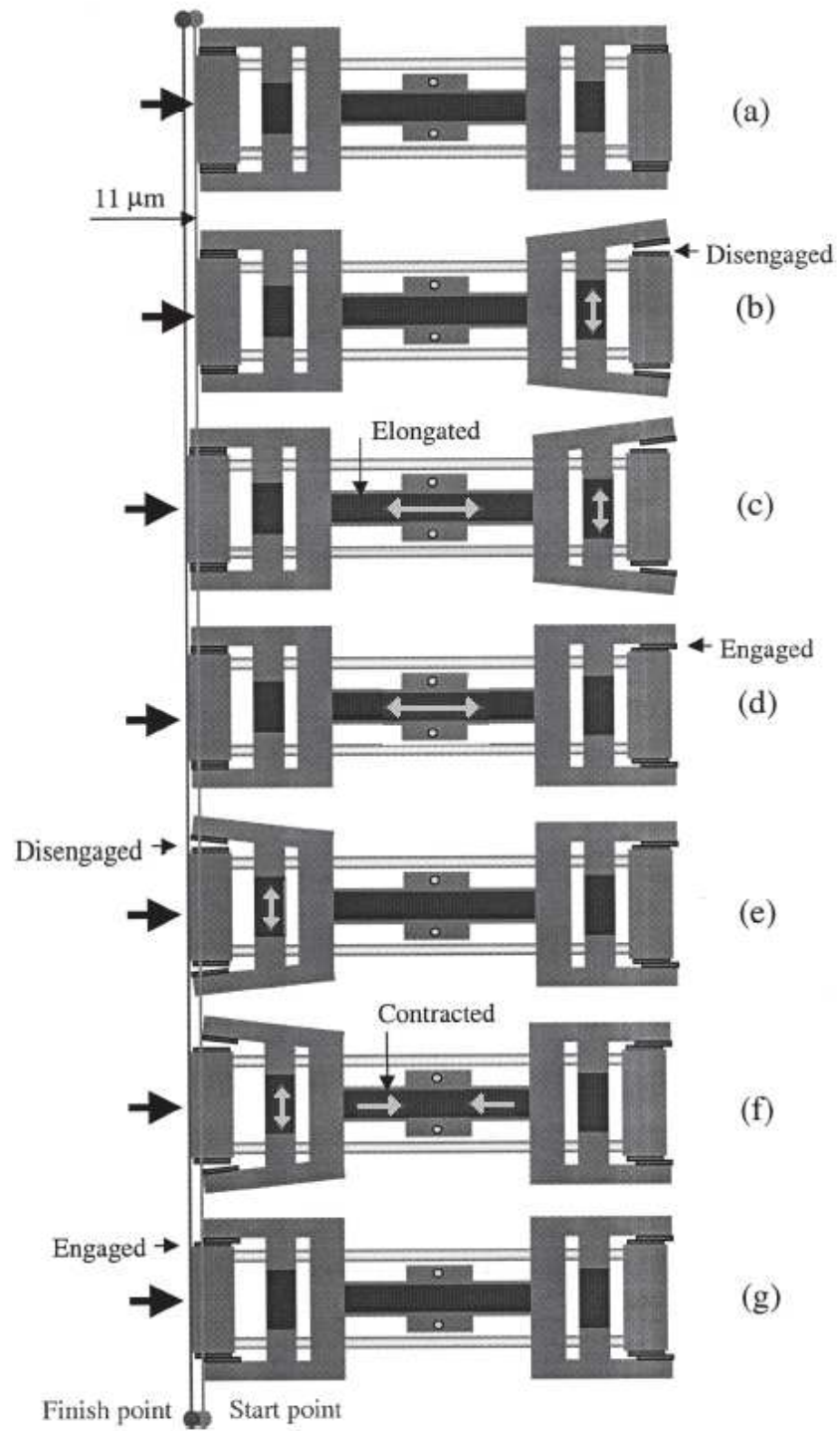


Figure 2.13: Schematic of inchworm operation cycle producing an $11\ \mu\text{m}$ step of actuation [23].

to generate large volume flow rates and pressure. A common design limitation is the bandwidth of directional control valves, both active and passive. A design by Mauck and Lynch [20] employed impedance matching between a piezoelectric stack driver and the fluid load to be displaced to maximize the amount of work produced, while using passive check valves to control flow direction. This design is capable of producing a blocked pressure of 3.5 MPa and an unrestricted flow rate of 2 cc/s. A design by Lee, Or, and Carman [19] uses a piezoelectric stack actuator and steel diaphragm to produce fluid flow and unimorph piezoelectric disk valves for inlet and outlet directional flow control, as shown in Fig. 2.14. The prototype design is capable of producing a flow rate of 3.44 cc/s and a blocked pressure of 8.3 MPa.

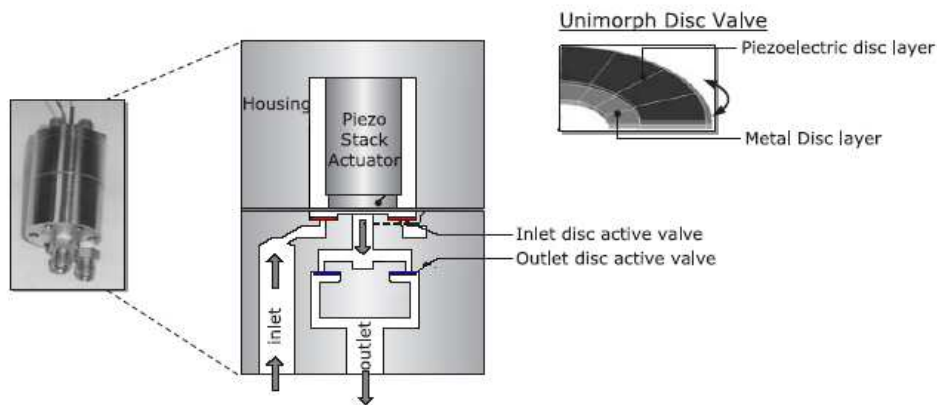


Figure 2.14: Schematic of piezoelectric-hydraulic pump with active unimorph disk valves to control flow at inlet and outlet [19].

The actuator design in Fig. 2.15 by Yoo, Sirohi, Wereley and Chopra [34, 35] is most closely related to the design presented in this study. The actuator employs a piezoelectric pump with passive directional control valves to drive magnetorheological (MR) fluid through a hydraulic network. Four MR fluid valves are located within the network to

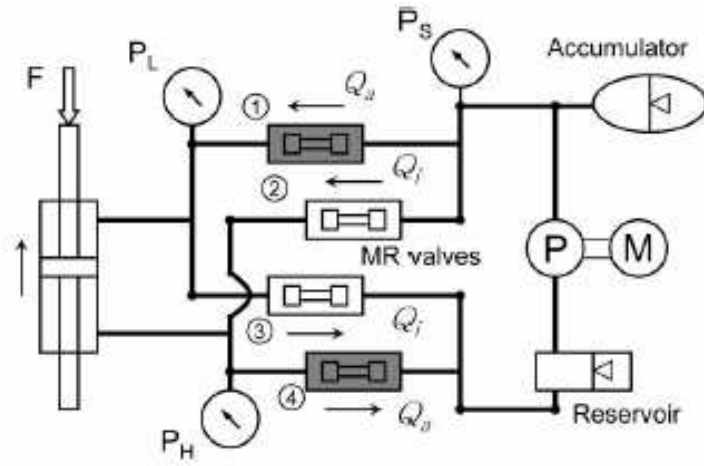


Figure 2.15: Schematic of complete actuator design consisting of a piezoelectric fluid pump and magnetorheological fluid valves [35].

control the unidirectional flow produced by the pump through two paths to provide bi-directional actuation capabilities. The prototype of this design produced an output velocity of 5.34 mm/s against a mass load of 5.15 kg.

CHAPTER 3

HYBRID ACTUATOR: CONCEPT, DESIGN, AND CONSTRUCTION

This chapter is focused on the description of the hybrid actuator concept and how the concept was realized and implemented. This chapter thus comprises three main elements: principle of operation (concept description), actuator design (concept implementation), and actuator construction (concept realization).

3.1 Principle of Operation

The hybrid actuator developed in this study can produce large linear displacements and forces by the integration of Terfenol-D and magnetorheological (MR) fluid. The principle for achieving compact actuation is based on two effects: (i) rectification of resonant vibration produced by a magnetostrictive Terfenol-D pump through MR fluid flow control and (ii) hydraulic advantage for conversion of magnetostrain into large deflection and force. The main components of the hybrid actuator are shown in Fig. 3.1(a)-(c). The system consists of a four-port MR fluid valve, MR fluid, Terfenol-D pump, drive piston, and driven piston. To achieve rectification of the resonant vibrations produced by the Terfenol-D pump, and thus large deflections, the actuator operates through cyclic repetition of two stages, actuator extension and fluid refill. At each stage the MR fluid valve completely closes one half of the fluid circuit and permits free flow through the other half.

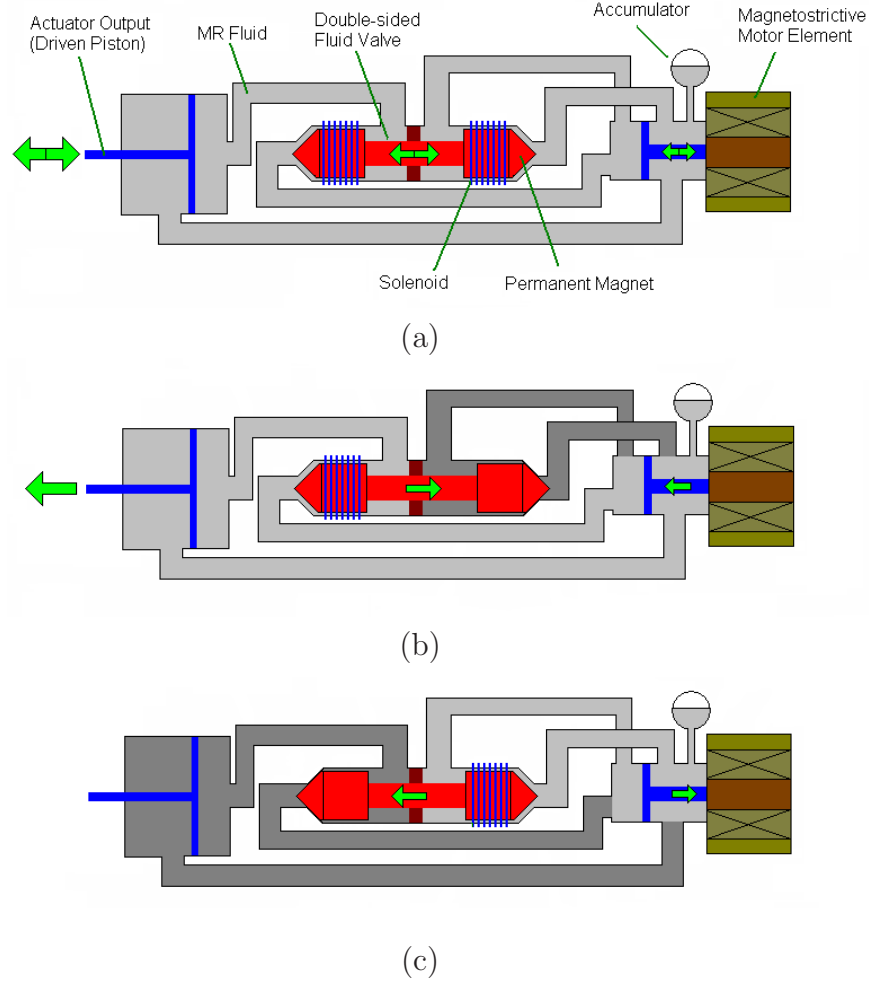


Figure 3.1: (a) Hybrid MR fluid-magnetostrictive actuator. In (b), the drive piston connected to the Terfenol-D pump pushes the fluid through the left valve half and subsequently pushes the driven piston on the load end (left coil active), while the right valve half remains closed. In (c), the drive piston retracts while the MR fluid recirculates through the right half valve (right coil active). The driven piston stays fixed until step (b) starts again and the sequence is repeated. Permanent magnets inside the conical heads provide a bias force on the MR fluid.

Flow generated by the Terfenol-D pump and driving piston is routed through two parallel (with common pressure differential) flow paths. Each fluid route includes one half of the MR fluid valve, and one path includes the driven piston. The MR fluid valve has two conical ends, each fitted with a permanent magnet. Solenoids wrapped around the valve at each end are used to cancel the field produced by the permanent magnets. When the

solenoid around the valve has no applied current, there is no magnetic field cancelation and the MR fluid increases in viscosity. When a suitable current is applied, the coil's magnetic field cancels the permanent magnet's field and the MR fluid decreases in viscosity, thus permitting flow through the valve. This design creates a normally-on mechanism that locks the actuator in place in the event of power failure.

The actuator extension stage commences with the leftmost solenoid turned “on” and the rightmost turned “off,” as shown in Fig. 3.1(b). This effectively thickens the MR fluid in the right path, producing a fluid path of least resistance through the left valve half. The flow produced by the Terfenol-D pump produces a pressure differential that fully closes the right valve half with the assistance of the MR fluid, which when energized by magnetic fields behaves as an O-ring around the conical head. Once the right valve half has closed, the flow extends the driven piston for positive actuation. To increase the output force, a hydraulic advantage is created by implementing a driven piston diameter that is larger than the drive piston.

The fluid refill stage immediately follows as the Terfenol-D element and drive piston begin to retract, as shown in Fig. 3.1(c). To refill the fluid cavity without also retracting the actuator output, the left solenoid is turned “off” and the right turned “on”. This changes the fluid path of least resistance and creates the pressure differential necessary to begin closing of the leftmost valve half. With the left half closed, the actuator output is temporarily locked, and the free flow path through the opened right valve refills the cavity. Steps (b) and (c) are subsequently repeated at high speed to further extend the driven piston and thus achieve quasi-continuous motion of the load attached to the actuator.

3.2 Challenges

The actuator’s principle of operation is relatively simple. However, it is apparent that this concept presents challenges which must be addressed for a successful device. This section outlines problems encountered during the design stages of this research.

The MR fluid valve requires a magnetic input source and a movable valve piece to energize the MR fluid and provide complete valve closure. Complete cancelation of the activating magnetic field is needed to maximize the variable MR fluid viscosity range. The larger the variable viscosity range, the better the valve performance. The movable valve piece feature requires hydraulic seals and bearings to contain fluid within the valve housing and to maintain axial alignment of the valve parts. Minimization of this unwanted sliding friction improves performance and frequency of operation.

The fluid valve and output piston are powered by a magnetostrictive Terfenol-D fluid pump. The Terfenol-D pump requires a fluid piston and fluid directional control valve. The control valve in a reciprocating flow design is the MR fluid valve. The valve must operate near the pump resonance frequency to rectify the flow. The fluid piston requires a seal to prevent fluid leakage. Elastic seals “soften” the fluid pump through additional system capacitance, which absorbs fluid energy intended for fluid valve operation and output actuation. Minimizing the dynamic friction increases output displacement and fluid power.

Capacitance is present in the connecting fluid lines and the fluid itself. Use of rigid lines minimizes added capacitance, however fluid compressibility is a large potential source. The inclusion of trapped air magnifies this compressibility significantly, therefore removal of all possible air pockets is necessary.

Finally, the actuator must be rigidly held to maintain relative component distances. However, increasing rigidity also increases overall actuator size.

3.3 Actuator Design

3.3.1 Magnetorheological Fluid Valve - Design #1

The MR fluid valve must be able to control the flow of MR fluid in an “on”/“off” fashion. The valve consists of two magnetic “conical” heads which sit into respective conical seats when a field is applied to the embedded coils. An alternative design (discussed in Sect. 3.1) employs permanent magnets in the conical heads such that the valve operates in “normally closed” mode. Application of suitable magnetic fields offsets the permanent magnet thus causing the valve to open. The “normally closed” design locks up in the event of power failure. On the other hand, the “normally open” design, shown in Fig. 3.2, is easier to implement and is thus preferable for this first double-sided MR fluid valve generation (design/device #1). This design permits a wide range of magnetic field strengths to be input to the system, while assuring zero field when desired. It is noted that by locating the coils around the conical head piece, the size of the fluid valve increases significantly but reduces fabrication complexity. 300 turns per solenoid (20 rows, 15 turns/layer, 2 solenoids/valve half) was implemented to assure fluid saturation capabilities. The solenoid lead wires were routed out of the housing through the movable rod. Pictures of the device are shown in Fig. 3.3.

The double-sided valve was made by joining two identical halves, coupled by the movable rod piece. This increases the adjustability and observability of the system since the exposed shaft facilitates the recording of the valve location by allowing more conventional sensors. The exposed shaft also permits manual positioning of the valve for consistent initial conditions and allows visual performance evaluation during a test for quality control purposes. The separate valve half housings can be positioned at various distances, which permits adjustment of the length of travel from one closed position to the other. Each valve half has a press-fit oil seal and bronze sleeve bushing to contain MR fluid within the

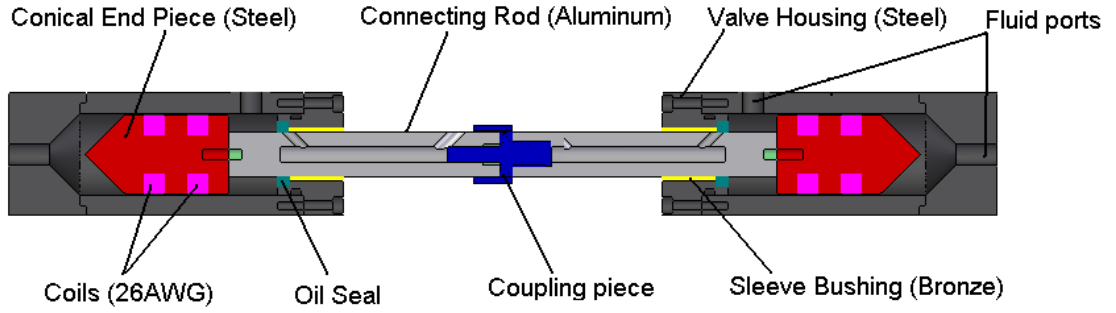


Figure 3.2: Cutaway solid model of the MR fluid valve. The grooves in the conical valve ends are fitted with coils for enhanced flexibility compared with the initial concept, which employs permanent magnets.

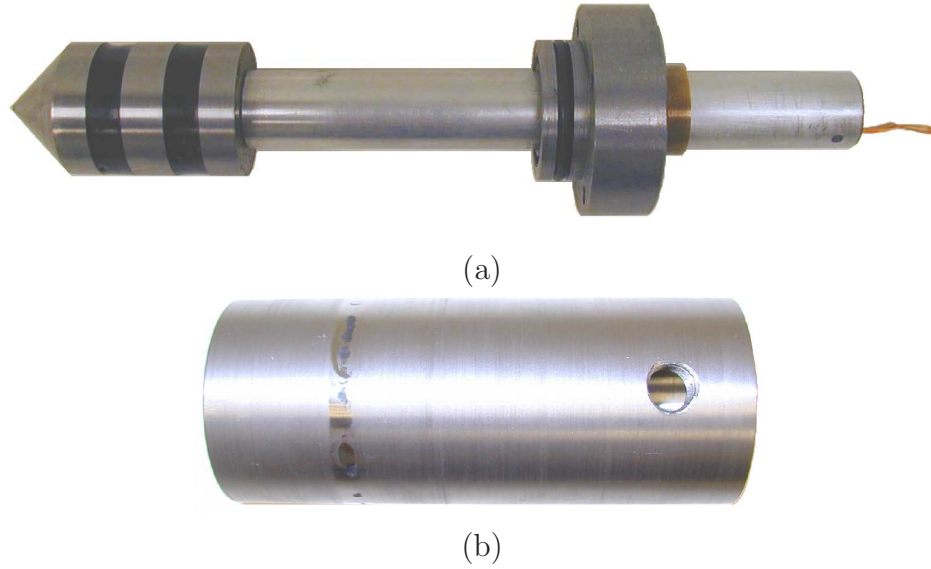


Figure 3.3: Picture of (a) movable valve piece and removable housing piece and (b) the main housing piece of the MR fluid valve device #1.

housing while permitting valve motion. Thus, having two valve halves increases the overall size and doubles the sliding friction forces which significantly reduces the bandwidth of operation. However, for initial testing purposes adjustability is preferred.

The movable head piece, dimensioned in Fig. A.7, is a conical piece bonded to a cylinder. The conical portion is in direct contact with the valve housing during closure. The cone increases the closed-valve contact surface area for a better seal and provides self alignment of the shaft. Both contacting surfaces were honed smooth to assure a tight seal. Two solenoids were wrapped around each cylindrical piece to produce a radial magnetic field for MR fluid activation. The size and location was aided by FEMM V.3.4 ¹, a magnetic finite element analysis program as shown in Fig. 3.4. The head piece and housing are made of steel and the rod, dimensioned in Fig. A.8, is aluminum. This effectively concentrates the flux lines perpendicular to the fluid gap.

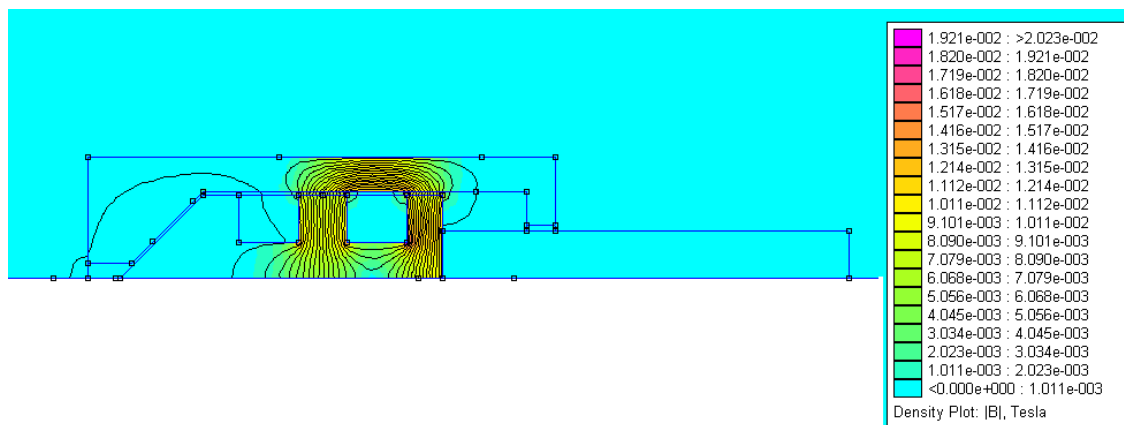


Figure 3.4: Magnetic finite element analysis (FEMM V.3.4) result showing the routing of magnetic flux density lines perpendicular to the flow direction.

As shown in Fig. 3.5, this fluid valve design has two gaps, a fixed annular ring gap and a variable axial gap. The annular ring gap is a critical dimension in the performance of the valve. The smaller the gap, the less power is required to saturate the MR fluid. However, too small of a gap results in large flow resistances in the “off”-state due to excessive fluid

¹<http://femm.berlios.de>

shear stresses. For this fluid valve, an annular ring gap of 0.030 in (or 0.762 mm) was selected. The axial gap varies continuously during operation.

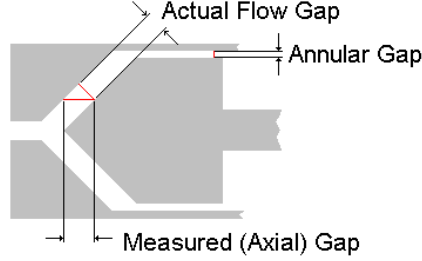


Figure 3.5: Illustration of MR fluid valve gap terminology.

Each valve-half housing consists of three machined pieces. Two of which, dimensioned in Figs. A.3 and A.4, were press-fit and welded together for permanent fastening. Due to machining restrictions, one solid piece was not feasible. The welded pieces allowed for precision machining of the cone seat to assure a good seal with the cone of the movable valve piece. A bolt-on end cap, dimensioned in Fig. A.5, allows assembly and disassembly of the valve. A standard O-ring was inserted between the bolt-on piece and the welded pieces to maintain a tight fluid seal. A spring-loaded oil seal and sleeve bushing were press-fit into the bolt-on housing piece to seal and support the movable shaft.

Each valve half has a housing length of 6.5 in and a diameter of 2.35 in. The overall length of this device with two halves coupled together is approximately 21 in. Additional details of MR fluid valve design #1 are included in Appendix A.1.

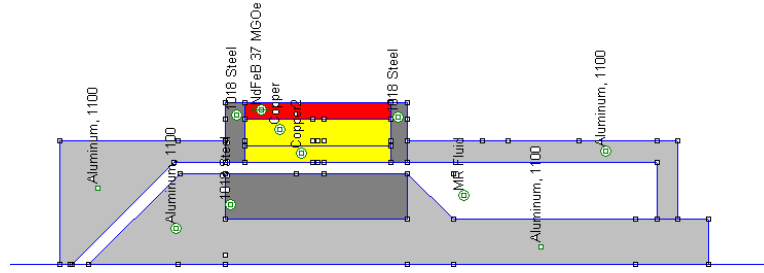
3.3.2 Magnetorheological Fluid Valve - Design #2

A second magnetorheological (MR) fluid valve (design/device #2) was developed following evaluation of the experimental data collected from design #1. The main redesign goal was to significantly reduce the overall size of the fluid valve while increasing the “on”

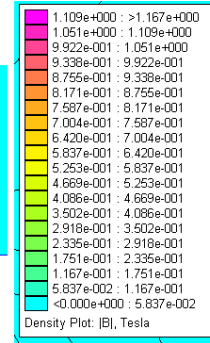
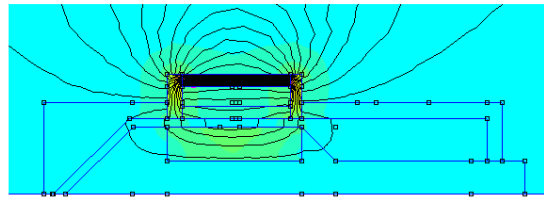
state fluid resistance of the valve. A size reduction lowers the amount of fluid stored within the system, thus lowering unwanted fluid inertia and capacitance effects. More importantly, the volume of MR fluid necessary to operate the valve is reduced and capable of operation with inputs generated by the unidirectional Terfenol-D pump presented in Sect. 3.3.3.

To reduce the overall size, the coils were removed from the movable valve piece. Several design considerations implementing a permanent magnet as discussed in the actuator principle of operation were analyzed through magnetic finite element analysis (FEMM V.3.4). A representative case is shown in Fig. 3.6. The difficulty of this design is the ability of an external solenoid to effectively cancel the permanent magnetic field to allow Newtonian flow of the MR fluid. Fig. 3.6(b) shows the magnetic flux created with the external solenoid turned “off.” As shown in Fig. 3.6(c), the magnetic flux is redirected to various locations with the solenoid “on”. This effectively reduces the critical magnetic field perpendicular to the flow gap. However, undesired magnetic field is still present.

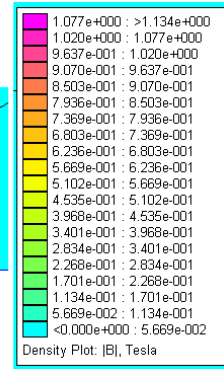
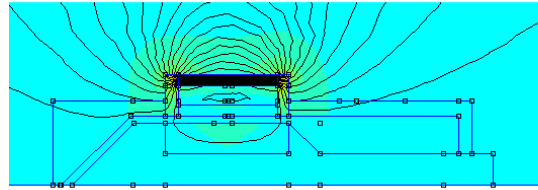
In the interest of adjustability and the desire for a zero magnetic field state, designs using only an external solenoid were considered with variations of solenoid size, number, and location. The size increases the magnetic field strength, but reduces the activated fluid area. The finalized design is shown in Fig. 3.7. This design doubles the number of activated fluid areas over that of the previous design. A solenoid stack of 4 coils are powered with alternating current directions. In other words, the first and third coils are powered with a positive current direction when two and four are powered with a negative current. This provides addition of the magnetic field between adjacent coils. The magnetic flux is routed radially through steel disks separating the coils. The benefit of multiple coils is the concentration of flux perpendicular to the flow gap at more locations. This significantly increases the volume of fluid energized by the magnetic field, which directly improves the performance of the MR fluid valve.



(a)



(b)



(c)

Figure 3.6: Magnetic finite element analysis of non-implemented valve design (a) axis-symmetric model with external solenoid and permanent magnet for (b) the solenoid “off” case and (c) solenoid “on” case. Magnetic field is always present across gap.

A solid model showing additional design details is shown in Fig. 3.8(a). The housing in this design is made of steel, composed of two pieces which assemble together with radially oriented bolts. Radial bolts produce a compact design, although this configuration places each bolt in shear (as opposed to tension). The housing was reduced to two components, dimensioned in Figs. A.11 and A.12, by switching the removable end-cap to the side with

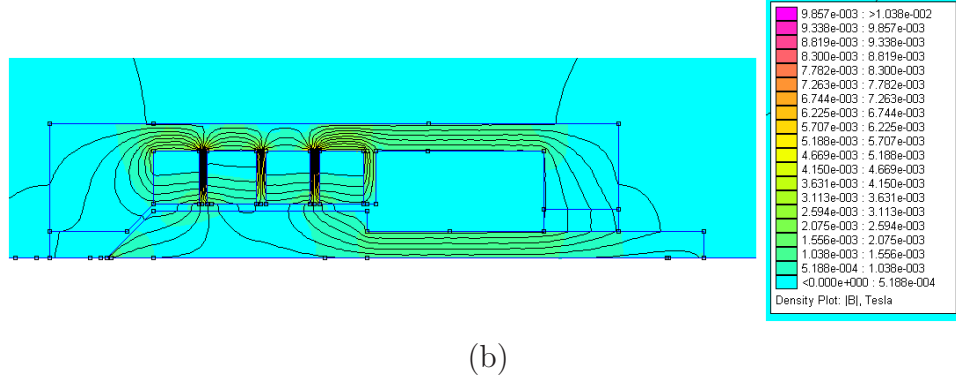
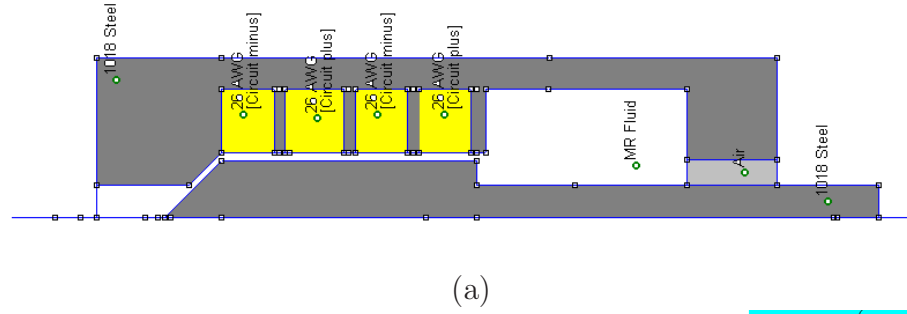
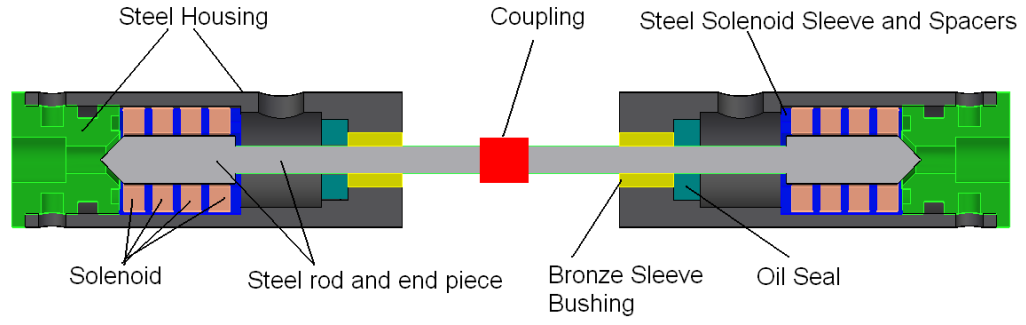


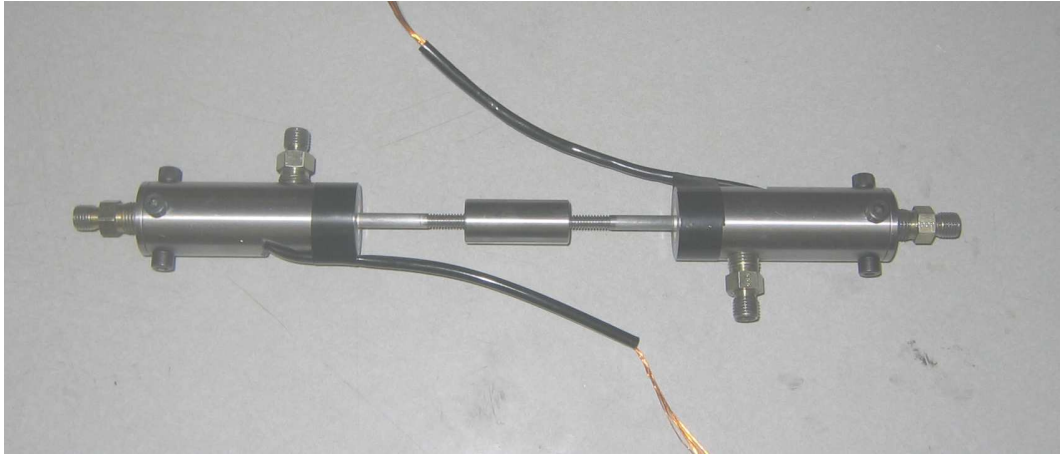
Figure 3.7: Magnetic finite element analysis of MR fluid valve design #2 (a) axis-symmetric model with external solenoid for (b) the solenoid “on” case. The solenoid “off” case is exactly zero at all locations.

the conical cutout. This permits precision machining of the conical seat, while maintaining the ability to press-fit a spring-loaded oil seal and bronze bushing for sealing and support of the movable shaft. An O-ring was inserted between the housing components for a proper fluid seal. Also, a face mounted O-ring was placed between the end cap and solenoid stack to avoid leakage from the outer perimeter of the coil stack to the conical fluid chamber.

Each solenoid within the stack was wound around an aluminum sleeve with 0.020 in thickness and separated by steel disks spaced 0.20 in apart. Winding epoxy was used between solenoid layers to add structural integrity, while providing electric insulation and heat dissipation. To aid in alignment and ease of assembly, the coil stack was inserted into a steel sleeve as shown in Fig. 3.9, which could easily be slid into the housing. The removable end cap and a notch in the cylindrical housing clamp the coils in place. The



(a)



(b)

Figure 3.8: MR fluid valve design #2 (a) cutaway view of a solid model and (b) the actual fluid valve. Coil stacks were relocated to the inner housing surface to allow significant size reduction of the movable valve piece.

lead wires for each solenoid were routed through the slot in chamber wall and sealed with epoxy.

The movable valve component, dimensioned in Fig. A.13 is a single steel piece which translates linearly between the coil stack. Similar to design #1, it implements a cone bonded to a cylinder. The cone increases sealing surface area and provides self alignment. The cylinder provides a constant annular gap for MR fluid activation. Another benefit of moving the solenoids outside of the MR flow gap is that a steel connecting rod was found

to produce minimal magnetic leakage. Similar to design #1, the fixed annular gap was kept as 0.030 in.

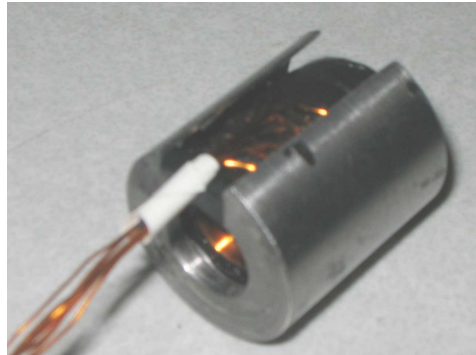


Figure 3.9: Picture of coil stack within a steel sleeve.



Figure 3.10: Picture comparing the size of valve design #1 and design #2. Design #2 has a 570 percent smaller volume.

Each valve half has a housing length of 3.625 in and a diameter of 1.25 in. The overall size of this device with two halves coupled together is approximately 12 in in length. The size reduction from design #1 to design #2 is shown in Fig. 3.10. This amounts to a 570 percent decrease in volume. Additional details of MR fluid valve design #2 are included in Appendix A.2.

3.3.3 Unidirectional Terfenol-D Fluid Pump

The actuator concept includes a high speed, reciprocating MR fluid flow produced by a Terfenol-D pump. An integrated MR fluid valve capable of operating at such low volume flow rates is needed before this type of pump becomes practical. As a starting point, a Terfenol-D pump which creates flow in a single direction was designed and constructed for coupling with MR fluid valve design #2. An oscillatory flow can be created from a traditional solenoid controlled fluid valve. It is noted that the benefits of the reciprocating flow pump is the minimal amount of moving parts, which leads to better reliability and broader bandwidth.

The unidirectional design is shown in Fig. 3.11, which consists of a Terfenol-D transducer, alignment block, piston, and chamber. There are two fluid ports, each fitted with a ball-and-cone type directional control valve. The directional control valves allow flow in one direction while impeding all flow in the opposite. Using this passive control device, a unidirectional flow is created from an oscillating piston as shown in Fig. 3.12. It is noted that passive valves have a bandwidth much lower than the resonance frequency of the Terfenol-D transducer. The optimal pump design would permit an input frequency near resonance of the Terfenol-D transducer (low kHz range), however this is well outside the usable range of the directional check valves. Specific operating limits are discussed in Sect. 4.4.

A typical Terfenol-D transducer design is shown in Fig. 3.13. The actual transducer used was supplied by Etrema Products, Inc. (Ames, Iowa) as in-kind contribution, which has a slightly different design. The transducer consists of a solenoid and Terfenol-D rod encased within a rigid steel housing. One end consists of a pre-load mechanism to assure the material always operates under compression. It is noted that the compression strength of Terfenol-D is one order of magnitude greater than that in tension. The other end includes

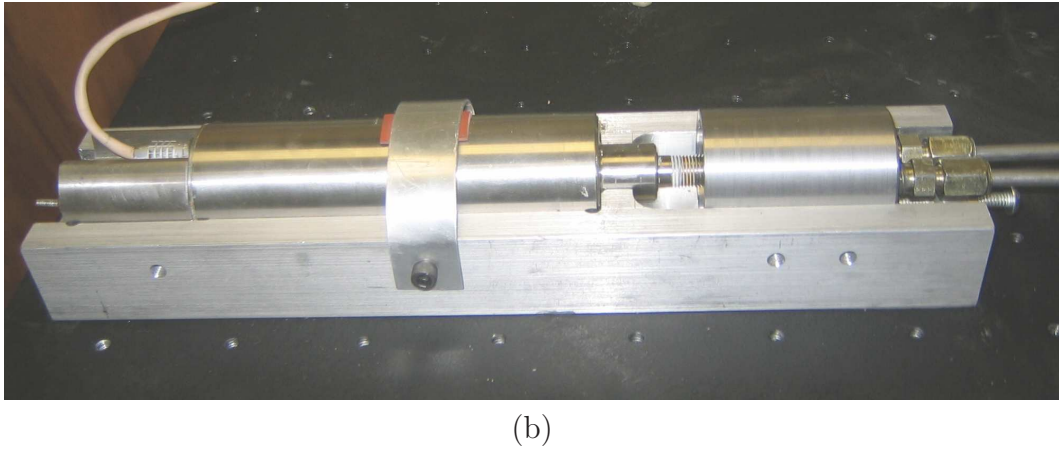
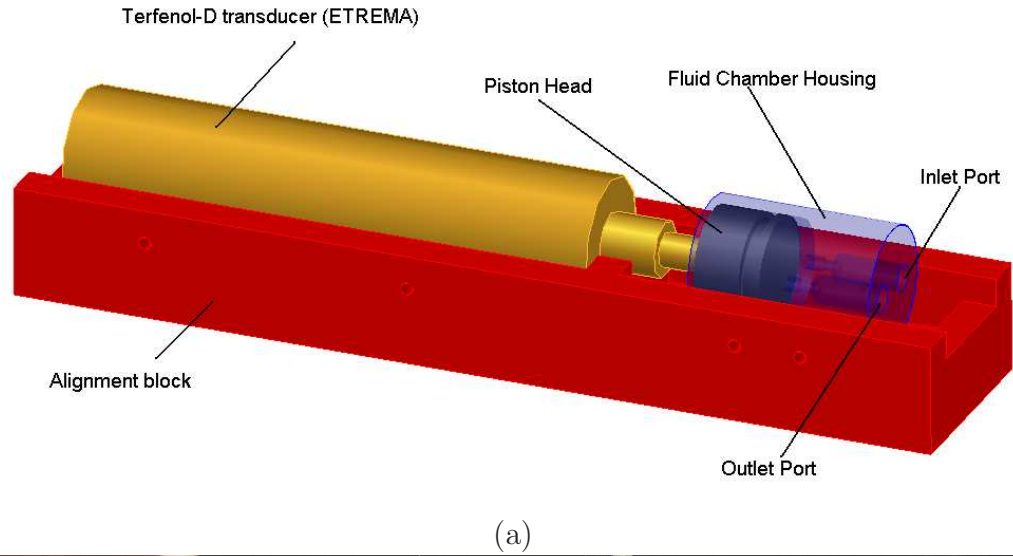


Figure 3.11: Unidirectional Terfenol-D fluid pump design (a) solid model and (b) the actual Terfenol-D fluid pump. The Terfenol-D transducer was supplied by Etrema Products, Inc. (Ames, Iowa) as in-kind contribution.

a push rod to transmit the vibrations produced by the transducer. The components are arranged such that there is a closed magnetic loop throughout the transducer and a strong magnetic flux along the axial direction of the Terfenol-D rod.

Additional components which improve the performance of the Etrema transducer include permanent magnets and an inertial tail mass. The tail mass (530 grams) is used to direct most of the deflection towards the push rod, instead of the housing. This effectively allows for a less massive clamping system to produce work at the push rod. The permanent

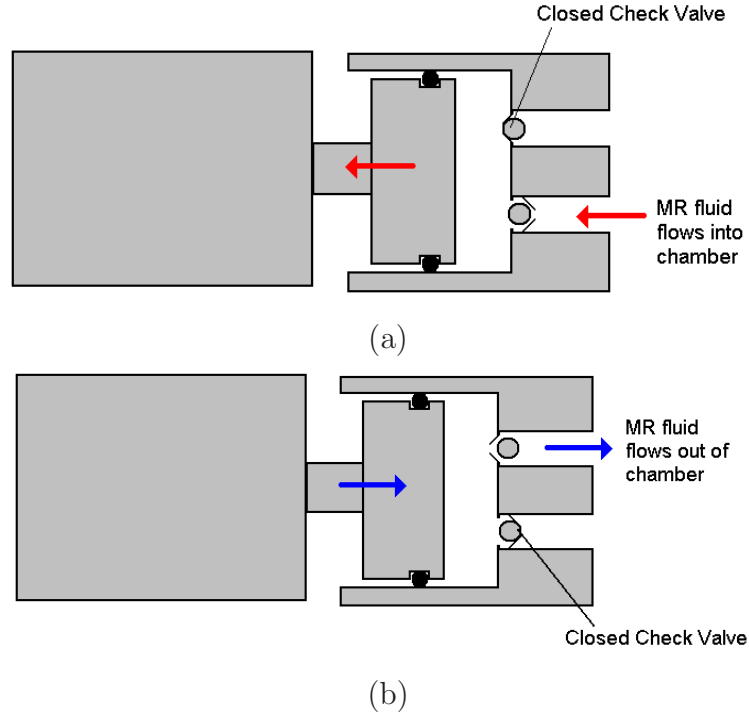


Figure 3.12: Illustration showing the two stages of operation for the unidirectional Terfenol-D fluid pump design using directional check valves; (a) pump refill and (b) output flow stage.

magnets create a magnetic bias which shifts the transducer operating range to the steepest portion of the $\varepsilon - H$ curve (shown in Fig. 2.10) for more efficient operation.

An aluminum piston head is mounted directly to the transducer push rod and seated within a steel chamber. A dynamic fit O-ring was placed between the reciprocating piston and the stationary housing for an elastic fluid seal. Directional control valves purchased from Lee Corp. were press-fit into the housing. The open ended chamber allows for an adjustable fluid chamber and permits the attachment of an accelerometer which can be used to obtain performance details. Additional dimension details are included in Appendix A.3.

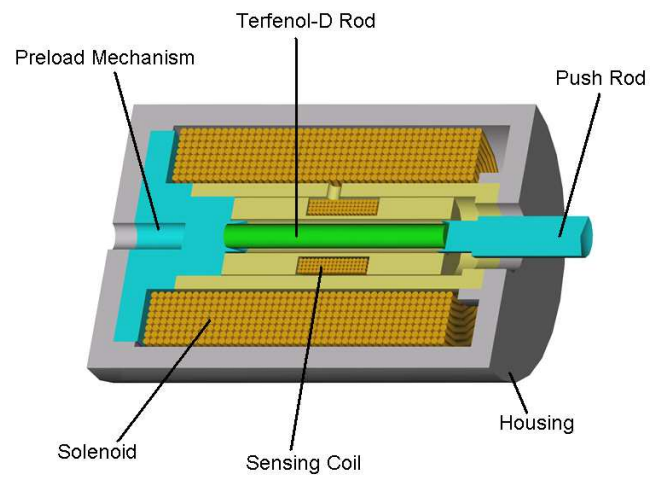


Figure 3.13: Solid model of a typical Terfenol-D transducer design.

CHAPTER 4

EXPERIMENTS

Experiments were performed on individual actuator components and the actuator system. The initial experiments were conducted to verify the fluid valve's ability to self control flow using magnetorheological (MR) fluid. Successful self control of the fluid valve led to the incorporation of an output piston to determine that linear actuation could indeed be generated. Inputs to the experimental setup proceeded from manual to automatically controlled for a more accurate assessment of performance. For modeling and analysis purposes, the variable fluid resistances of the MR fluid valve were quantified. It is noted that system-level modeling was performed concurrently with experimental testing and will be discussed in Chapter 5. Experiments concluded with the performance testing of the Terfenol-D fluid pump.

4.1 Fluid Valve Testing Using Manual Pump

4.1.1 Objective and Construction Details

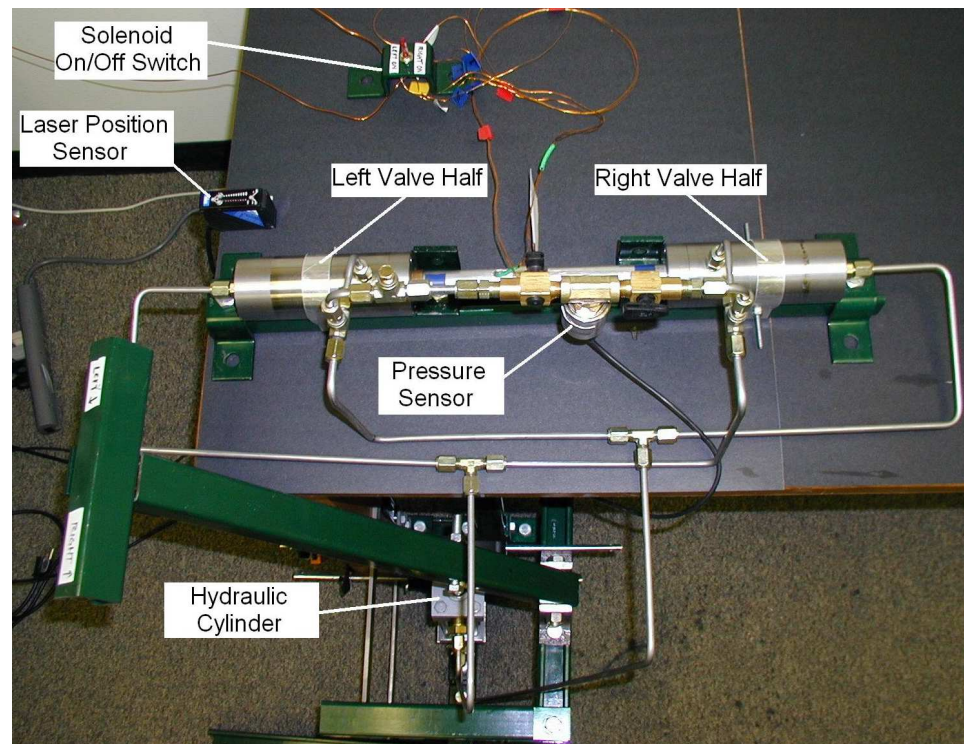
The first experimental objective was to demonstrate the feasibility of the MR fluid valve, especially concerning its ability to regulate oscillatory flow through both sides. For valve operation, both a pressure differential across the valve and a change in the viscosity of MR fluid are required.

Experiments in this stage focused on the ability of a “double-sided” MR fluid valve to cycle between high and low fluid restriction (or fully closed and fully open). A double-sided valve refers to a single valve controlling flow for two fluid paths simultaneously. In our design, the two paths are on opposite sides of the valve. For proof of concept purposes, design #1 was developed and fabricated as shown in Fig 3.2.

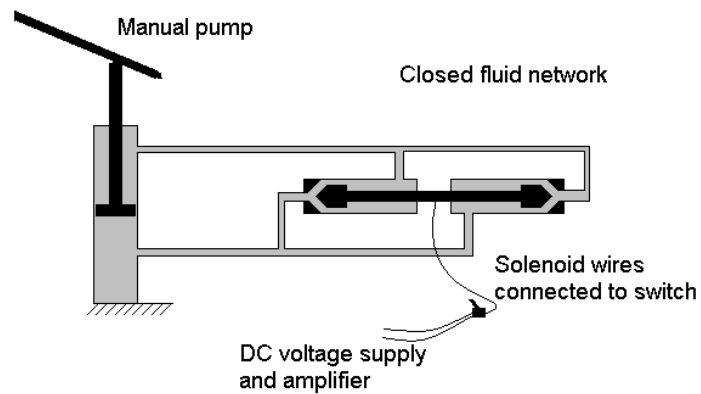
The closed-loop experimental setup is shown in Fig. 4.1. Input MR fluid flow rate and pressure was applied to the fluid system through a manually operated, single-sided hydraulic cylinder (Miller HV Series 150) with 1.5 in bore, 0.625 in rod, and 6 in stroke. It is noted that no Terfenol-D fluid pump had been created at that point in the research time-line. The pressurized MR fluid is divided into two flow paths, one through each valve half, with the volume flow fraction depending on valve location and fluid viscosity. A single pressure sensor (Sensotec GM-A 992453) was used to record the pressure during the experiment for one MR fluid valve half, depending on the positions of the “on”/“off” valves on either side of the sensor. Voltage to the coils was supplied by a dc power source (Tektronix CPS250) and linear amplifier (MB Dynamics SL500VCF), routed through a DPDT switch (Radio Shack 275-653A) to limit one coil to be “on” at any given time. Motion of the valve was measured with a non-contact laser displacement sensor (SA1d-LK4), aimed at a target attached to the midpoint of the valve’s shaft. Measured signals include fluid pressure, shaft displacement, and input voltage magnitude. Data acquisition (DAQ) was conducted using DataPhysics hardware (SignalStar Vector) and software (SignalCalc Mobilizer).

4.1.2 Non-activated Fluid Valve Results

The ability of the MR fluid valve to operate with only a pressure differential and no changing fluid viscosity (zero solenoid voltage) was tested. The manual hydraulic cylinder was pumped hard enough to create over 100 psi of line pressure. The MR fluid valve was biased to both closed positions in subsequent tests (two tests per starting position) as shown



(a)



(b)

Figure 4.1: (a) Actual and (b) schematic of the experimental setup used for testing of an early double-sided MR fluid valve.

in Fig 4.2. The pressure differential alone is not sufficient to operate the double-ended fluid valve, and the change in apparent viscosity due to applied magnetic fields is required to increase the pressure differential. It is noted that in all valve location data presented for manual pump operation, the data was translated and scaled by the (min/max) ratio. Noise peaks in the data cause the nominal 0.0 (left closed) and 1.0 (right closed) to be shifted slightly.

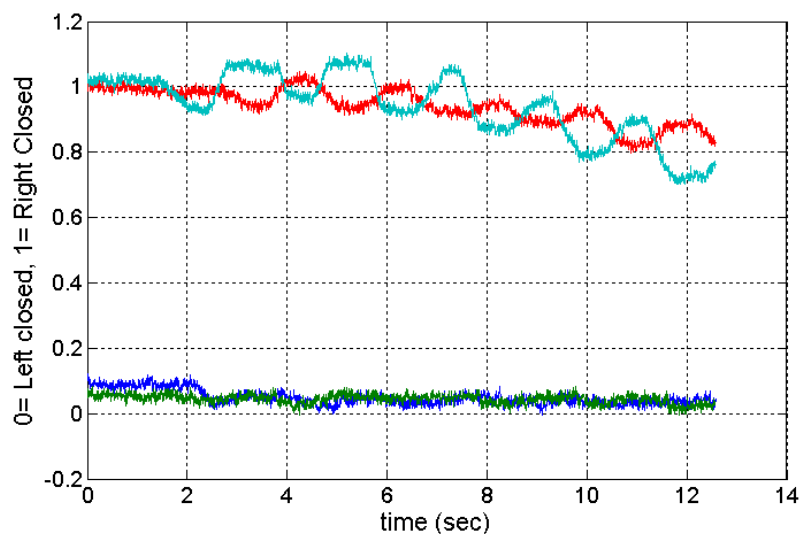


Figure 4.2: MR fluid valve motion from an oscillatory pressure and flow, but with no solenoid input voltage. Both initial valve positions, left closed ($=0$) and right closed ($=1$), were tested twice for repeatability.

4.1.3 Activated Fluid Valve Results

The ability of the MR fluid valve to operate under both pressure differentials and fluid viscosity change was tested through manual cycling of the input hydraulic cylinder and a dc voltage applied to the solenoids. In Figs. 4.3(a),(b) a dc voltage of 20 V was applied to the right solenoid while the manual hydraulic cylinder was extended up. Immediately after closure of the right valve half, an identical voltage was applied to the left solenoid,

followed by a manual retraction of the hydraulic cylinder. This cycle was repeated at approximately 0.8 Hz, for a run duration of over 12 seconds. Fig. 4.3(c) shows the pressure recordings from the left valve half from a similar run. The fluid valve cycles between fully closed left to fully closed right with the appropriate combination of pressure differential and viscosity change. The difference in pressure between the left and right sides is attributed to the volume change caused by the hydraulic cylinder's connecting rod. As the piston is extended, the volume of the rod is removed from the upper piston half, but not the lower piston half. Depending on the direction of pumping, dissimilar pressure differentials across the system are produced.

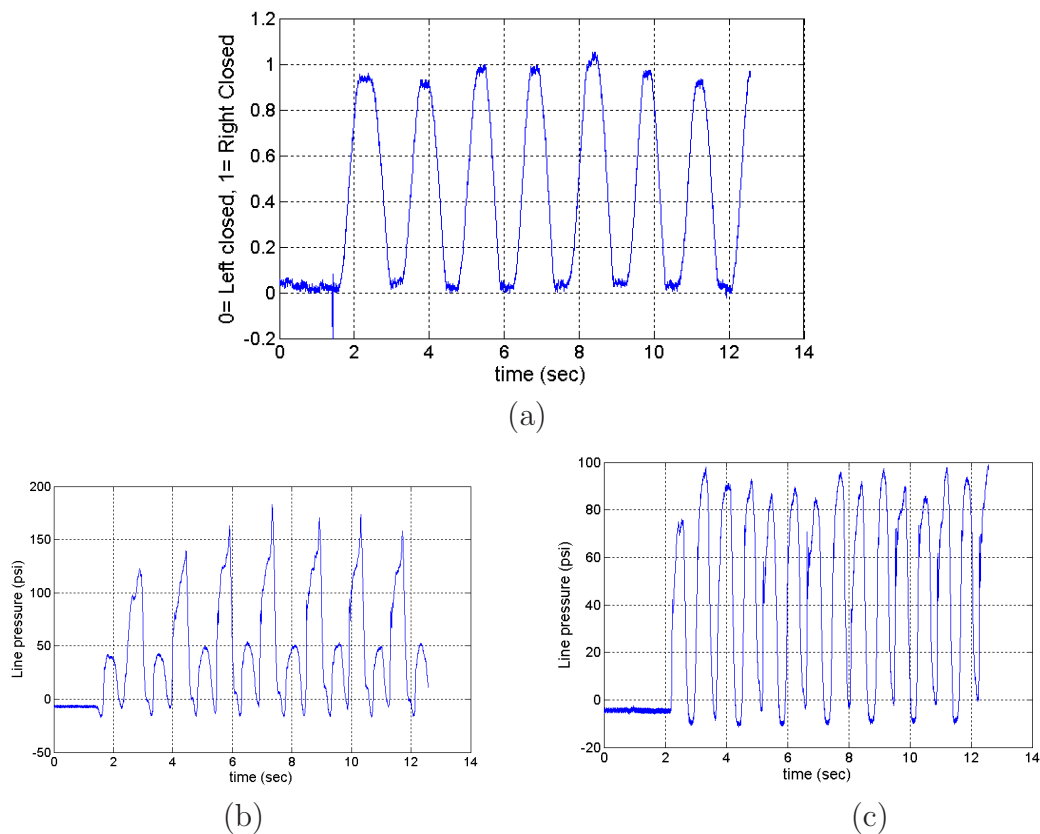


Figure 4.3: (a) MR fluid valve motion under an oscillatory hydraulic input and a 20 V solenoid input voltage. (b) Recorded pressure from the right valve inlet and (c) recorded pressure from the left valve side from a similar run.

Fig. 4.4 presents records from the procedure discussed immediately above, but with an input of 5 V opposed to 20 V. The MR fluid valve is able to cycle between fully closed and fully open with the lower input voltage. Furthermore, it is qualitatively observed that less force on the hydraulic cylinder is required to produce valve motion. This implies that maximum efficiency for this configuration is obtained by a solenoid voltage close to 5 V rather than 20 V.

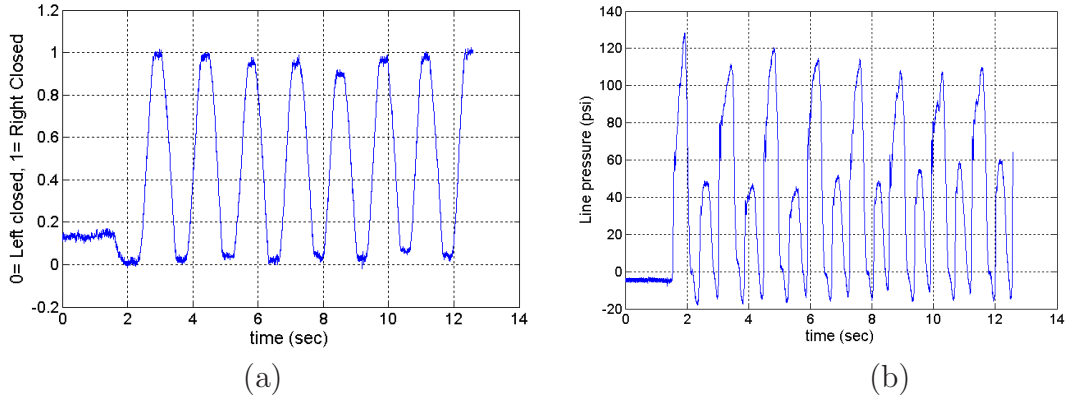


Figure 4.4: MR fluid valve (a) motion under an oscillatory hydraulic input and a 5 V solenoid input voltage and (b) recorded pressure from the right valve inlet.

4.2 Fluid Valve Testing with Output Piston and Automated Pump

4.2.1 Objective and Construction Details

The previous experimental setup included a hydraulic cylinder attached to a manual pump as the input and had no output piston to perform usable actuation. The main objective of the measurements described in this section was to add an output piston to verify the MR fluid valve's ability to rectify an oscillatory input flow and create positive linear actuation. A second objective was to replace the manual input pump in favor of an automated input. This change produced more controllable and repeatable inputs which were desired for analysis and development purposes.

This experimental setup included an automated fluid input from a controllable universal compression-tension machine (i.e. MTS), rather than a manual pump as in the previous experiments. To maintain a constant volume within the closed MR fluid network, a double-sided hydraulic piston (Allenair ED; 1.5 in bore, 0.5 in rod, 6 in stroke) replaced the single-sided piston from previous testing. A double-sided hydraulic piston has a push rod extending through both ends of the housing cylinder to maintain a constant internal fluid volume. Fig. 4.5 illustrates the system while Fig. 4.6(a) shows the main components and connections of said experimental setup. A second double-sided hydraulic piston was added to the closed MR fluid network to obtain work output from the system. A diameter smaller than the input piston is desired for hydraulic (dis-)advantage; the smaller diameter produces larger displacements. The selected output piston (Clippard 7DD-9) has a 0.875 in bore and a 0.25 in rod, with a maximum travel of 9 in. To prevent bottoming out of the piston, the safe operation range was 8 in. This physical constraint limited the total amount of actuation possible before the system had to be stopped and reset.

The two steps that make up one full cycle are shown in Figs. 4.6(b),(c). First, the input cylinder is pulled down for positive input displacement (piston rigidly held), which creates flow of MR fluid, denoted $F1$. By closing the left valve half with the assistance of the solenoid in the left valve half, all flow is directed through the output cylinder and the right valve half. The flow effectively extends the output piston a discrete step. Next, the input displacement direction is reversed, directing flow in direction $F2$. To prevent the flow from returning the output piston, which would negate all actuation motion, the right valve half is closed by applying voltage to the right solenoid. Therefore all flow is routed through the left valve half, keeping the output piston locked in place. The cycle is repeated to further extend the output piston.

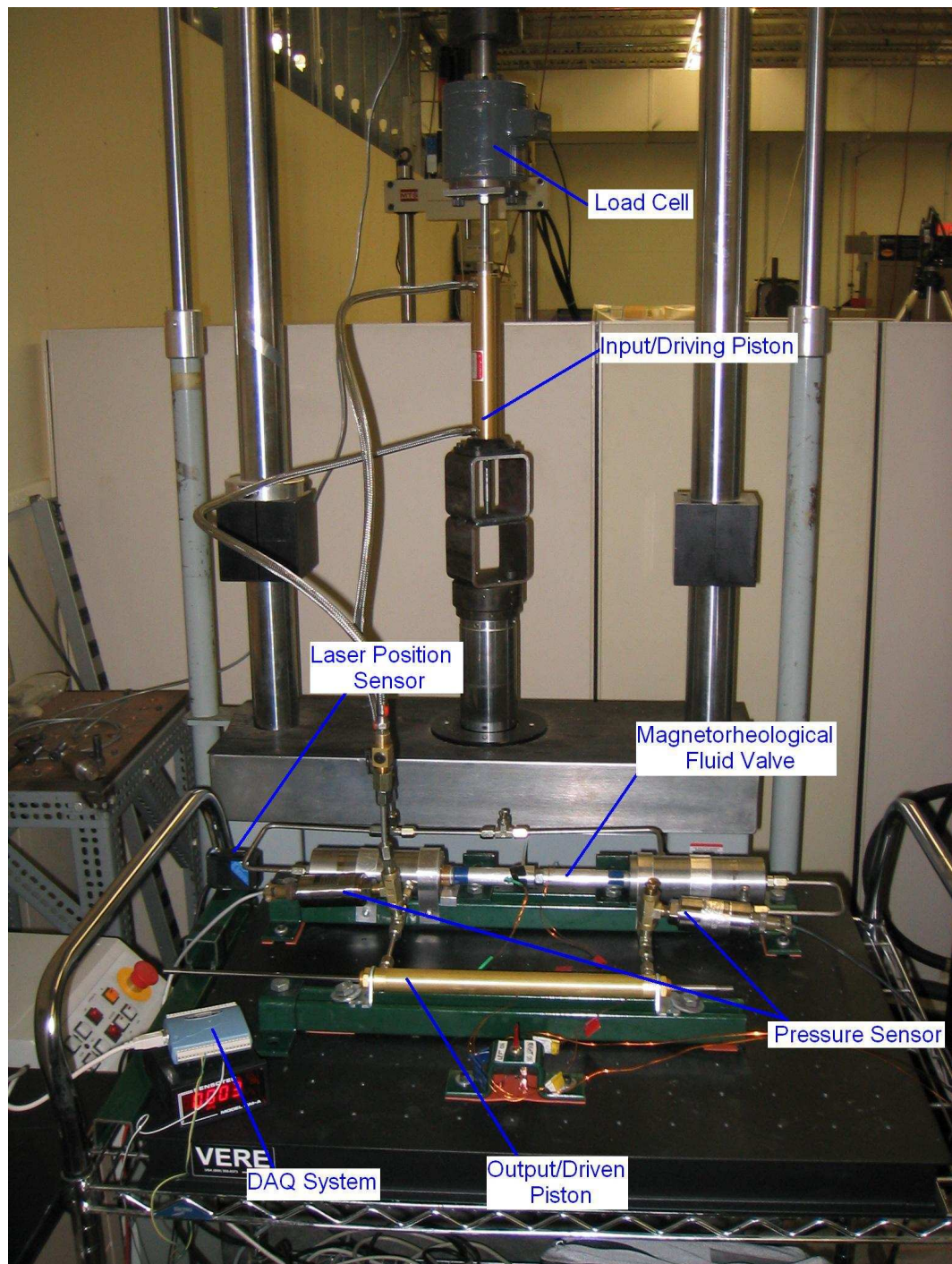


Figure 4.5: Experimental setup with automated inputs used for controlled actuation.

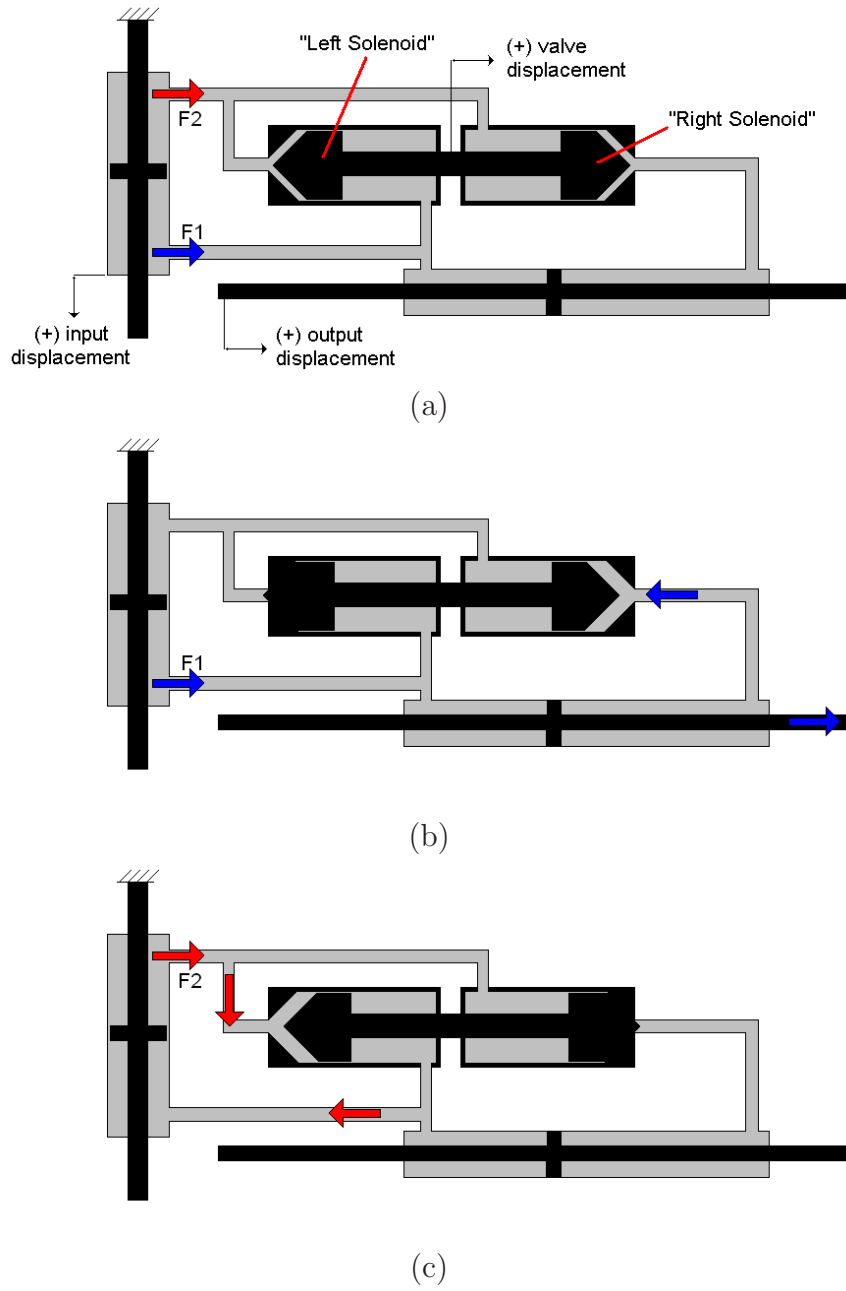


Figure 4.6: Illustrations of (a) automated input piston experimental setup with double-sided valve and output piston, (b) actuation step of operation, and (c) the refill step needed to complete one actuation cycle. A positive input displacement produces flow $F2$ and negative input displacement produces flow $F1$.

4.2.2 Solenoid Timing

To determine when each solenoid should be energized during a run, initial tests were performed using a single ramp input piston displacement and comparing the effects of different voltage applications, input stroke length, direction and rate, and initial valve position on the output piston displacement. More specifically, after setting the initial fluid valve and output piston locations and magnetizing a valve half with a constant dc voltage, the MTS machine input a single ramp displacement to the system. After all motion seized, the final position of the output piston was recorded. It is noted that motion often continued a few seconds after the input piston motion ended. This is likely due to system capacitance and inertial effects.

The data collected is shown in Tables 4.1 and 4.2. It is apparent that the left valve (fluid route not through output piston) has the most control over the system. With the left valve's solenoid turned "on" and a negative ramp input, the output displacement is approximately +5 in regardless of the initial valve position (left closed, middle, right closed). On the other hand, the right valve is extremely dependent on initial valve location, having output displacements ranging from +5 7/8 in to +1/8 in. Leaving both solenoids "off" had a similar large range. Positive and negative are as defined in Fig. 4.6(a).

Switching the direction of input stroke from negative to positive and leaving only the left solenoid "on" produced output displacements in the range of 0 to -1 1/4 in. It is noted that small negative displacements are preferred to minimize unwanted recoil of the output piston. Energizing the left or right solenoid produced similar output ranges. However, not energizing either coil pushed the output piston an undesirable -2 in.

From these preliminary ramp tests, it is concluded that for fastest output actuation, one of two control strategies should be implemented. First, the left solenoid should be "on" for both positive and negative MTS direction inputs. Second, the left solenoid should be

Voltage Application	Initial Valve Position		
	Left Closed	Middle	Right Closed
Left Valve Half “On”	+ 5 3/8	+ 4 7/8	+ 4 1/2
Both “Off”	+ 4 3/4	+ 3 3/8	+ 1
Right Valve Half “On”	+ 5 7/8	+ 3 7/8	+ 1/8

Table 4.1: Output piston displacement (in) from a ramp input of 2 in magnitude in the negative direction at a rate of 3.0 in/s.

Voltage Application	Initial Valve Position		
	Left Closed	Middle	Right Closed
Left Valve Half “On”	- 1 1/4	- 3/8	0
Both “Off”	- 1 3/4	- 2	0
Right Valve Half “On”	- 1 1/8	- 5/8	0

Table 4.2: Output piston displacement (in) from a ramp input of 2 in magnitude in positive direction at a rate of 3.0 in/s.

“on” for negative MTS direction inputs and both solenoids “off” for positive MTS direction inputs.

4.2.3 Input Waveform

In this experimental stage, various sinusoidal waveforms were generated by the MTS machine and applied to the input hydraulic cylinder while manually controlling the voltage applied to the solenoid in each valve half. The objective was to produce positive actuation through manual control of the solenoids. A secondary objective was to determine the bandwidth of the system.

The voltage applied to each solenoid was manually controlled by means of a DPDT switch. It was observed that frequencies near 2 Hz pushed the limits of controllability without major timing inaccuracies. Various control strategies were tested for two input

waveform frequencies, 0.5 Hz and 1.0 Hz. The net output displacements for each run are shown in Table 4.3.

The control strategy of left solenoid “on” for both positive and negative MTS direction inputs was determined in Sect. 4.2.2 to be one of two preferred control strategies. However, this control strategy produces relatively small actuation values when employing sinusoidal inputs. This is attributed to there being no “low” resistance fluid path through the left valve half during the “refill” stage, illustrated previously in Fig. 4.6(c).

The control strategy that yields the highest performance is left solenoid “on” for negative input directions ($F1$) and both solenoids “off” for positive input directions ($F2$). This control strategy varies from that of the actuator concept, which uses the strategy of left solenoid “on” for a negative MTS direction input and right solenoid “on” for a positive MTS direction input. This discrepancy in the results is attributed to the asymmetric flow path resistances generated by the output piston in series with only one (right) valve half. The large pressure drop across the output piston due to sliding friction reduces the pressure drop across the right valve to a less controllable magnitude.

The input sinusoid frequency of 0.50 Hz consistently produces larger net output actuation results compared to the 1.0 Hz runs. Additional frequencies were tested using the highest performance control strategy to better locate the optimal input frequency. The results, shown in Table 4.4, suggest that the optimal operating frequency is located near 0.50 Hz. While higher frequencies are preferred as the larger bandwidth often yields a faster system, frequencies near 0.75 Hz almost completely stop all actuation from occurring. Lower frequencies near 0.25 Hz are also able to produce large output displacements, but the faster frequency of 0.5 Hz is selected for future testing.

Control Strategy	Input-A	Input-B
Right Always “On”	-1/4	-3/8
Left Always “On”	+1 1/4	+ 1/8
Left “On”–MTS(-) and Right “On”–MTS(+)	+3 1/2	+ 3/8
Right “On”–MTS(-) and Left “On”–MTS(+)	- 3/8	- 3/8
Both “Off”–MTS(-) and Left “On”–MTS(+)	+ 1/4	no data
Left “On”–MTS(-) and Both “Off”–MTS(+)	+6 7/8	+ 1/8

Table 4.3: Net displacement produced by the output piston from a sinusoidal input piston waveform ($A = 0.5$ Hz, 2 in p-p amplitude, $B = 1.0$ Hz, 2 in p-p amplitude).

Control Strategy	Input Frequency (Hz)	Net Output (in)
Left “On”–MTS(-) and Both “Off”–MTS(+)	0.25	+4
Left “On”–MTS(-) and Both “Off”–MTS(+)	0.50	+6 7/8
Left “On”–MTS(-) and Both “Off”–MTS(+)	0.75	+ 1/4
Left “On”–MTS(-) and Both “Off”–MTS(+)	1.00	+ 1/8

Table 4.4: Net displacement produced by the output piston using the control strategy of left solenoid “on” for a negative MTS direction input and both solenoids “off” for a positive MTS direction, for a sinusoid input piston waveform (2 in p-p amplitude) of various frequencies.

4.2.4 Automated Solenoid Control

To completely automate the actuation cycle, the manual solenoid activation must be replaced by an automated controller. The main objective of these experiments was to produce controlled actuation using no manual inputs. A secondary objective was to again verify the necessity of MR fluid to produce actuation.

The experimental setup was identical to that shown in Fig. 4.5, but without the manual switch. Also, a precision string potentiometer (Unimeasure LX-PA-20-L2M) was attached to the output piston to record linear actuation. A LabVIEW program was developed to simultaneously record inputs from two separate data acquisition cards, display, process and record data, and to output a solenoid control signal. The acquired signals include the input piston position and load, fluid valve position (laser sensor, SA1d-LK4), output piston position (precision string potentiometer), and two pressure sensors (Sensotec GM-A 992453, 668774). Through a simple algorithm, a voltage signal was sent through an amplifier (MB Dynamics SL500VCF) to the left MR fluid valve half based on the the sign (\pm) of the input force. It is noted that the sign of the input loading was equal to that of the MTS input direction. Details of the program are presented in Appendix B.1.

As previously shown in Fig. 4.6(a), a negative and positive input displacement direction produces flows $F1$ and $F2$, respectively. Fig. 4.7 presents data from the controlled solenoid run where 5 V was applied to the left solenoid during negative input displacement. The output piston motion is in the form of a ramped-sinusoid with an average actuation rate of 0.325 in/s. There exists a large amount of undesired output retraction during negative input piston velocities. This is due to the valve not closing fully to the right side, which is attributed to large sliding friction forces and asymmetries of flow path resistances.

Fig. 4.8 presents data from the uncontrolled solenoid run where no voltage was applied for either input loading. The lack of MR fluid viscosity changes show that conventional

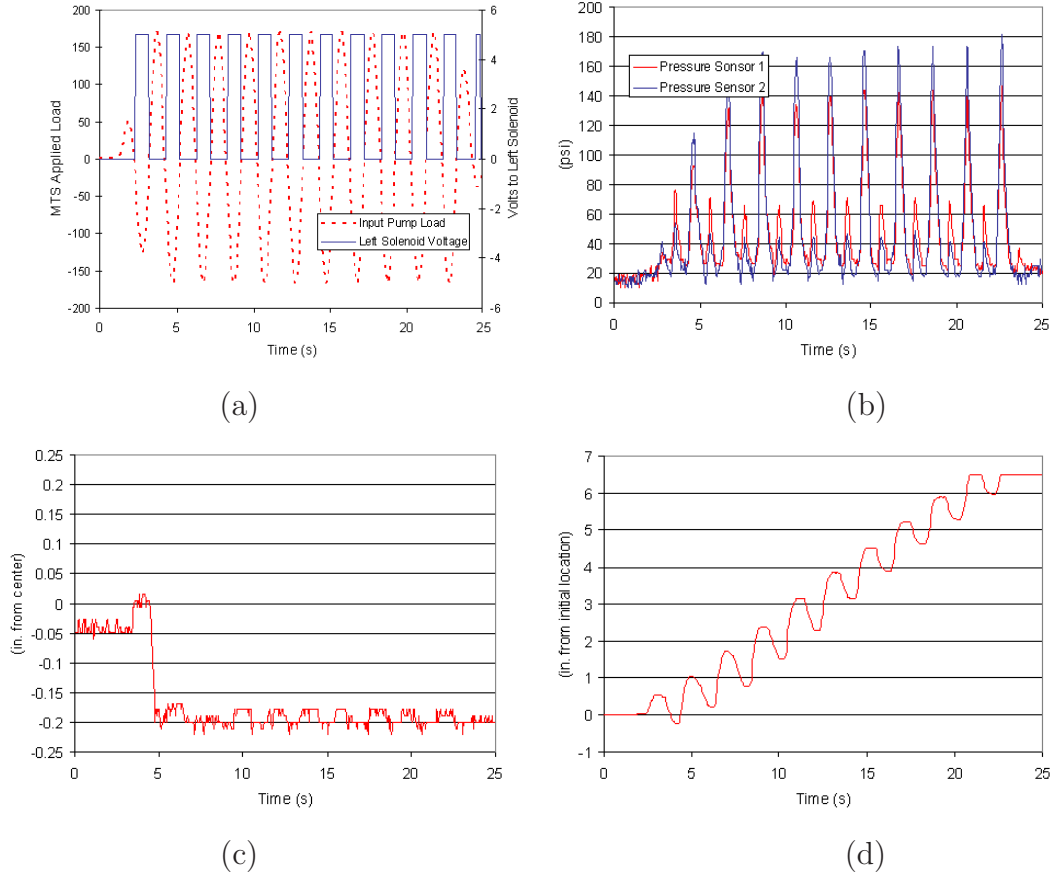


Figure 4.7: Actuation results (a) control strategy for 5 V dc solenoid input and negative (F1) input piston loading (b) line pressures (c) valve location (-0.2 = left valve closed, +0.2 = right valve closed), and (d) output piston position.

hydraulic fluid forces are not large enough to move the valve. Therefore, the output piston is observed to oscillate about a nominal position resulting in no net positive actuation. This verifies the necessity of MR fluid as the working fluid.

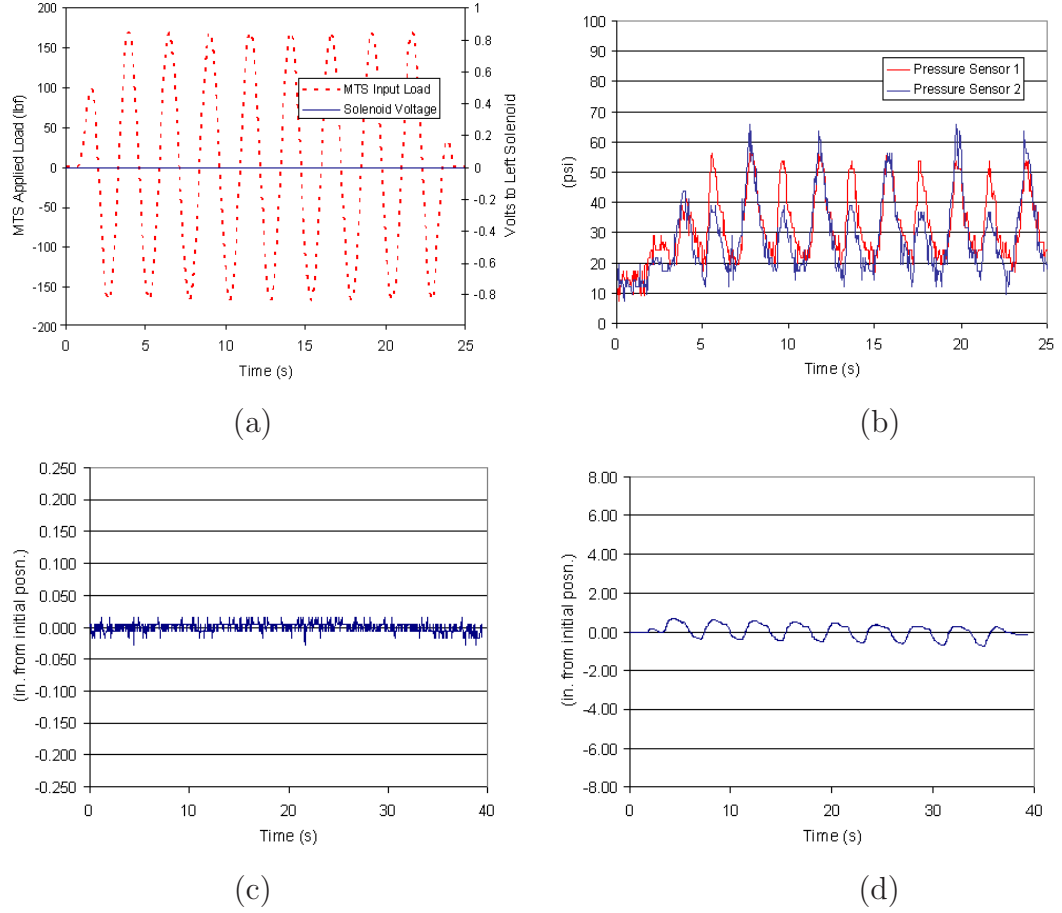


Figure 4.8: Actuation results (a) control strategy - no solenoid inputs for either loading, (b) line pressures, (c) valve location (-0.2 inch is valve not in series with output piston closed), and (d) output piston position.

4.3 Variable Valve Resistance Measurements

4.3.1 Objective and Construction Details

Previous testing characterized the MR fluid valve performance in terms of output actuation. An alternative approach is to measure the variable flow resistances generated through the valve based on independent inputs. The magnitude of resistance increase is an important aspect of the valve controllability and performance. The ideal valve produces zero resistance when open (non-activated) to minimize energy losses and will have infinite resistance when closed (activated) to produce a flow rate of zero. The fluid resistance to

flow produced by the MR fluid valve is dependent upon solenoid voltage, relative valve position, annular gap size, and direction of flow. The objective in this set of experiments was to quantify the variable resistance based on each of these parameters. The values were directly inserted into a system-level model of the hybrid actuator, which is described in Sect. 5.2.

Slight modifications to the LabVIEW program developed for testing in Sect. 4.2.4 and temporary component isolation permitted the analysis of fluid resistance. Fig. 4.9 illustrates the general setup. Individually, each valve half was connected to an input piston (Allenair ED), driven by an MTS as in previous tests. A locking mechanism was constructed to hold a constant axial gap between the conical shaft and seat for the entire period of a run, for isolating the effect of valve gap on resistance. Voltage was kept constant throughout each run by a dc power source (Tektronix CPS250) and linear amplifier (MB Dynamics SL500VCF).

The fluid resistance is defined as

$$R = \frac{P_2 - P_1}{Q_v} \quad (4.1)$$

where Q_v is the volume flow rate, and P_1 and P_2 are the pressures on either side of the resistance element. Two pressure sensors (Sensotec GM-A 992453, 668774) were located at each port to measure P_1 and P_2 .

4.3.2 MR Fluid Valve #1 Resistance

MR fluid valve #1 (annular ring gap of 0.030 in) was inserted into the experimental setup shown in Fig. 4.9(a) for variable resistance analysis. In addition, a new movable valve piece with a smaller conical diameter was constructed to provide an additional annular ring dimension of 0.125 in.

To remove the unwanted dynamic effects from the measurement, a triangular waveform (4 in p-p, 0.25 Hz) was selected as the input piston (MR fluid volume) displacement

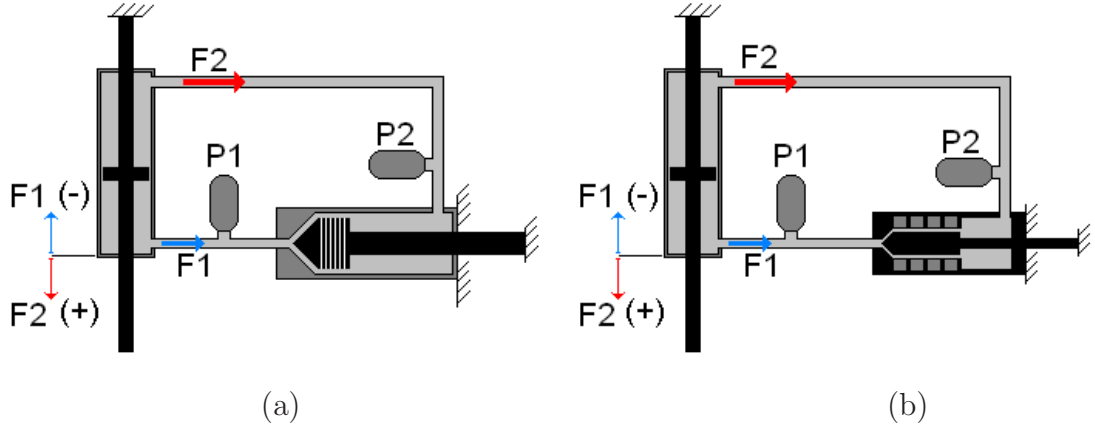


Figure 4.9: Illustration of setup used to determine MR valve resistance for (a) design #1 and (b) design #2. Arrows depict the two flow directions, F1 and F2, based respectively on negative and positive MTS input direction.

as shown in Fig. 4.10(a). Triangular waves have constant derivatives between peaks, effectively minimizing transient effects. The waveform period of 4 seconds was found to be sufficiently long to remove the dynamic effects, but short enough to produce large pressures.

The volume flow rate is

$$Q_v = \frac{dx}{dt} A_p \quad (4.2)$$

where x is the input piston location measured by the MTS position sensor and A_p is the effective input piston cross-sectional area. The position waveform $x(t)$ can be approximated using Fourier Series analysis and subsequently used to calculate the flow rate \tilde{Q}_v ,

$$x(t) = \frac{-17}{\pi^2} \left(\sin(t\pi/2) - \frac{\sin(3t\pi/2)}{9} + \frac{\sin(5t\pi/2)}{25} - \frac{\sin(7t\pi/2)}{49} + \dots \right) \quad (4.3)$$

$$Q_v(t) = \frac{-17}{\pi} \left(\cos(t\pi/2) - \frac{\cos(3t\pi/2)}{3} + \frac{\cos(5t\pi/2)}{5} - \frac{\cos(7t\pi/2)}{7} + \dots \right) \quad (4.4)$$

Equation 4.4 was difficult to implement in practice due to the large waveform distortion found even when using a large number of terms in the series. An alternative approach is to use piecewise derivatives over each constant slope and manually insert the constant

flow rate into the resistance equation. The later equation produces cleaner results and was therefore implemented. The volume flow rate input is shown in Fig. 4.10(b). It is noted that the input flow rate waveform for all resistance runs were equal. However, the force input by the MTS machine was found to vary significantly from run to run, as it is dependent on the resistance of the fluid path.

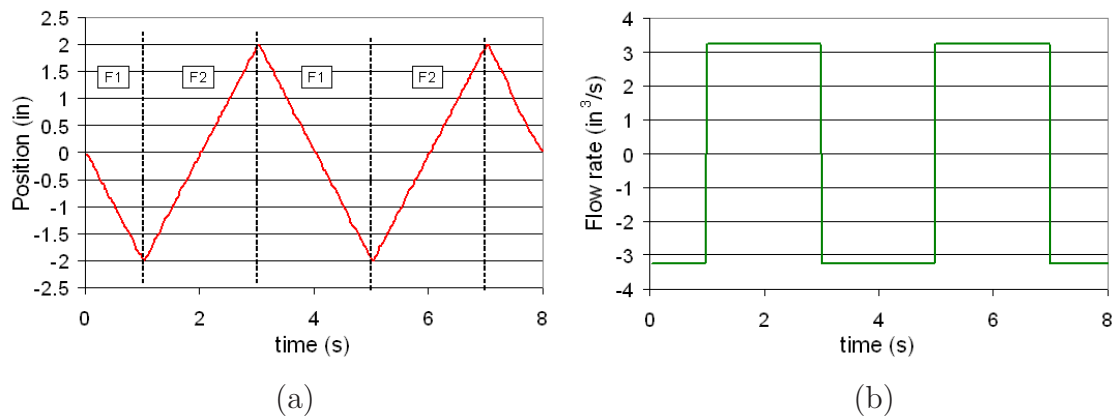


Figure 4.10: (a) Input waveform recorded with MTS machine's position transducer, and (b) the calculated input flow rate for resistance testing of MR fluid valve device #1.

As an example, in Fig. 4.11(a) are the line pressures for the 0.030 in annular gap, 10 V input, and 0.125 inch axial gap (axial distance from closure) run. The valve shaft was rigidly held to maintain a constant axial gap for each resistance test. It is noted that for future fluid flow analysis, it is necessary to convert the axial gap to perpendicular flow gap as shown in Fig. 3.5. The difference between the line pressures is the pressure drop across of the valve, as shown in Fig. 4.11(b). The pressure differentials are positive and negative for flow directions $F2$ and $F1$, respectively. The calculated resistance is shown in Fig. 4.11(c).

The average resistance values for each annular gap size, 0.030 in and 0.125 in, are summarized in Tables. 4.5 and 4.6, respectively. Based on these results, the maximum

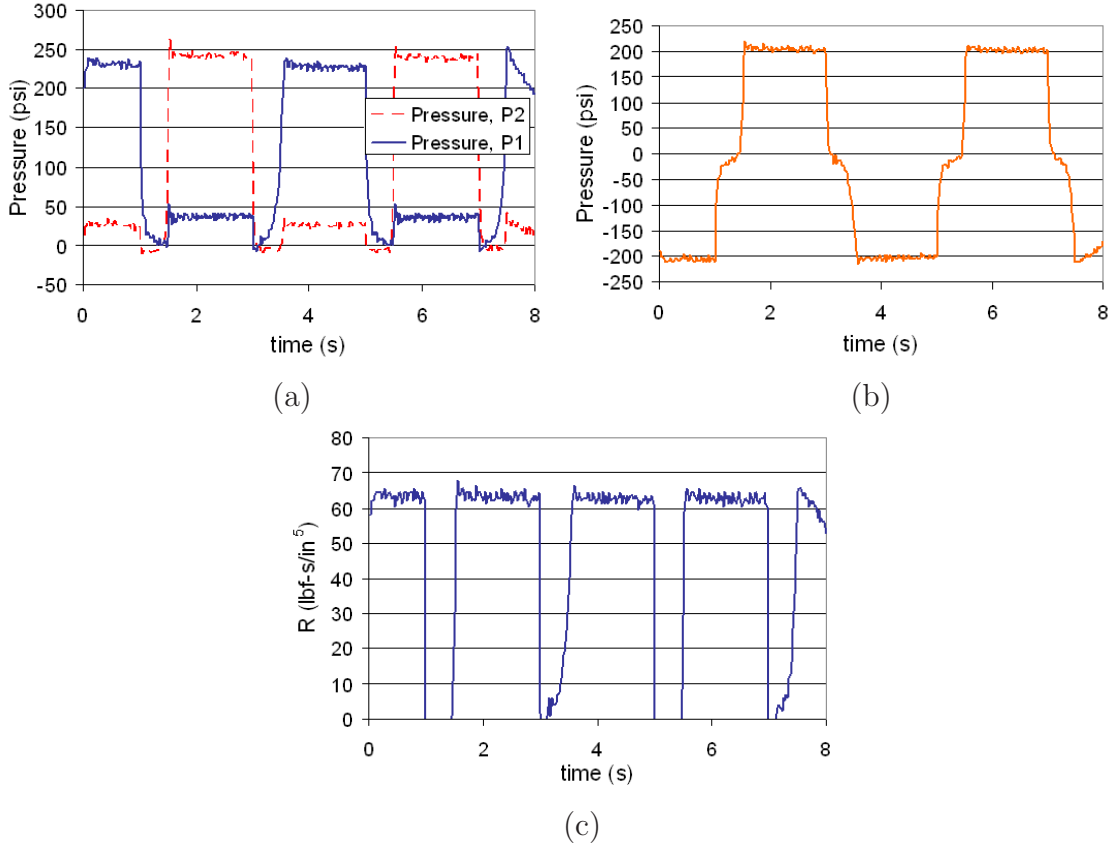


Figure 4.11: MR fluid valve (#1), left valve, 10 V, 0.125 in gap resistance test data; (a) line pressure, (b) pressure differential, and (c) resistance data.

resistance of 100 lbf·s/in⁵ is produced with at an annular gap of 0.030 in, 10 V input, and an axial gap of 0.036 inch. The larger annular ring gap runs consistently produce lower resistances than the original MR fluid valve #1. The minimum resistance recorded is near 10 lbf·s/in⁵ for all zero voltage runs. Therefore, the fluid flow resistance can be increased by a factor of 10 using MR fluid valve #1.

Voltage (V)	Axial Gap (in)	Resistance F1	Resistance F2
0	.250	11	12
0	.125	11	12
0	.075	12	12
0	.057	16	17
0	.036	20	20
5	.250	49	50
5	.125	52	53
5	.075	45	46
5	.057	72	74
5	.036	84	91
10	.250	56	58
10	.125	60	60
10	.075	52	53
10	.057	80	82
10	.036	93	100

Table 4.5: Average resistance measurements (lbf·s/in⁵) of MR fluid valve #1 for fixed annular gap of 0.030 in, axial gap, solenoid voltage, and flow direction (F1, F2).

Voltage (V)	Axial Gap (in)	Resistance F1	Resistance F2
0	.250	9	9
0	.125	9	9
0	.075	9	10
5	.250	16	17
5	.125	18	18
5	.075	21	22
10	.250	19	19
10	.125	20	21
10	.075	19	19

Table 4.6: Average resistance measurements (lbf·s/in⁵) of MR fluid valve #1 for a modified fixed annular gap of 0.125 in, axial gap, solenoid voltage, and flow direction (F1, F2).

4.3.3 MR Fluid Valve #2 Resistance

At this stage of the research, a new MR fluid valve was designed and developed with the goals of decreasing overall size and increasing resistance performance. The first goal was successfully accomplished as discussed in Section 3.3.2. To test the performance, MR fluid valve #2 was inserted into the experimental setup shown in Fig. 4.9(b) for variable resistance analysis. Again, the valve shaft was rigidly held to maintain a constant axial gap throughout the duration of each run.

To remove unwanted dynamic effects from the measurement, a triangular waveform (2 in p-p, 0.25 Hz) was selected as the displacement applied by the MTS machine to the input piston. The waveform amplitude was reduced from that used in previous measurements due to the smaller internal volume of the valve. Using piecewise derivatives, the input volume flow rate for all valve #2 resistance runs is shown in Fig. 4.12(a).

As an example, Fig. 4.12(b) is the line pressures for the 0.030 in annular gap, 10 V input, and 0.055 in axial gap (axial distance from closure) run. The difference between the line pressures is the pressure drop across of the valve, as shown in Fig. 4.12(c). The pressure differential is positive and negative for flow directions $F2$ and $F1$, respectively. The calculated resistance values are shown in Fig. 4.12(d). Both valve halves (A and B) were tested, and the results for each are summarized in Tables 4.7 and 4.8.

The maximum resistance produced is 172 lbf·s/in⁵ from valve (A) with a 10 V input. This accounts for a 72 percent increase in performance over the 570 percent larger MR fluid valve #1. As shown by the constant axial gap plots of the resistance data in Fig. 4.13, MR fluid valve #2 has not yet reached its maximum resistance potential. For the solenoid stacks tested within the valve, voltages higher than 10 V produced significant self-heating. Thus, the input voltage limit was kept below the level at which the MR fluid could fully

Voltage (V)	Axial Gap (in)	Resistance F1	Resistance F2
0	.205	10	18
0	.140	10	19
0	.055	10	17
3	.205	73	73
3	.140	73	73
3	.055	70	65
6	.205	52	53
6	.140	121	127
6	.055	124	124
10	.055	172	172

Table 4.7: Average resistance measurements (lbf·s/in⁵) of MR fluid valve #2(A) for fixed annular gap of 0.030 in, axial gap, solenoid voltage, and flow direction (F1, F2).

Voltage (V)	Axial Gap (in)	Resistance F1	Resistance F2
0	.192	8	14
0	.132	12	9
0	.062	9	11
6	.192	93	93
6	.132	93	96
6	.062	104	100
10	.192	140	140
10	.132	138	135
10	.062	140	149

Table 4.8: Average resistance measurements (lbf·s/in⁵) of MR fluid valve #2(B) for fixed annular gap of 0.030 in, axial gap, solenoid voltage, and flow direction (F1, F2).

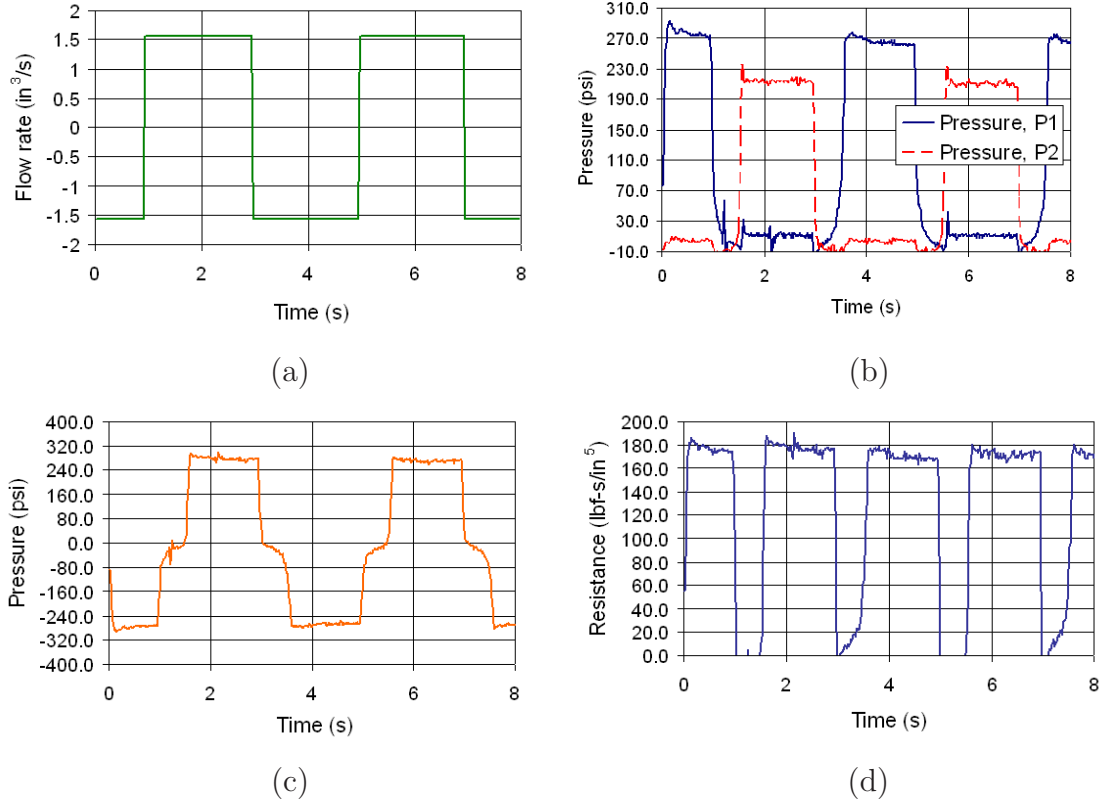
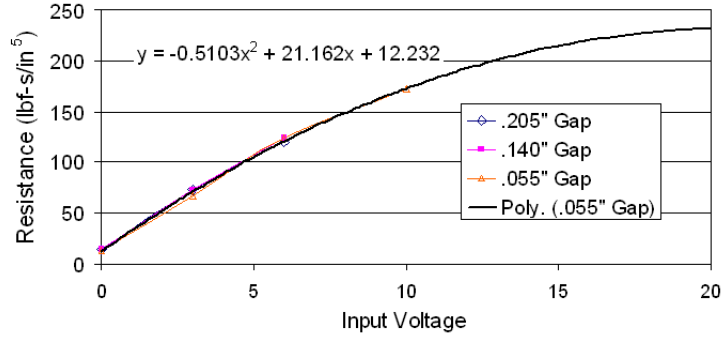


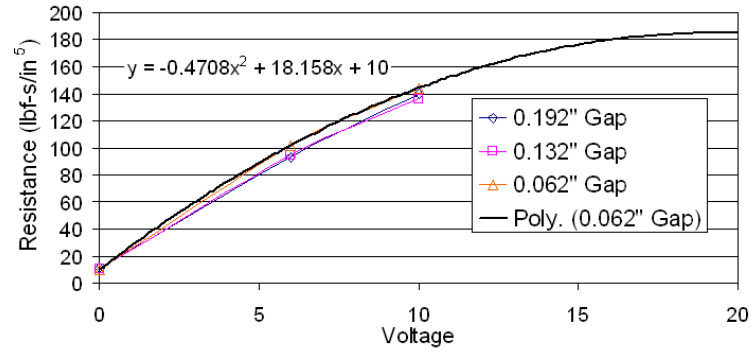
Figure 4.12: MR fluid valve device #2, 10 V input, 0.055 in axial gap resistance testing data; (a) input flow rate, (b) line pressures, (c) pressure differential, and (d) resistance.

saturate. The extrapolated curve fit predicts the maximum resistance to occur in the range of 200–250 $\text{lbf}\cdot\text{s}/\text{in}^5$ with an input of 20 V.

Similar to MR fluid valve #1, valve #2 produces a minimum resistance near 10 $\text{lbf}\cdot\text{s}/\text{in}^5$ for 0 V input at all axial gap distances. Therefore, MR fluid valve #2 increases fluid flow resistance by a factor greater than 17 times. The resistance ratio is expected to increase to more than 20 with minor solenoid modifications.



(a)



(b)

Figure 4.13: Projected resistance fits to data for MR fluid valve #2 for (a) valve (A) and (b) valve (B).

4.4 Characterization of Unidirectional Magnetostrictive Pump

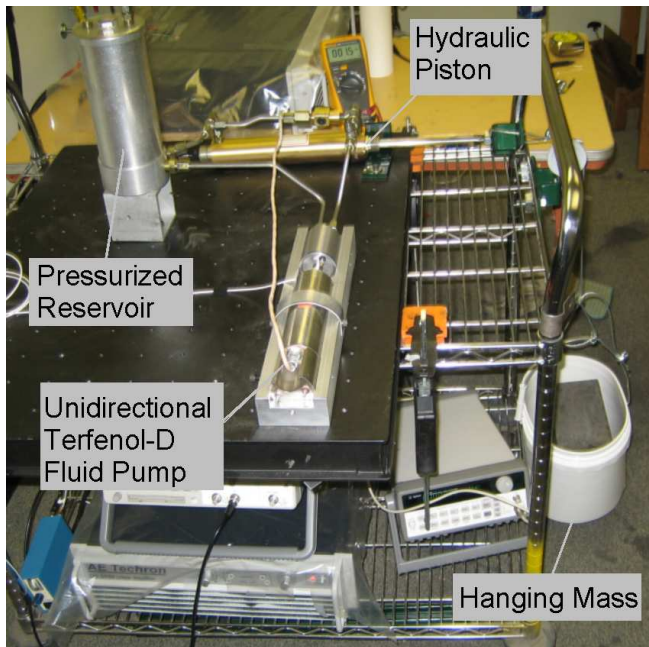
4.4.1 Objective and Construction Details

All previous testing implemented a traditional hydraulic piston powered either manually or through a universal compression-tension machine. These input sources were temporary replacements of the Terfenol-D fluid pump included in the hybrid actuator concept described in Sect. 3.1. A major step in the advancement of the hybrid actuator was to replace the bulky and impractical inputs used in previous testing, with that of a Terfenol-D fluid pump. This pump uses two passive check valves to produce a unidirectional flow of MR fluid. Performance is limited by the frequency bandwidth of the check valves.

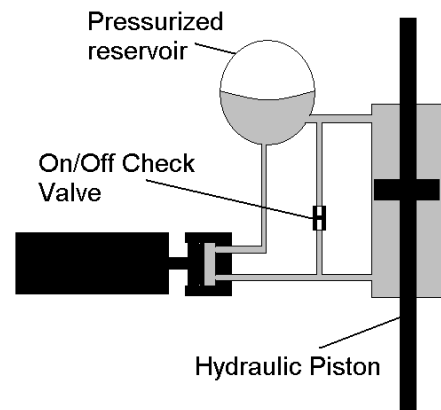
The first of two experimental setups used in this section was constructed for impedance and resonance testing of the Terfenol-D transducer supplied by Etrema Products, Inc. (Ames, Iowa). The transducer was fitted with an aluminum piston, which was connected to the output pushrod. The transducer and aluminum piston were suspended horizontally from nylon cords which were attached to a rigid frame on the floor. The purpose of this support fixture was to minimize impedance effects from other surrounding sources (i.e. table vibrations). An accelerometer (PCB-76645) was attached to the piston to measure axial acceleration produced by the transducer. An input frequency sweep was generated by the DataPhysics hardware (SignalStar Vector) and software (SignalCalc Mobilizer). A dc bias of -0.65 mV was added to the DataPhysics output to center the sinusoid about 0.00 V, before being amplified by two amplifiers (Techron 7780) connected in series.

The second of two experimental setups used in this section was constructed to measure output flow properties. The performance of the unidirectional fluid pump is dependent on the input signal's voltage and frequency and the load which the pump must work against. The pump's performance limits are defined by the unloaded volume flow rate and the loaded blocking pressure. The values between these two maxima is the usable range for actuation. To quantify the loading versus volume flow rate, the experimental setup shown in Fig. 4.14 was constructed. The setup consisted of a unidirectional Terfenol-D fluid pump, hydraulic piston (Allenair ED), and pressurized reservoir (Lube Devices; A OR12053-3) connected in series. Due to the pump's directional check valves prevention of reverse flow, a manual "on"/"off" type check valve was routed parallel to the piston to permit manual repositioning of the system. The hydraulic piston was used to measure volume flow rate and for loading of the pump. The pressurized reservoir assisted the Terfenol-D pump in drawing fluid into the system to prevent cavitation, which is described as the formation of cavities or air bubbles within a fluid due to mechanical forces or a vacuum lowering the local pressure below the fluid vapor pressure. The reservoir created a bias pressure imposed

on the entire fluid network which the fluid pump must add to. High bias pressures facilitate the drawing of fluid into the chamber, but at the expense of larger forces the pump must work against to increase the pressure differential across the hydraulic piston and produce volume flow. Conversely, a low pressure bias will represent a smaller load for the pump to work against, but will more easily cavitate the MR fluid. A signal generator (Agilent 33120A) and amplifier (AE Techron; LVC5050) were used to power the Terfenol-D pump for various sinusoidal waveforms. The load was applied through a hanging mass (lead bricks, 23.7 lbs each) attached to the piston rod and pivoting about a pulley.



(a)



(b)

Figure 4.14: (a),(b) Experimental setup used to characterize the performance limits of the unidirectional Terfenol-D fluid pump.

4.4.2 Terfenol-D Transducer Resonance

Using the horizontally-mounted transducer, a swept frequency sinusoid was input to the device to locate the system resonance. The importance of this quantity is evident from

the measurements shown in Fig. 4.15(a). Using a moderate drive level of 5.09 V-rms (below the rated continuous operation rating of 5.8 V-rms) the magnitude of the transfer function acceleration per current reaches a peak near 2660 Hz. The 2660 Hz resonant frequency is orders of magnitude larger than at lower frequencies.

The ideal pump operating conditions are at maximum displacement per pump cycle and the maximum pump cycle rate. This increases the work output per cycle, while maximizing the iterations of work production. Therefore, it is desired to operate the pump near the resonant frequency. It is noted that the unidirectional Terfenol-D pump will not be able to operate near the resonant range due to the passive directional flow check valves which have a resonance below 200 Hz.

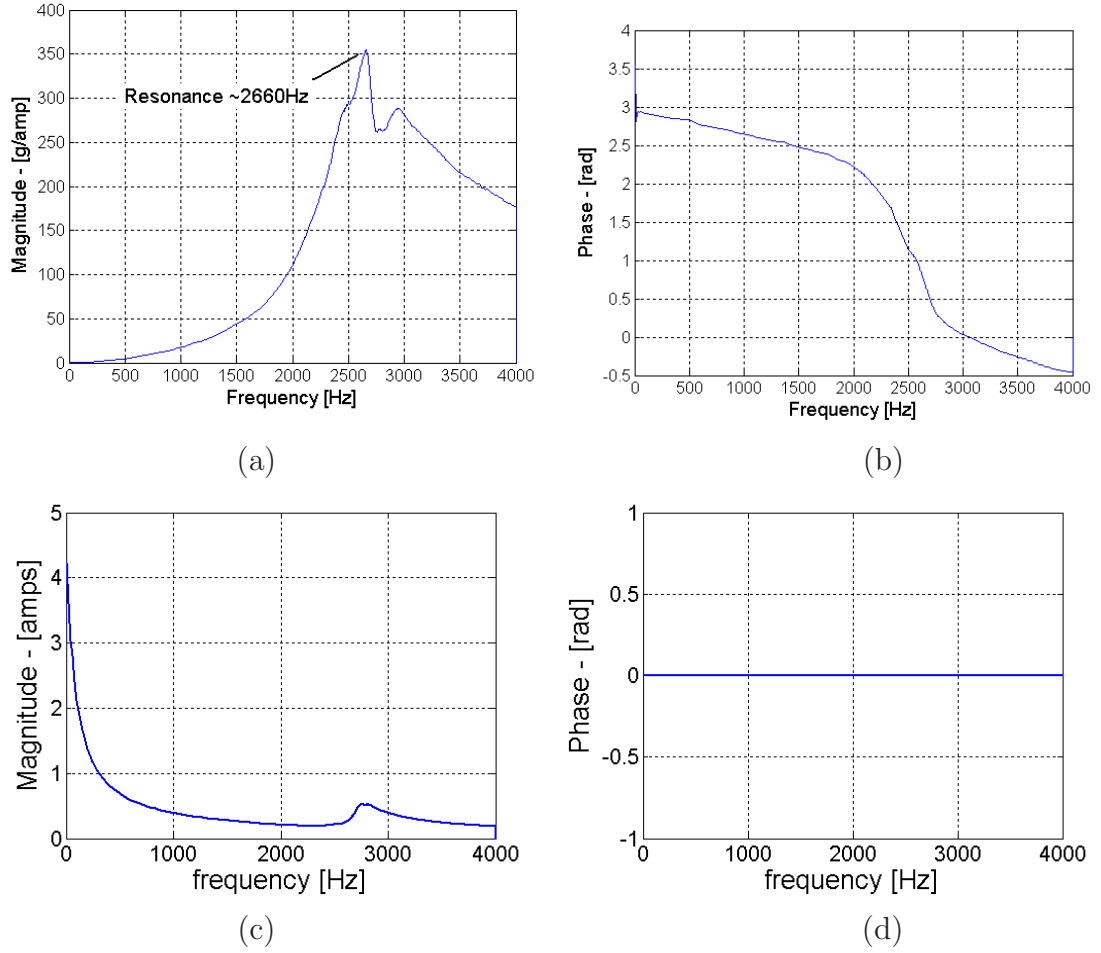


Figure 4.15: Frequency response for acceleration per current of Terfenol-D transducer (a) magnitude and (b) phase. This response shows resonance at 2660 Hz. The associated input current spectral density (c) magnitude and (d) phase.

4.4.3 Operating Bias Pressure

Tests were performed using the second experimental setup shown in Fig. 4.14 to determine the average pressure bias to optimize the performance of the Terfenol-D pump. The reservoir is capable of safe operation up to 125 psi. Varying only the pressure bias, Fig. 4.16 shows three pressures which produce the largest unloaded volume flow rates. It is noted that the volume flow rate is calculated through static measurements of distance traveled by the output piston, multiplied by the effective piston area (1.57 in^2), and divided by the

duration of the run (60 seconds). From these results, 40 psi is selected as the average bias pressure for improved pump performance.

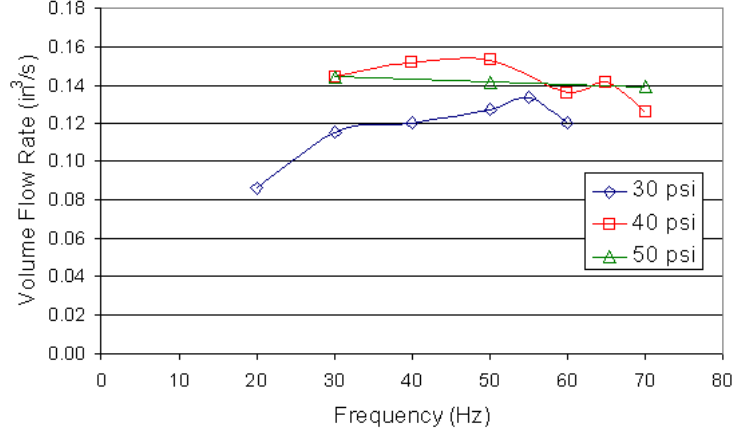


Figure 4.16: Unidirectional Terfenol-D pump performance for varying pressure bias.

4.4.4 Pump Performance

Additional testing of the pump was conducted through a sweep of the remaining three inputs; voltage amplitude, signal frequency, and hanging mass. Similar to previous testing, the volume flow rate was calculated from the output piston's distance traveled and the duration of the run (15 seconds). The voltages range from the rated continuous duty voltage (5.8 V-rms) to an intermittent voltage of 8.5 V-rms. It is noted that larger voltages produce larger pump deflections and forces, but also increase the self-heating produced by the pump's solenoid. Therefore, larger voltages than those used in this testing can be used for short durations of time to further increase performance. The results for varying frequencies and constant voltage are shown in Fig. 4.17. The results for varying voltage and constant frequencies are shown in Fig. 4.18.

The maximum volume flow rate produced by the Terfenol-D pump is $0.25 \text{ in}^3/\text{s}$. As expected, this occurs with no load and at the highest input voltage tested. Similar to the data shown in Fig. 4.16, a 50–60 Hz input frequency produces the largest flow rates. This is assumed to be the resonance of the passive check valves located in the pump chamber. The maximum blocking pressure recorded is approximately 75 psi, at the largest input voltage tested. It is observed that at a pressure load between 5 and 15 psi, an optimal frequency “crossover” occurs. The optimal frequency decreases in all three constant voltage runs to 30 Hz with an applied load of at least 15 psi.

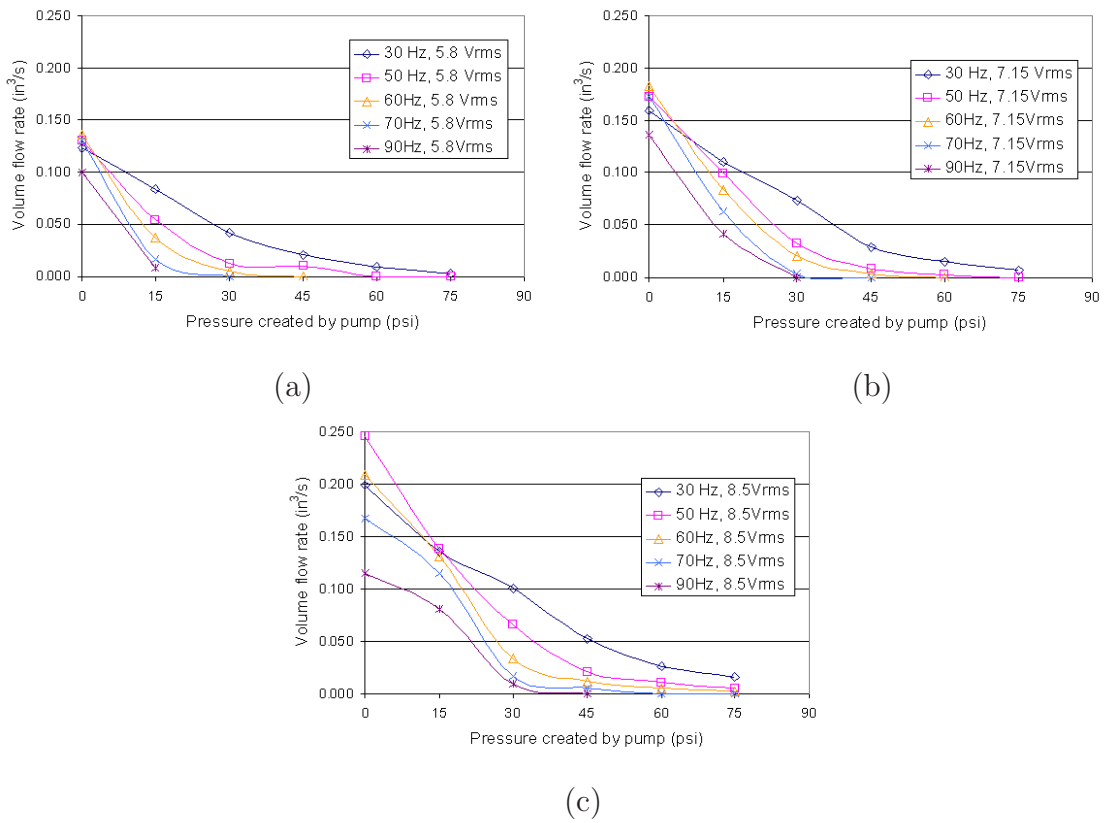
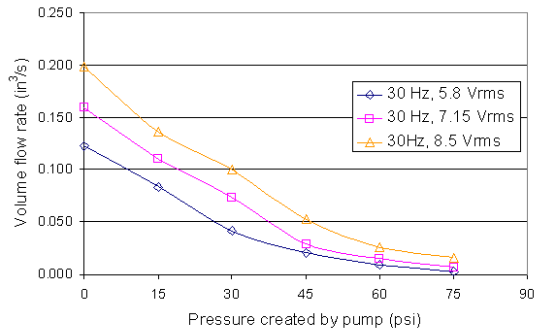
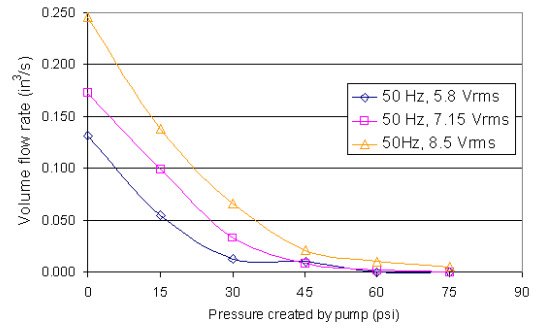


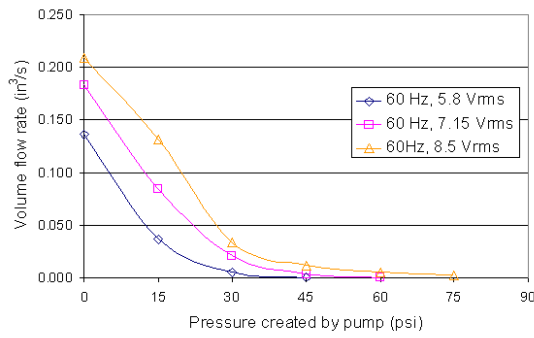
Figure 4.17: Performance of unidirectional Terfenol-D pump for (a) constant 5.8 V rms input, (b) constant 7.15 V rms input, and (c) constant 8.5 V rms input.



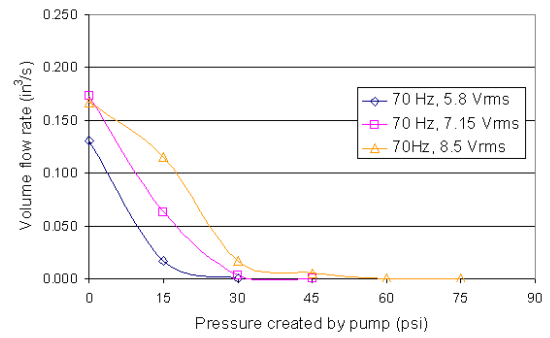
(a)



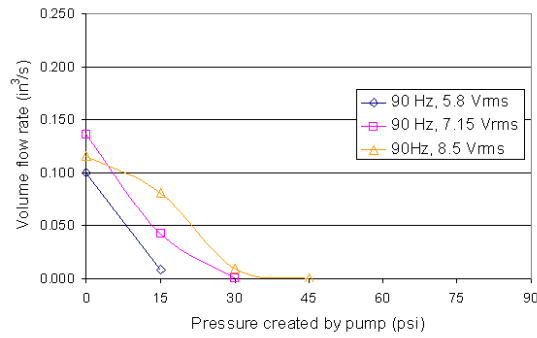
(b)



(c)



(d)



(e)

Figure 4.18: Performance of unidirectional Terfenol-D pump for (a) constant 30 Hz input, (b) constant 50 Hz input, (c) constant 60 Hz input, (d) constant 70 Hz input, and (e) constant 90 Hz input.

CHAPTER 5

MODELING

This chapter is focused on the development of a system-level model of the hybrid actuator. Two equation sets, model #1 and model #2, are outlined in this chapter, both of which are constructed from the same general framework and verified with experimental results of Chapter 4. Model #2 is an enhancement of Model #1.

5.1 System Model #1 - Force Balance

5.1.1 Model #1 Development

A system-level model of the experimental actuator setup in Sect. 4.1.1 was developed for concept verification and system analysis. There are multiple physical domains that are coupled within the system, including electric, magnetic, fluid, and mechanical domains. To outline briefly, the input piston converts mechanical displacement to fluid pressure p and volume flow rate Q_v . The solenoids within the fluid valve convert an electrical input to a magnetic field, which in return increases the fluid viscosity. The fluid viscosity effects a pressure change across the MR fluid valve, which produces a mechanical valve motion, y . The mechanical valve position and fluid viscosity varies the flow path resistances R and flow rates, which control the output piston motion z and force. Modeling all of these coupled domains is desired for system analysis and parameter identification. Fig. 5.1 outlines the actuator system and the associated model variables.

The four controllable inputs are the pressure p_1 and MR volume flow rate Q_v generated by a displacement x of the hydraulic pump, and two independent voltages V_l and V_r , one to each solenoid. Application of the inputs to the model yields time trace solutions for line pressures, flow rates, mechanical forces, and valve position.

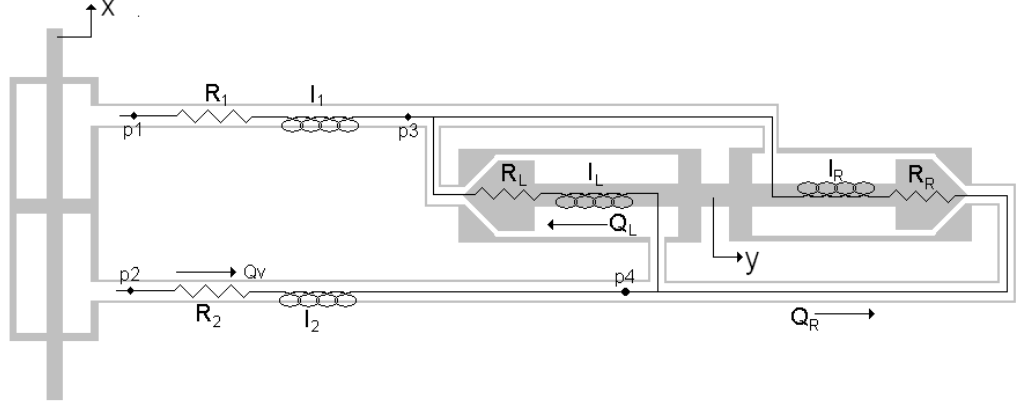


Figure 5.1: System-level representation of experimental setup using hydraulic input piston and double-sided valve design #1, without an output piston. The fluid flow is modeled by equivalent resistance and inductance elements.

The valve location y is determined by Newton's law with maximum displacement limits due to the rigid housing. This is modeled as a highly non-linear spring and damper in parallel between the movable mass and rigid housing. The free body diagram for the forces imposed on the movable valve piece is shown in Fig. 5.2, which includes fluid pressure forces F_{pll} , F_{plh} , F_{prh} , and F_{prl} at all four fluid valve ports, Coulomb friction force F_f from the sleeve bushings and seals needed to support the movable connecting rod, fluid damping forces F_{dl} and F_{dr} , and non-linear spring-damper pairs F_s and F_b to limit motion. These

forces are calculated individually by

$$\sum F = M \frac{d^2 y}{dt^2}, \quad (5.1)$$

$$F_p = p_3 A_{low} + p_3 A_{high} - p_4 A_{low} - p_4 A_{high}, \quad (5.2)$$

$$F_f = f_c \operatorname{sgn}\left(\frac{dy}{dt}\right), \quad (5.3)$$

$$F_d = (\tau_y(H) + \tau \dot{\gamma}) A_s, \quad (5.4)$$

$$F_s = k(y)y, \quad (5.5)$$

$$F_b = c(y) \frac{dy}{dt}, \quad (5.6)$$

where M is the mass of the valve, A_{low} and A_{high} are projected pressure areas, and A_s is the shear area. f_c is an estimated Coulomb friction coefficient, and $k(x)$ and $c(x)$ are approximated with large values (infinity) at housing limits and small (negligible) values within housing limits. The fluid damping is modeled after the viscoplastic Bingham model, as described in Sect. 2.3.2, with the shear rate $\dot{\gamma}$ always positive. Numerical values for fluid yield stress τ_y are best fit approximations from experimental data shown in Figs. 2.5(b),(c).

Each MR fluid line within the closed network is modeled as a fluid resistance in series with a fluid inductance, as illustrated in Fig. 5.1. The use of stiff steel lines in the design is estimated to produce negligible wall capacitance. Furthermore, the oil-based fluid was assumed incompressible. The pressure differential across a fluid resistance R and inductance I element is

$$\Delta p = R Q_v, \quad (5.7)$$

$$\Delta p = I \frac{dQ_v}{dt}. \quad (5.8)$$

Therefore, the pressure differentials over various line segments are

$$p_1 - p_3 = R_1 Q_v + I_1 \frac{dQ_v}{dt}, \quad (5.9)$$

$$p_4 - p_3 = R_r Q_{vr} + I_r \frac{dQ_{vr}}{dt}, \quad (5.10)$$

$$p_4 - p_3 = R_l Q_{vl} + I_l \frac{dQ_{vl}}{dt}. \quad (5.11)$$

Numerical values for both resistance R and inductance I through the hard steel lines of circular cross section (not through valve) are independent of the input parameters, therefore permitting direct calculation using the equations

$$R_1 = R_2 = \frac{128\mu L}{\pi d^4}, \quad (5.12)$$

$$I_1 = I_2 = 2 \left(\frac{\rho}{A} \right) L, \quad (5.13)$$

where μ is the absolute viscosity, ρ is the MR fluid density, and L , A , and d are the length, cross sectional area, and diameter of each fluid line section. Equation (5.12) is valid for laminar flow, and equation (5.13) is valid for a parabolic flow profile [26]. The variable flow resistances through each valve half (R_r and R_l) are functions of the valve location y and the input voltages to the solenoids V_l and V_r , which permits coupling of the fluid equations to those of the mechanical valve motion. Discrete approximations of resistance at various closure fractions and magnetic fields H were made, allowing for linear interpolation between values. The fully-closed valve with magnetic field present creates an order of magnitude greater resistance than that of fully-open valve and $H = 0$. It is noted that in the next model iteration, experimentally measured values of variable valve resistance were obtained and implemented.

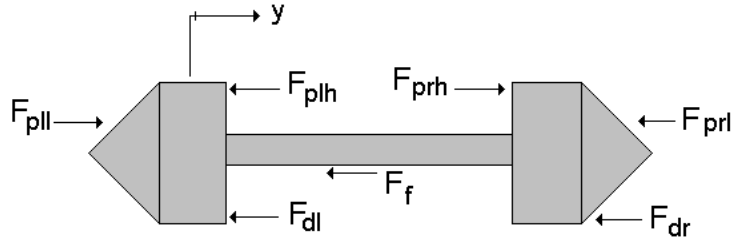


Figure 5.2: Mechanical model of valve.

The total volume flow divides into two fluid paths connected in parallel while observing the conservation of mass laws,

$$Q_v = Q_{vr} + Q_{vl}, \quad (5.14)$$

$$\frac{dQ_v}{dt} = \frac{dQ_{vr}}{dt} + \frac{dQ_{vl}}{dt}. \quad (5.15)$$

Here, Q_{vr} is the volume flow rate of MR fluid through the right valve half, and Q_{vl} is the volume flow rate through the left. This permits calculation of the volume flow rates through each valve half as a function of the variable valve-half resistances by setting equations (5.10) and (5.11) equal and solving (5.14) and (5.15) for Q_{vr} and $\frac{dQ_{vr}}{dt}$. The resulting flow divider equation is

$$(R_r + R_l)Q_{vr} + (I_r + I_l)\frac{dQ_{vr}}{dt} = R_rQ_v + I_r\frac{dQ_v}{dt}. \quad (5.16)$$

These equations were assembled in a Matlab-Simulink block diagram program for numerical solving. Additional details of the program and corresponding run script can be found in Appendix B.3.1.

5.1.2 Model #1 Results

The system of equations for model #1 were solved using the control strategy outlined in Sect. 4.1.3. The numerical output produces the typical result set shown in Fig. 5.3. The solenoid control was alternated between the right and left valves in coordination with the appropriate fluid flow direction. The input pressure and volume flow rate are sinusoids and the input solenoid voltages are square waves. This is similar to the manual experimental inputs produced by the manual hydraulic cylinder and the DPDT switch. As observed experimentally with no output piston attached to the system, Figs. 5.3(d) and 5.4 show the output valve oscillating between left closed and right closed. All quantities have symmetry between the limits, which is expected due to the symmetry of the model. The addition of an output piston to one fluid path will eliminate this symmetry.

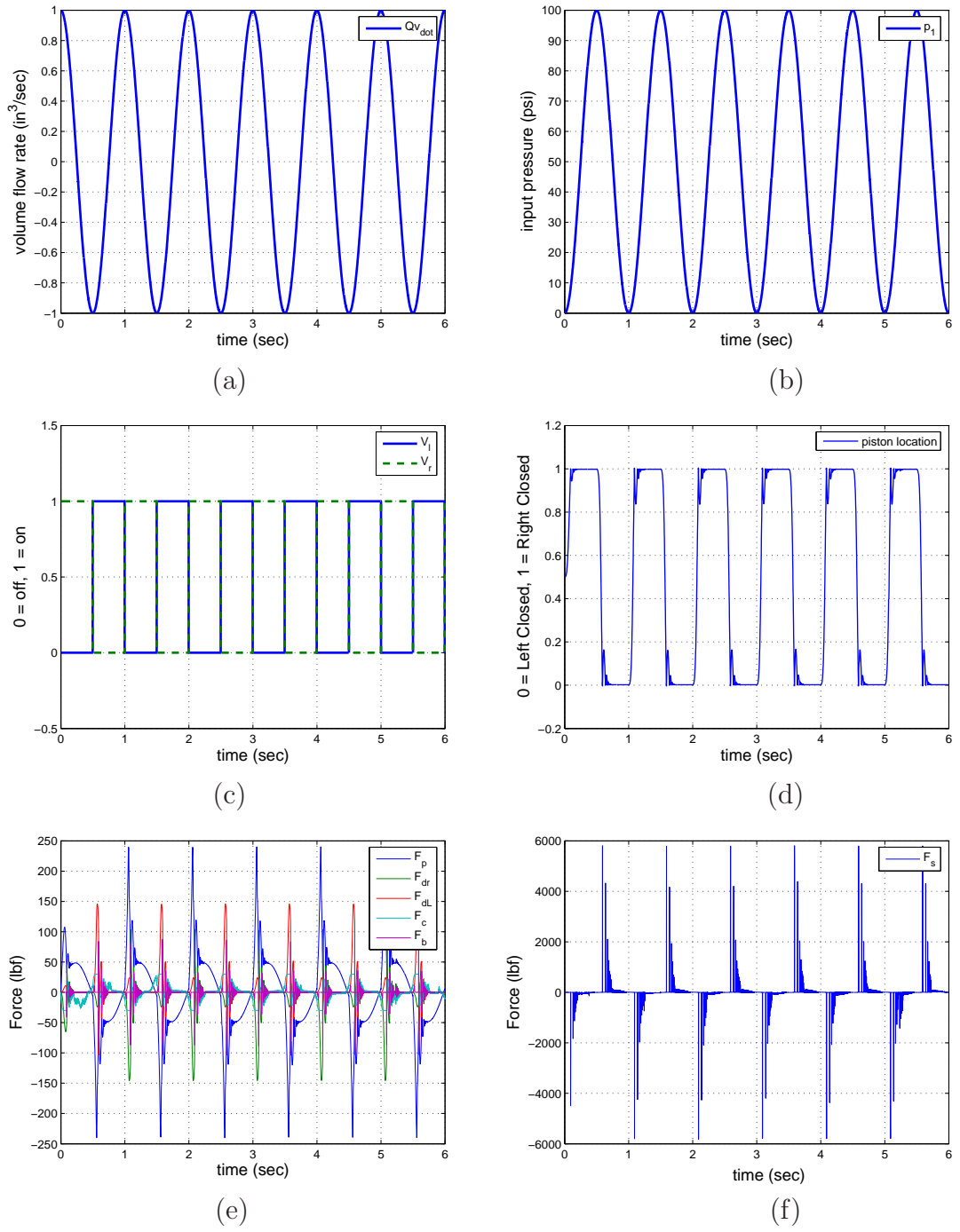


Figure 5.3: System-level model #1 output example (a) input volume flow rate, (b) input fluid pressure, (c) input voltages (solenoid “on” / “off”), (d) output valve position, (e) forces imposed on valve, and (f) the high amplitude, high frequency spring force used to simulate the motion limit imposed by rigid housing.

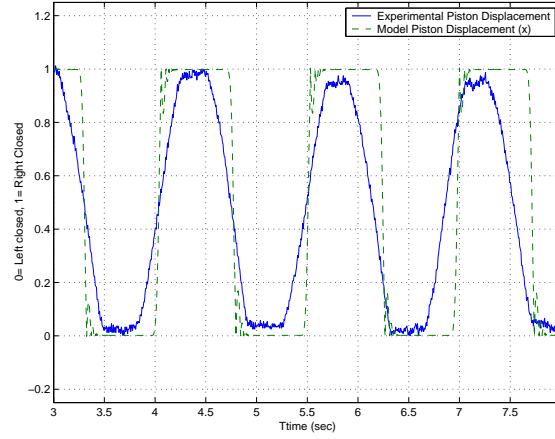


Figure 5.4: System-level model #1, comparison of actuator output with experimental data.

One benefit of modeling the actuator system in this fashion is that individual inputs can be adjusted for control, as well as several force and geometric parameters. This permits the user to investigate the effects of a large number of design changes. There are some inherent problems, however, which also result from this modeling strategy. In particular, the program is highly unstable due to non-linearities caused by friction forces, rigid housing constraints, and step changes in fluid viscosity. Figs. 5.3(e),(f) show the large parasitic vibrations generated by the highly nonlinear housing constraints. These strong dynamic effects make accurate parameter identification difficult.

5.2 System Model #2 - Volume Stored

5.2.1 Model #2 Development

The first system-model iteration incorporated multiple domains where energy was converted between electrical, fluid, and mechanical domains via coupling equations. However, the model construction mandates the use of unideal system inputs, which renders the simulations cumbersome and complex. Furthermore, highly nonlinear terms make the model unstable. An improved system-level model is thus desired that addresses these shortcomings. Specifically, a better selection of input quantities, higher stability, and output actuation predictions are desired. The modeling strategy is that of fluid leakage and fluid stored. By modeling the quantity of fluid flowing past a particular location (leakage) compared to the total volume flowing in, the stored fluid volume is easily obtained. For the movable valve and output piston, this allows direct calculation of position.

This model primarily uses fluid equations and experimental data in look-up tables to calculate system outputs. The system is described by Fig. 5.5, and is analogous to the experimental setup presented in Sect. 4.2.1 which consists of a universal compression-tension machine to input a displacement and force to an input hydraulic cylinder. Also, in contrast to model #1, model #2 incorporates an output hydraulic cylinder to perform actuation.

Controlled inputs to the model are “on”/“off” saturation voltages for the left V_L and right V_R solenoid, acceleration \ddot{x} of the input hydraulic piston, and the force F_1 required to accelerate the input piston of mass M . The following set of equations provides a solution for the input pressure differential $p_2 - p_1$ by means of Newton’s Second Law, force balancing,

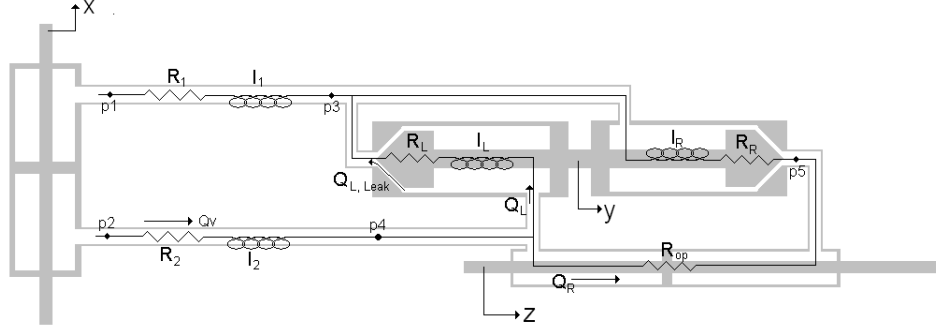


Figure 5.5: System-level representation of the experimental actuator used in model #2.

flow resistance, and volume flow rate Q_v .

$$\sum F = M \frac{d^2 x}{dt^2} \quad (5.17)$$

$$F_1 + p_1 A_{ip} - p_2 A_{ip} = M \frac{d^2 x}{dt^2} \quad (5.18)$$

$$p_2 - p_1 = \frac{F_1 - M \ddot{x}}{A_{ip}} \quad (5.19)$$

$$Q_v = \frac{dx}{dt} A_{ip}. \quad (5.20)$$

Here, A_{ip} is the cross sectional area of the input piston. Assuming negligible fluid capacitance due to the stiff lines and incompressible fluid, then all pressure loss occurs from resistance and inertia effects. Since R_1 and I_1 are approximately equal to R_2 and I_2 , both variables are set equal as R and I . Assigning a constant fluid resistance to the output piston R_{op} , the pressure differentials are given by

$$p_4 - p_3 = p_2 - p_1 + 2(RQ_v + I \frac{dQ_v}{dt}), \quad (5.21)$$

$$p_4 - p_3 = R_L Q_L + I_L \frac{dQ_L}{dt}, \quad (5.22)$$

$$p_5 - p_3 = R_R Q_R + I_R \frac{dQ_R}{dt}, \quad (5.23)$$

$$p_4 - p_5 = R_{op} Q_R, \quad (5.24)$$

$$p_4 - p_3 = R_R Q_R + I_R \frac{dQ_R}{dt} + R_{op} Q_R. \quad (5.25)$$

Similar to model #1, the fluid parameters for a circular cross-section fluid lines and parabolic flow are estimated by [26]

$$R = \frac{128\mu L}{\pi d^4}, \quad (5.26)$$

$$I = 2 \left(\frac{\rho}{A} \right) L. \quad (5.27)$$

The total flow volume is divided into two fluid paths connected in parallel, with conservation of mass laws

$$Q_v = Q_R + Q_L, \quad (5.28)$$

$$\frac{dQ_v}{dt} = \frac{dQ_R}{dt} + \frac{dQ_L}{dt}, \quad (5.29)$$

being observed. Q_R and Q_L respectively denote the volume flow rates of MR fluid through the right and left valve half. This permits calculation of the volume flow rates through each valve half as a function of the variable valve half resistances by setting equations (5.22) and (5.25) equal and solving (5.28) and (5.29) for Q_R and $\frac{dQ_R}{dt}$. The resulting flow divider equation is

$$(R_r + R_{op} + R_L)Q_R + (I_R + I_L)\frac{dQ_R}{dt} = (R_R + R_{op})Q_v + I_R\frac{dQ_v}{dt}. \quad (5.30)$$

The fluid leakage Q_{leak} across each valve half is a function of the variable valve half resistances, which are dependent on valve position y , flow direction, input voltages V_L and V_R , and the divided volume flow rates. The experimental values obtained from Sect. 4.3.2 are implemented in a look-up table within the simulation to account for the leakage output based on resistance and pressure differential inputs. In previous measurements, it was observed that the left valve had significantly more control over the valve position than the right half. Therefore, in this model the position of the valve is calculated from the leakage past the left valve $Q_{L,leak}$. From the flow divider equation, Q_L is known. As shown by the

following sequence of equations,

$$Q_{L,leak} = \frac{p_4 - p_3}{R_L}, \quad (5.31)$$

$$V_L = \int (Q_L - Q_{L,Leak}) dt, \quad (5.32)$$

$$y = -\frac{V_L}{A_v}, \quad (5.33)$$

a simple subtraction permits calculation of the fluid volume storage rate within the left valve. This is integrated and divided by the cross-sectional valve fluid area to determine y . The physical travel limitation of the movable valve shaft due to the rigid valve housing is enforced through a look-up table for the variable valve half resistance. Infinite resistance is generated by the look-up table when the position reaches a position limit (0.20 or -0.20in) and the flow direction is pushing the valve closed. When the flow reverses to push the valve open, the resistance returns to measured values.

The position of the output piston z is modeled by integration of the volume flow rate through the right valve half,

$$V_R = \int Q_R, \quad (5.34)$$

$$z = \frac{V_R}{A_{op}}, \quad (5.35)$$

where A_{op} is the output piston cross sectional area. Similar to the valve location equations, equation (5.35) effectively projects the output piston position based on stored fluid volume.

The actuation force F_z is the difference in pressure forces on each side of the piston,

$$F_z = \frac{p_4 - p_5}{A_{op}}. \quad (5.36)$$

The equations of this model were assembled in a Matlab-Simulink block diagram program for numerical solving. Additional details of the program and corresponding run script can be found in Appendix B.3.2.

5.2.2 Model #2 Results

Running system-level model #2 with the actuator control strategy outlined in Sect. 4.2.4 produces the result set shown in Fig. 5.6. The solenoid control strategy alternated between left “on” and left “off” to coordinate with the appropriate fluid flow direction as shown in Figs. 5.6(a) and (b). It is noted that the right valve half remained “off” for the entire run. The input acceleration and force are sinusoids and the input solenoid voltage is a square wave. This is similar to the automated experimental inputs produced by the universal compression-tension machine and the LabVIEW control program.

Fig. 5.6(c) shows the output valve oscillating about the left closed position. This result was observed experimentally as shown in Fig. 4.7(c). It is noted that numerical values for valve position extend beyond the intended range limits of ± 0.20 . This is attributed to the stored volume technique for calculating valve position using only one valve half. For a future generation of this model, use of both valve halves to model valve position should be investigated.

The modeled actuation is shown in Fig. 5.6(d). The waveform is a ramped sinusoid, similar to the experimental result shown in Fig. 4.7(d). One major difference is the increased rate of actuation. Experimental results were near 0.325 in/s, while the model produces rates of approximately 1.7 in/s. This difference is attributed to the lack of fluid resistance and capacitance effects within the system. The addition of such fluid power loss terms would reduce the actuation rate. However, this also suggests that minimizing friction and capacitance in the valve will increase the output actuation.

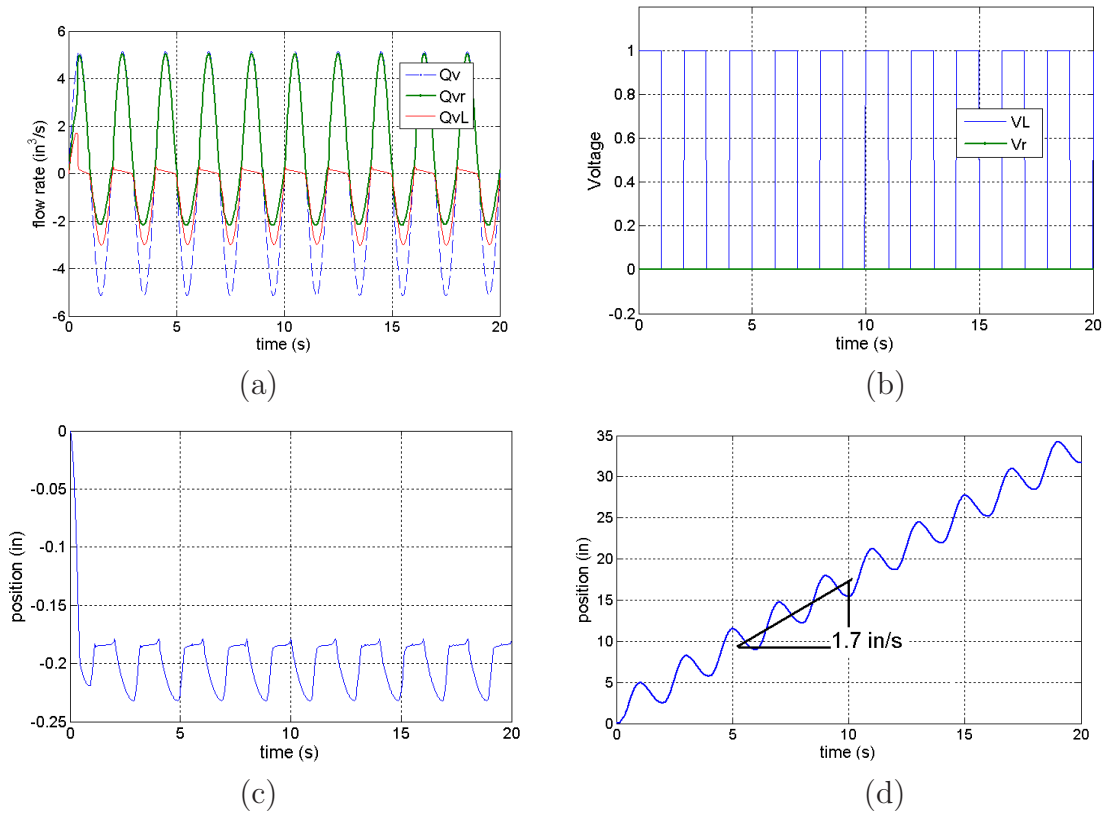


Figure 5.6: System-level model #2 results for (a) valve position, (b) input voltages (solenoid “on”/“off”), (c) volume flow rate, and (d) output valve position.

CHAPTER 6

CONCLUDING REMARKS

6.1 Summary of Findings

In this research, a new hybrid actuator was conceptualized, constructed, characterized, and modeled. The experimental work varied from individual component testing to system testing with automated controls. Concurrent with testing, a system-level model of the actuator was constructed.

The first experimental setup comprised of a large double-sided magnetorheological (MR) fluid valve with no output piston. By manually controlling all inputs, we showed that the combination of pressure differential and changing MR fluid viscosity could control fluid flow through the valve. Furthermore, absence of either input led to the inability of producing cyclic closure of the MR fluid valve. A system-level model was developed which verified the cyclic closure of the MR fluid valve with the combination of appropriate inputs.

Testing progressed to automated inputs and the addition of an output piston to perform actuation. Through use of a universal compression-tension machine and a LabVIEW controller, over 6 in of positive actuation was achieved at a rate of 0.325 in/s from a sinusoidal hydraulic input. This was achieved using the resonant operating frequency tested to be near 0.50 Hz and the control strategy found from waveform testing which activates only the left valve half's solenoid. A second iteration of the system-level model was developed using a stored fluid volume approach to control the position of the MR fluid valve. The

model results confirmed the ramped-sinusoid actuation waveform, but with an improved actuation rate of 1.7 in/s.

Resistance values of the MR fluid valves were quantified as a function of various independent inputs. MR fluid valve #1 produced a minimum and maximum resistance of 10 and 100 lbf·s/in⁵, respectively. This accounts for an effective variable resistance factor of 10. MR fluid valve #2 was 570 % smaller than MR fluid valve #1 and produced a minimum and maximum resistance of 10 and 174 lbf·s/in⁵, respectively. This accounts for an effective variable resistance factor of 17. Larger maximum resistances near 225 lbf·s/in⁵ were projected to occur with saturating input magnetic fields. MR fluid valve #2 enhanced the performance of MR fluid valve #1 by 70–125 %.

A unidirectional Terfenol-D fluid pump was developed and tested as an intermediate step to the reciprocating flow pump. The pump operated best with an average bias pressure of 40 psi. The maximum flow rate was 0.25 in³/s with a pump input of 8.5 V-rms at 50 Hz. The maximum blocking pressure was approximately 75 psi with a pump input of 8.5 V-rms at 30 Hz.

6.2 Future Work

The work presented in this thesis advanced the understanding of our compact, fly-by-wire, hybrid actuator concept, which is potentially capable of producing large deflections and large forces. The next research step should combine the unidirectional Terfenol-D pump and MR fluid valve #2 to create a hybrid, fly-by-wire actuator. Testing should incorporate control strategies which maximize the output actuation rate and blocking force.

Pending successful actuation using the unidirectional Terfenol-D pump, MR fluid valve #2 should be redesigned and miniaturized to permit coupling with a reciprocating flow Terfenol-D pump. A necessity for miniaturization is the sacrifice of experimental adjustability. An MR fluid valve should be designed which eliminates the coupling of two separate

halves. This will produce a significantly more compact design and aid in the reduction of the parasitic sliding friction and inertia effects.

Once a sufficiently small fluid valve has been constructed and the variable resistance factor is maximized, a reciprocating flow Terfenol-D pump should be developed. The passive ball-cone check valves of the unidirectional device are incapable of operation at the optimal frequency. The benefit of the reciprocating flow pump is that no passive check valves are needed. Instead, the MR fluid valve will rectify the flow.

Finally, the system of actuator components should be merged into a single, self-contained unit.

APPENDIX A

ACTUATOR COMPONENT DESIGN DETAILS

A.1 MR Fluid Valve Design #1

Additional details of the first magnetorheological fluid valve design are discussed in this section. It is emphasized that this design was the primary work of Brett Burton, an undergraduate student researcher who developed and tested an early valve design. The assembly draft of one half of the fluid valve is shown in Fig A.1. Two identical fluid valve halves are coupled by the movable rod to produce the double-sided valve. The three piece housing subassembly is shown in Fig. A.2. The two components which are press fit and welded together are shown in Figs. A.3 and A.4. The removable housing piece shown in Fig. A.5 is attached to the main housing through four bolts. Within the housing is the movable valve piece subassembly which is shown in Fig. A.6. This component includes a steel “conical” end piece and an aluminum connecting rod as shown in Figs. A.7 and A.8, respectively.

A solenoid was wrapped around each movable end piece to produce the magnetic field necessary to activate the MR fluid. To prevent electrical shorts across the steel end piece, general-purpose winding varnish was applied to the metal surfaces to be in contact with the wire. The wire used is enamel-coated AWG 26 magnet wire. Each solenoid has 20 rows with approximately 15 turns per row. To protect the solenoid, epoxy was used to seal all exposed wires. After the solenoids were wound, the rod was screwed to the movable end

piece. Loctite was used to assure permanent attachment. Once attached, the lead wires were routed through the center of the shaft and sealed with epoxy. This completes the movable piece subassembly.

The removable housing end cap has a bronze sleeve bushing press-fit to support the movable piece subassembly. To assure a proper sliding fit, the bearing was machined to the proper inner diameter after being press-fit. A spring type oil seal (CR-Chicago Rawhide, type 8624) was press-fit into the part after the bushing fabrication has been completed. An O-ring (Parker size 2-219) was placed in the machined gland to seal housing pieces.

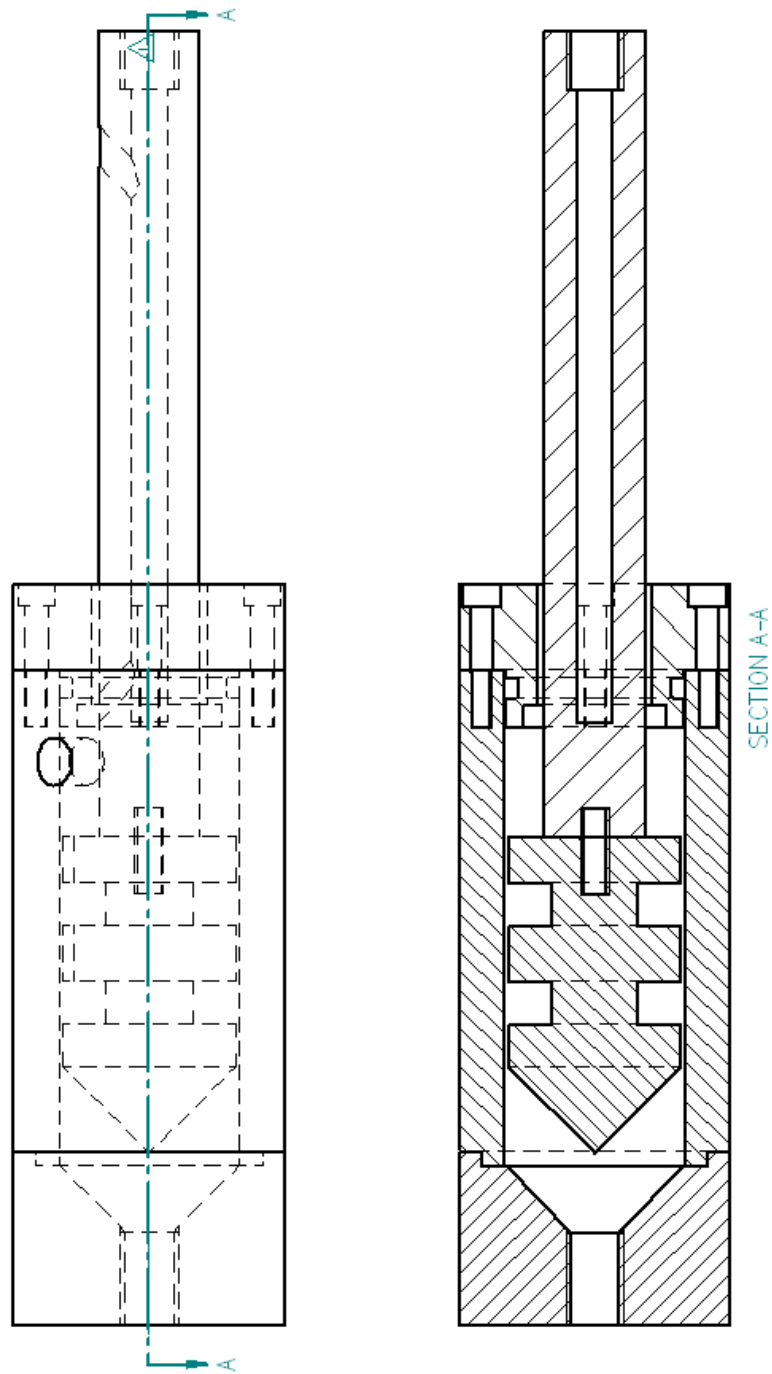


Figure A.1: Magnetorheological fluid valve design #1, Main assembly. An identical half is coupled to complete the double sided valve.

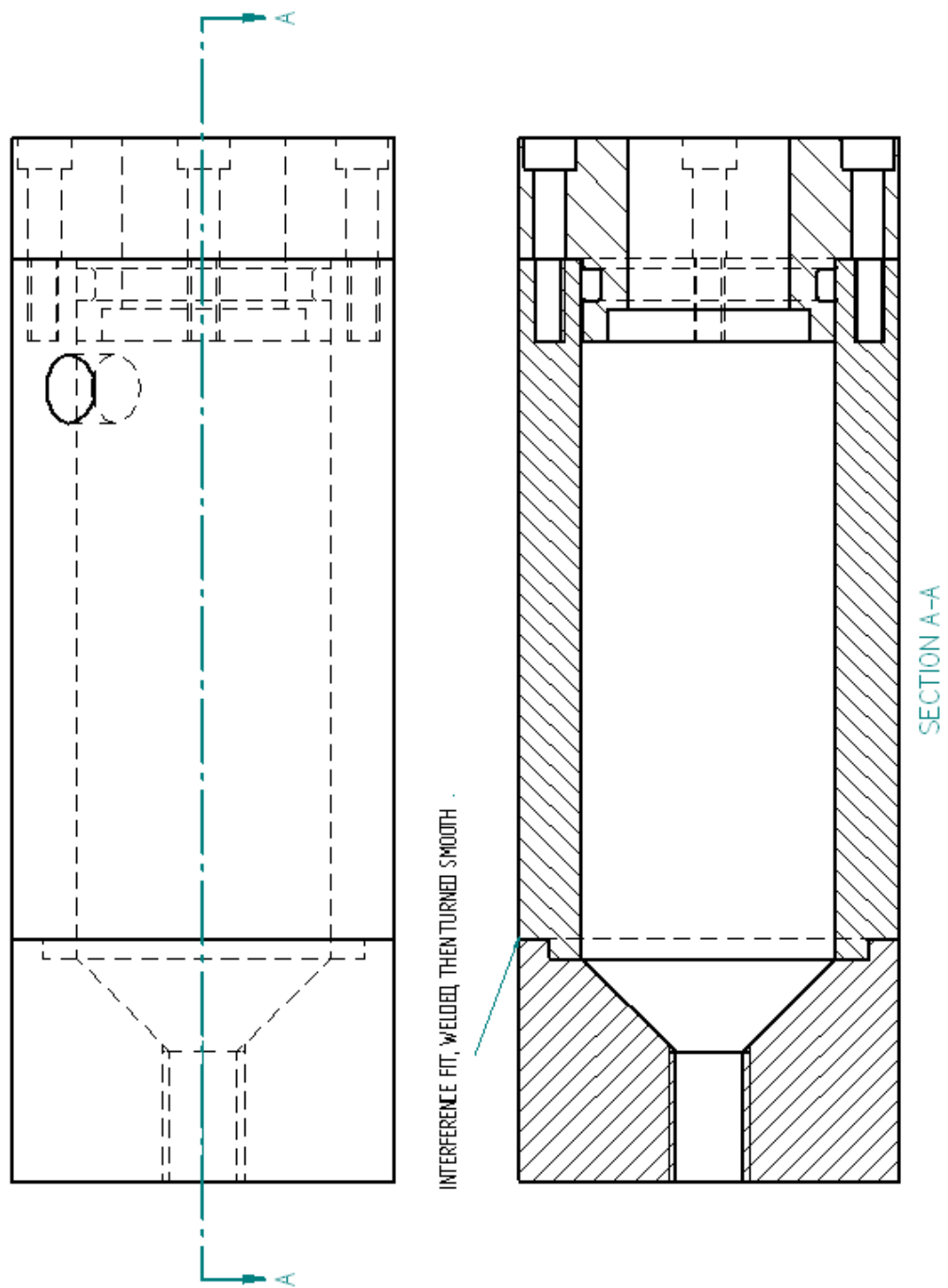


Figure A.2: Valve housing subassembly.

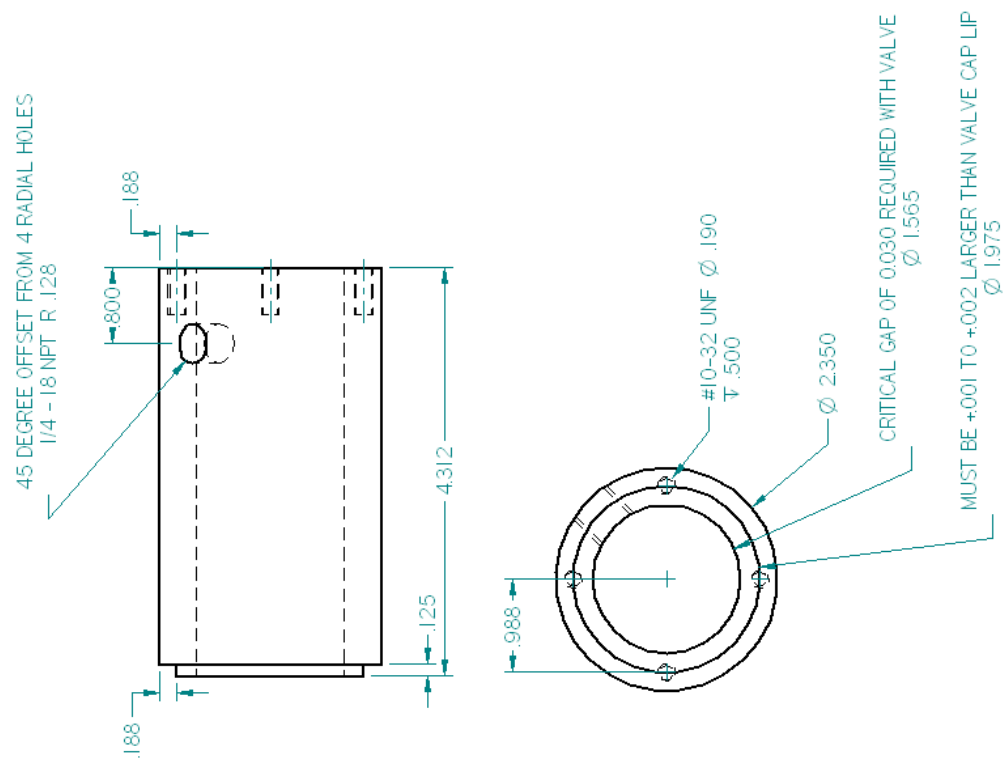


Figure A.3: Main housing piece (steel)

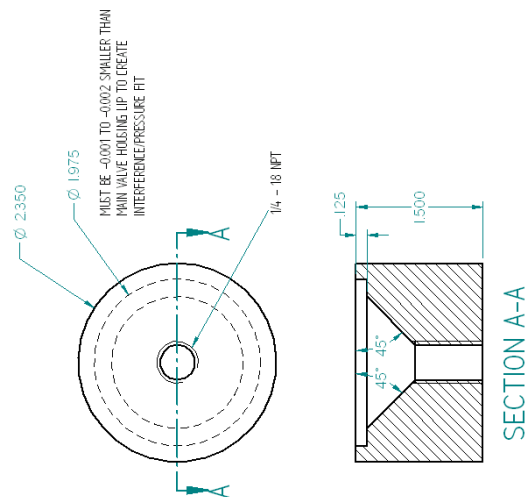


Figure A.4: Main housing piece (steel), press fit and welded to previous housing piece.

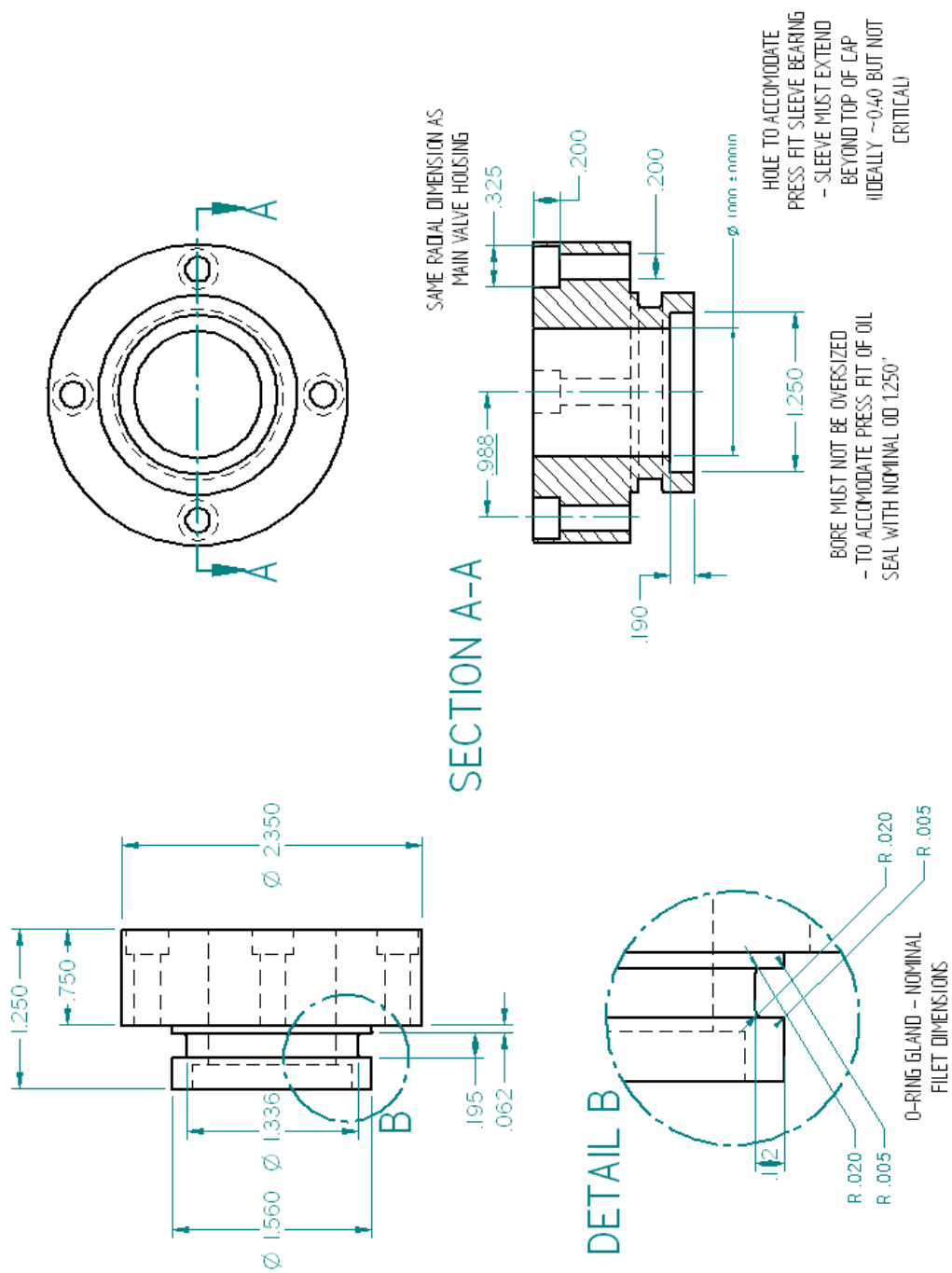


Figure A.5: Removable housing end cap (steel).

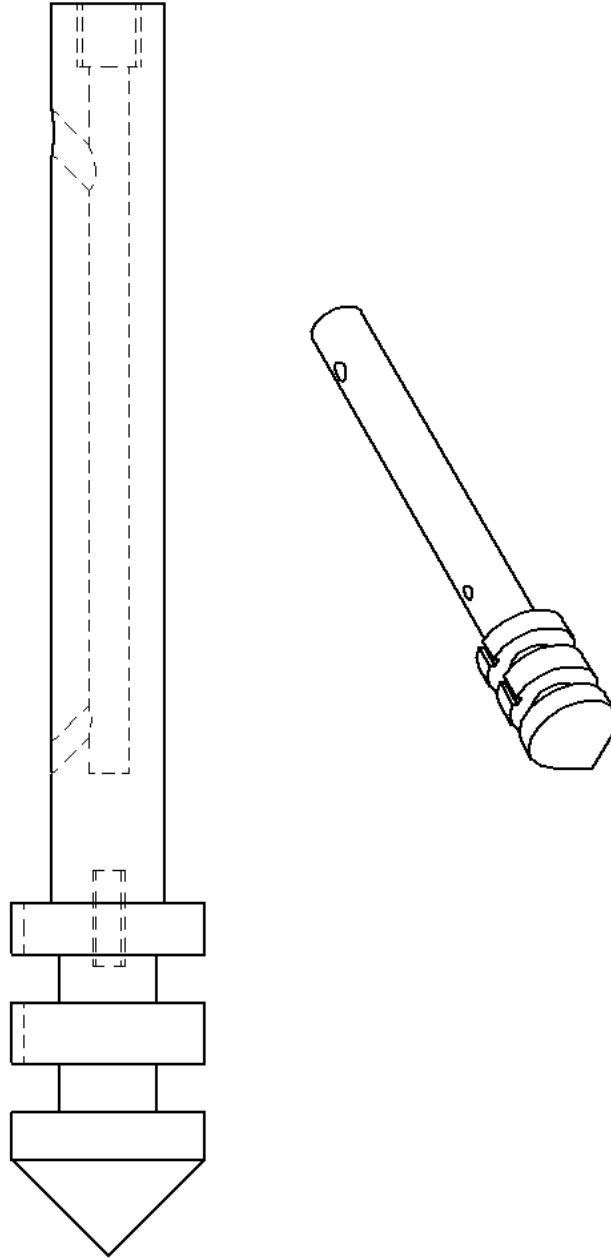


Figure A.6: Movabable valve piece subassembly.

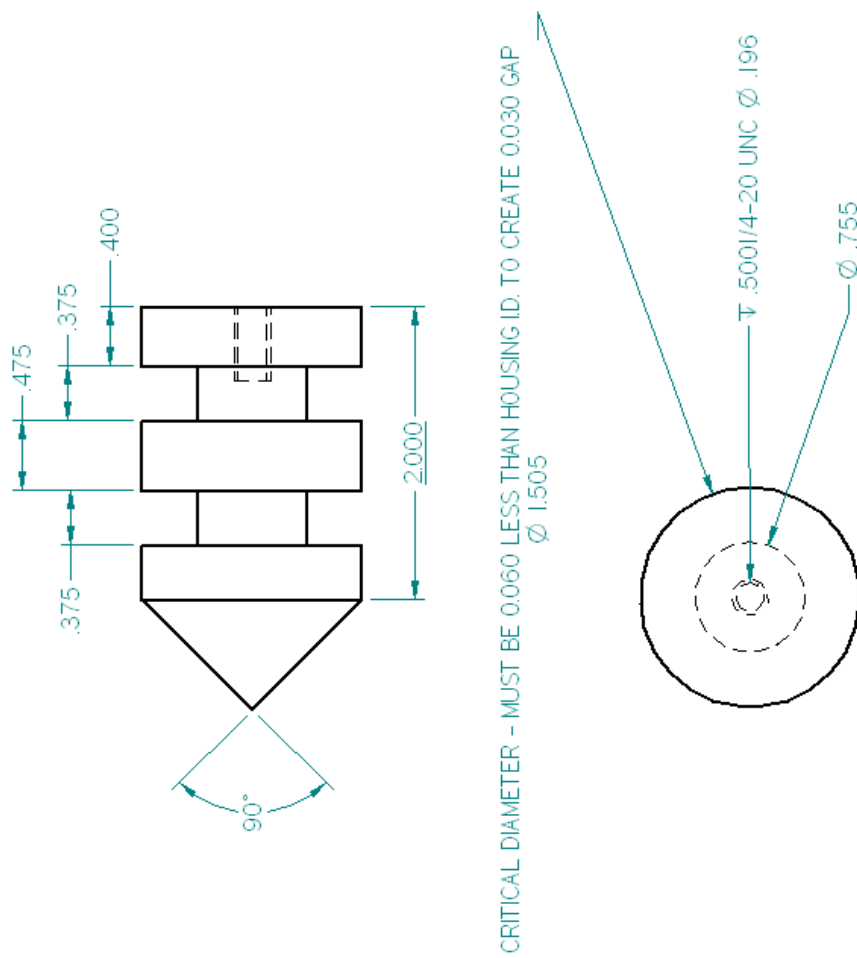


Figure A.7: Movable valve head piece (steel)

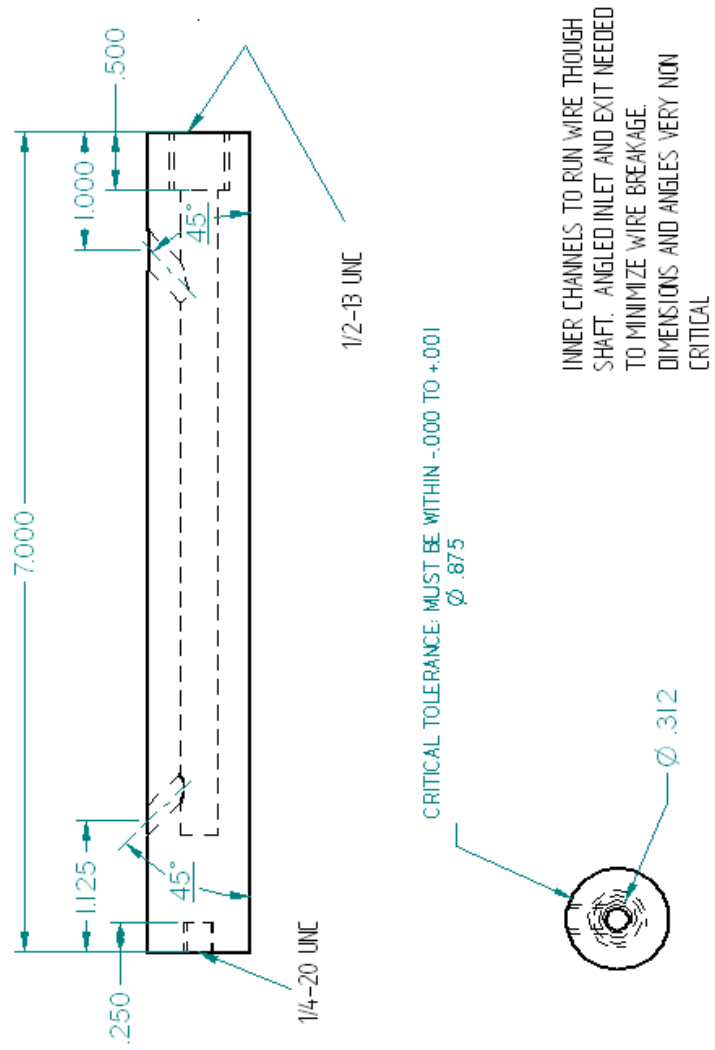


Figure A.8: Movable valve rod piece (aluminum). Connected to head piece through set screw.

A.2 MR Fluid Valve Design #2

Additional details of the second MR fluid valve design are discussed in this section. The complete assembly, along with a cutaway view are shown in Fig. A.10. The goal of this valve design was to significantly reduce the size in comparison to design #1. By locating the coils outside of the movable valve piece, a smaller movable valve piece could be used. How small it could be was limited by the size of the surrounding solenoids which had to be manually wound. A nominal solenoid stack size of 1 in length, 0.50 in inner diameter, and 1.00 in outer diameter was selected. Upon designing, it was observed that a steel solenoid stack sleeve shown in Fig. A.15 would facilitate the axial alignment and insertion into the housing. Therefore, the coil outer diameter was decreased to approximately 0.80 in. As shown in Fig. A.9, the stack consists of four individual solenoids wound around thin aluminum sleeves, each separated by steel spacer (1/16 in thickness) to direct the magnetic flux perpendicular to the gap. This yields an individual coil thickness of approximately 0.20 in. It is noted that one coil end has no spacer. This is accounted for in the final assembly using the steel housing end cap shown in Fig. A.12 to direct the flux. The solenoids were wound sequentially along the same spool. To facilitate removal, a thin plastic film was placed on the spool end pieces. The wire used was enamel-coated AWG 26 magnet wire. Each solenoid has 10 rows with approximately 8 turns per row. To increase the solenoid resistance, the four solenoids were wrapped using only two sets of lead wires. The right most coil was wound first in a clockwise direction. Using the same wire, the winding was reversed to counter-clockwise for winding of the adjacent coil. Upon completion of the coil pair, the lead wires were taped out of the way. The second pair was wound using a similar technique. After all four solenoids were wound, epoxy was used to protect and insulate the exposed wire. The completed solenoids were later slid into a steel outer sleeve and further sealed with epoxy.

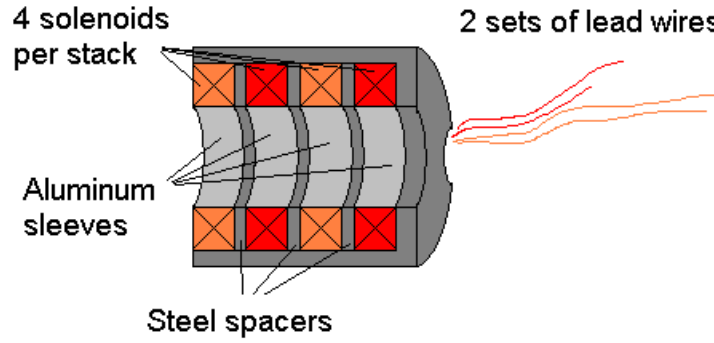


Figure A.9: Schematic of solenoid stack assembly

The main housing piece shown in Fig. A.11 has a press-fit sleeve bushing and spring type oil seal (CR-Chicago Rawhide, type 2514), similar to that in design #1, but with a reduced size. The solenoid stack sleeve was carefully inserted into the main housing piece, which has a lip to hold the sleeve in place. A small cutout in the housing permits the lead wires to be routed out of the housing, and then sealed with more epoxy. The epoxy was applied in two steps. First, thick epoxy with the consistency of clay sealed the hole from the outside. Second, to assure a leak-proof seal, low viscosity epoxy was poured into the housing through the fluid port hole.

The movable valve piece dimensions were tailored to fit the housing and solenoids. To maintain a 0.030 in gap, a diameter of 0.440 in was assigned to the conical head piece. The rod size of 0.25 in was a nominal dimension based on spring seal availability.

To complete the assembly of the valve, the housing end cap shown in Fig. A.10 is fitted with two O-rings. One (Parker size 2-210) is used as a perimeter seal between the two housing pieces and one (Parker size 2-114) is used as a face seal between the housing end cap and solenoid stack. The end cap is inserted into the main housing until the lip on the end cap was flush with the main housing. Using the lip, the end cap was rotated to align the four radially oriented bolts.

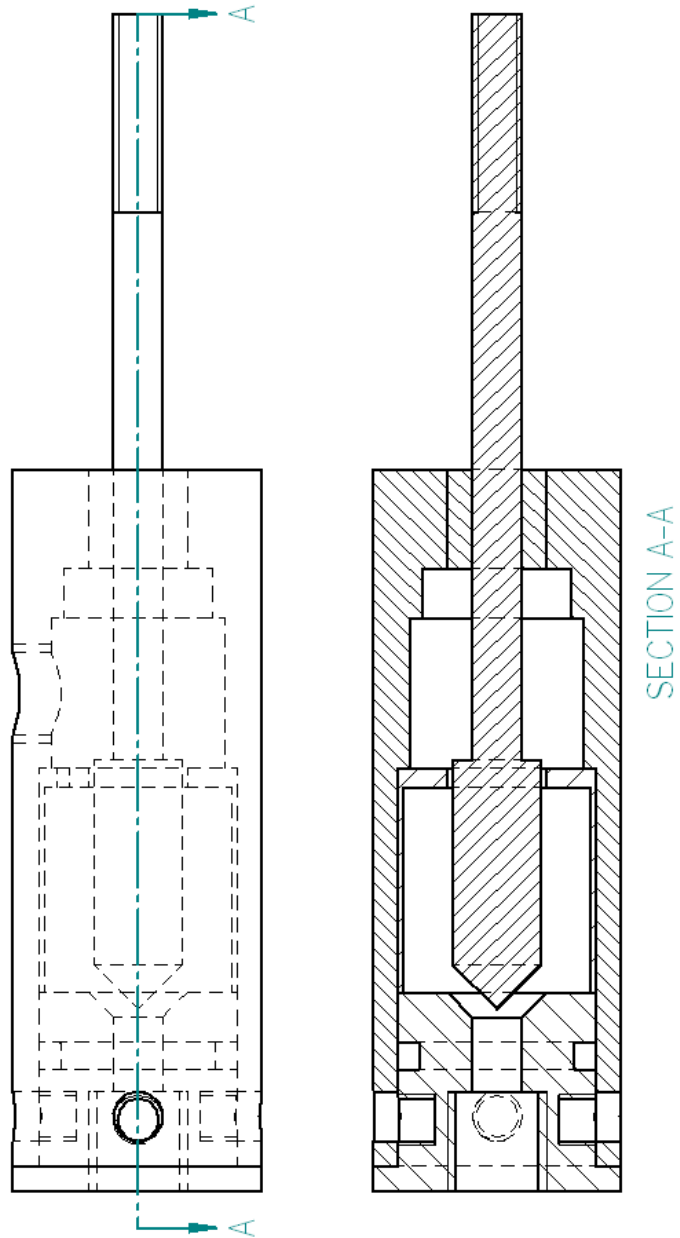


Figure A.10: Assembly of entire fluid valve (design #2)

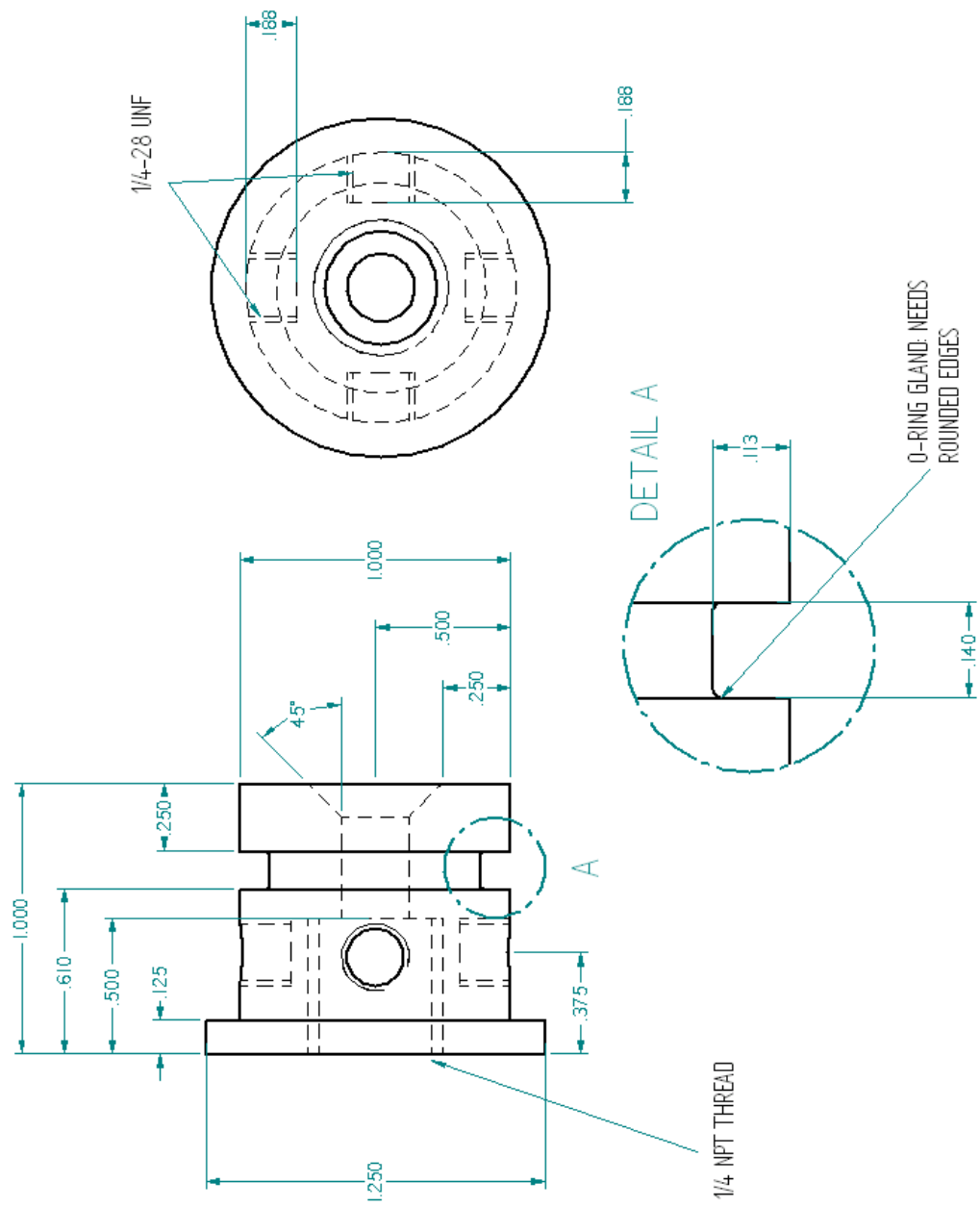


Figure A.12: Housing end cap (steel)

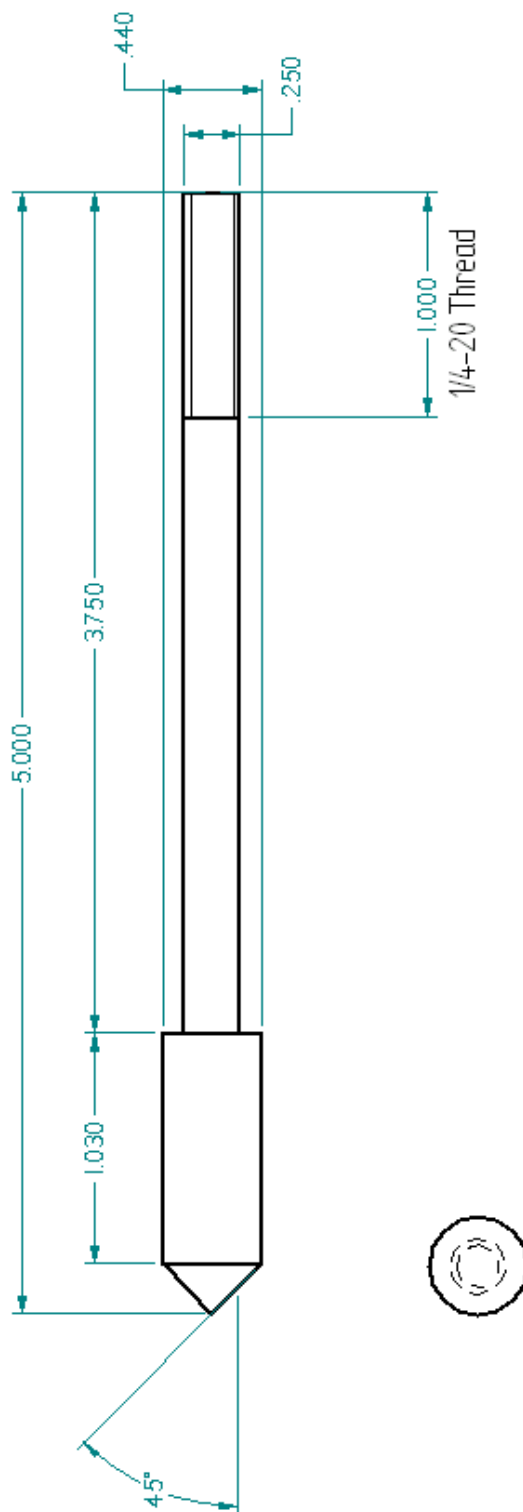


Figure A.13: Rod (steel)

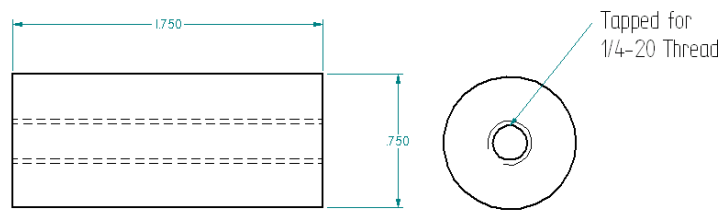


Figure A.14: Coupling piece (steel)

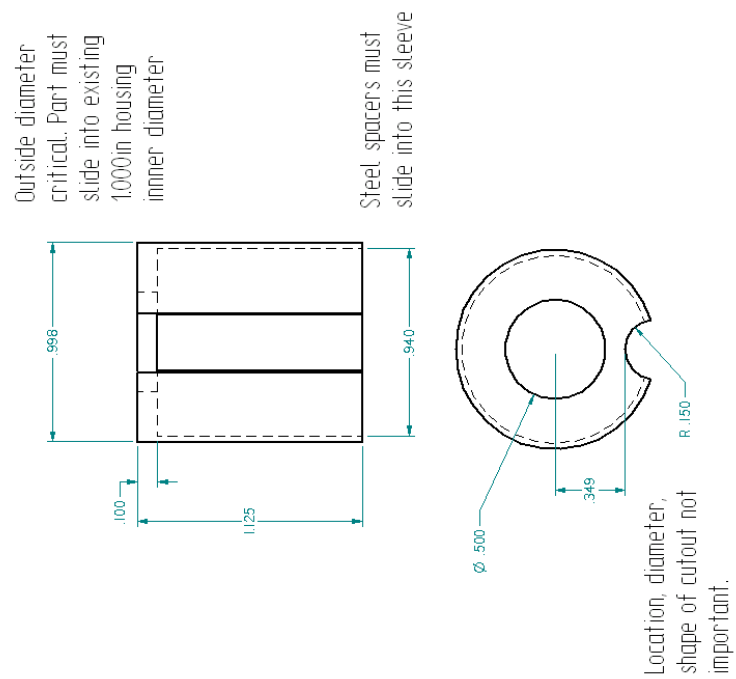


Figure A.15: Solenoid stack sleeve (steel). The semi-circular cutout leaves space for the lead wires to be routed out of housing.

A.3 Unidirectional Terfenol-D Fluid Pump Design

This section includes additional details of the unidirectional Terfenol-D fluid pump design shown in Fig. A.16. The main component is a AA090 ETREMA Terfenol-D transducer. The Terfenol-D rod is 0.5 in in diameter and 4 in in length. The surrounding coil has 735 turns of 21 gauge wire. The dc resistance is approximately 1.7Ω , and increases with input frequency. Due to the large variance in system impedance, the ac current limit for continuous operation is 3.4 A-rms. The output displacement is approximately ± 45 micrometers at dc. The blocked force is approximately 375 lbs and maximum dynamic force to remain in Terfenol-D compression is approximately 200 lbs. It is noted again that Terfenol-D is stronger in compression than in tension, therefore it is generally pre-loaded to operate at various degrees of compression. Previously presented swept sine tests place the transducer resonance near 2660 Hz.

The transducer was fitted with an aluminum piston piece shown in Fig. A.19 to push fluid within a steel fluid chamber shown in Fig. A.18. The fluid chamber outside diameter was set equal to the transducer outside diameter to facilitate relative positioning. The fluid chamber seal is an O-ring (Parker size 2-219) using the dynamic seal specifications outlined by the manufacturer. Ball and cone type flow direction check valves were implemented for the initial design. The inherent problem with passive valves is the relatively low bandwidth of approximately 100 Hz compared to the 2660 Hz resonance of the transducer. The check valves were obtained from Lee Company. One forward flow (CCFM1550200S) and one reverse flow (CCRM1550200S) check valve with no spring were press fit into the chamber. It is noted that directional flow check valves of this type can also be spring loaded which would require a pressure differential to be sufficiently large before opening. Without knowing the pressure that could be produced by the pump during the design phase, no spring was used in this iteration.

To aid in final assembly, an alignment block shown in Fig. A.17 was constructed. The block has a cutout to hold the transducer in one fixed position. Threaded holes are present to clamp the transducer to the block. The fluid chamber slot fixes the axial alignment with the transducer, while permitting adjustability in the fluid chamber size. The chamber is held in a fixed location through an aluminum spacer (1 in) between the alignment blocks dividing wall and a threaded rod which compresses and locks the chamber against the block. For all testing in this thesis, the piston was nominally 0.15 in from contact with the fluid chamber, which yields a fluid volume of 0.30 in³ within the chamber.

After initial assembly, a noticeable amount of magnetic leakage from the transducer bias magnets was observed on the fluid chamber. To remove this undesired effect, a better material selection would have a significantly lower magnetic permittivity (i.e. stainless steel, aluminum).

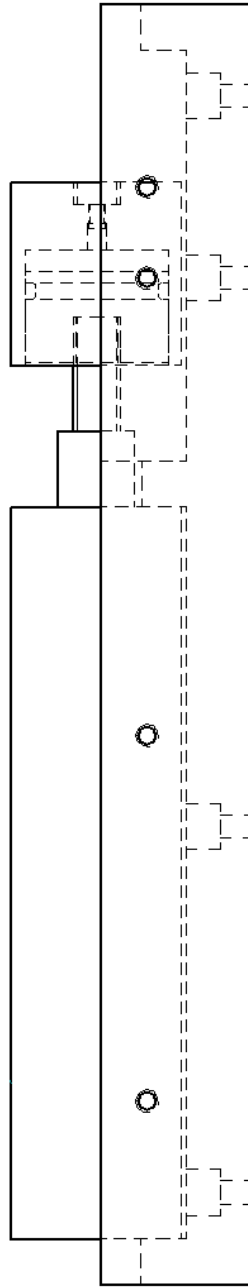


Figure A.16: Assembly of unidirectional Terfenol-D fluid pump

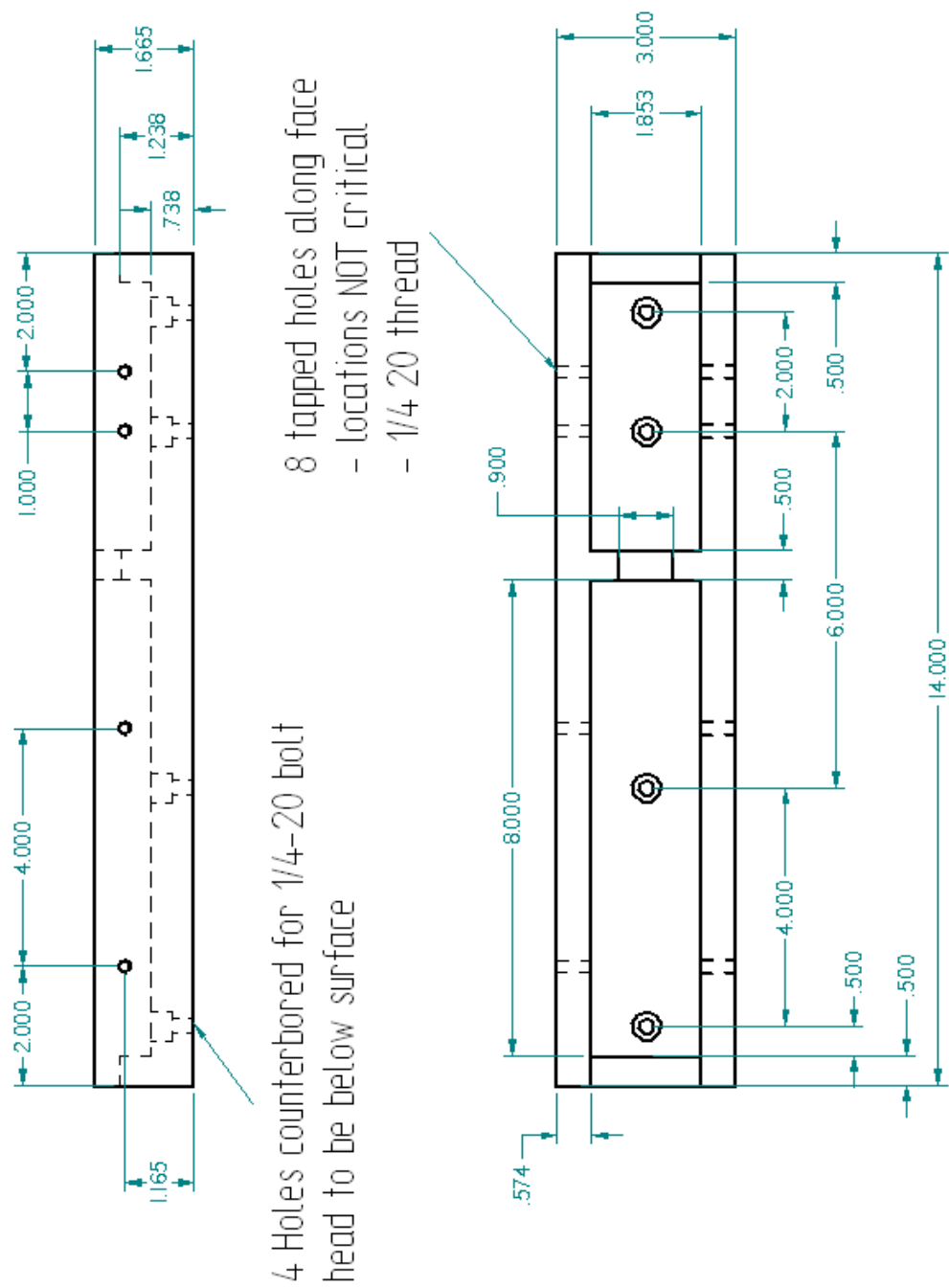


Figure A.17: Alignment block (aluminum). Used to rigidly hold Terfenol-D transducer and fluid chamber at a fixed spacing and inline.

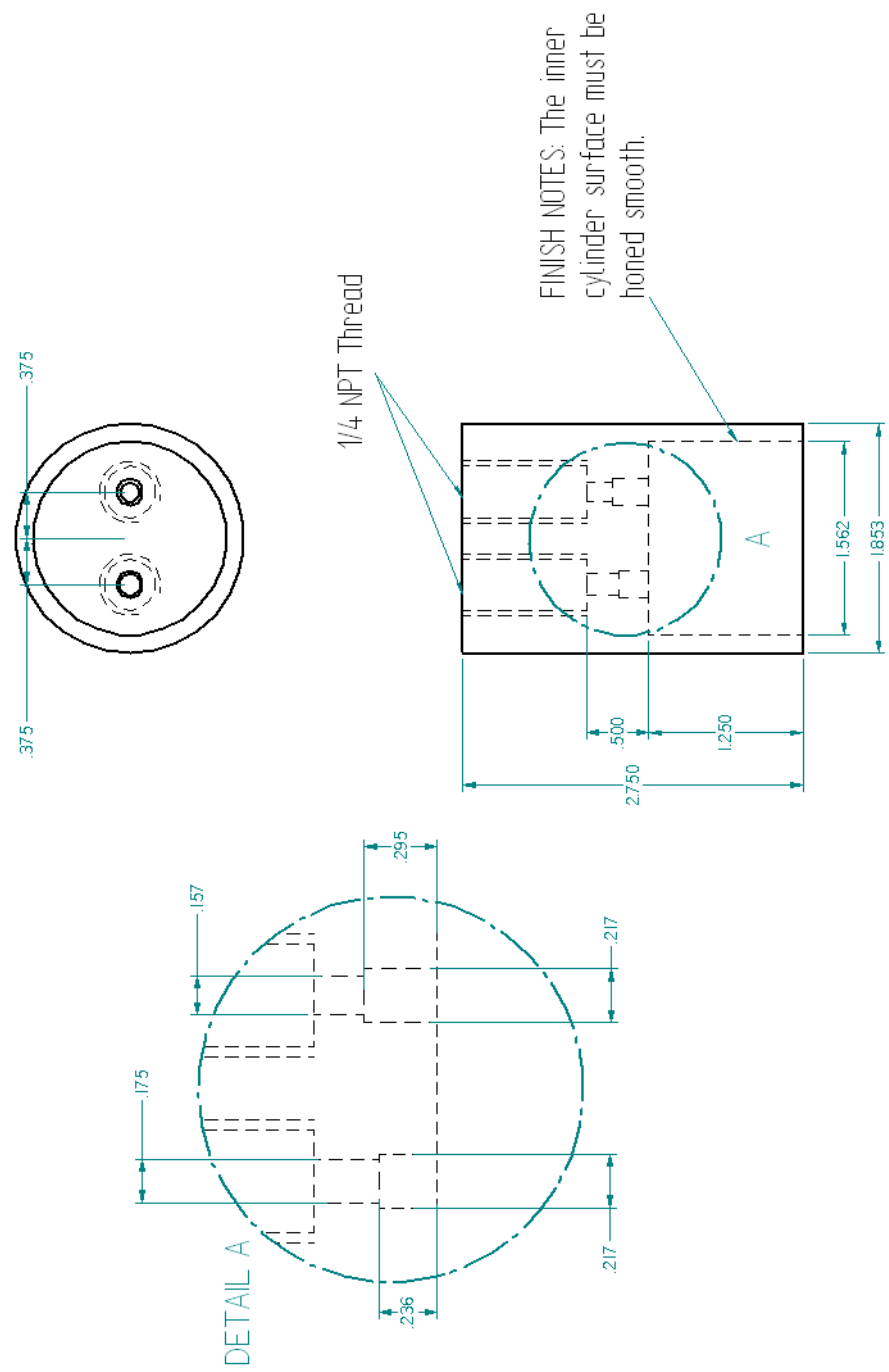


Figure A.18: Fluid chamber (steel). Detail-A shows the dimensions for the press-fit fluid check valves (Lee Co: CCRM1550200S and CCFM1550200S)

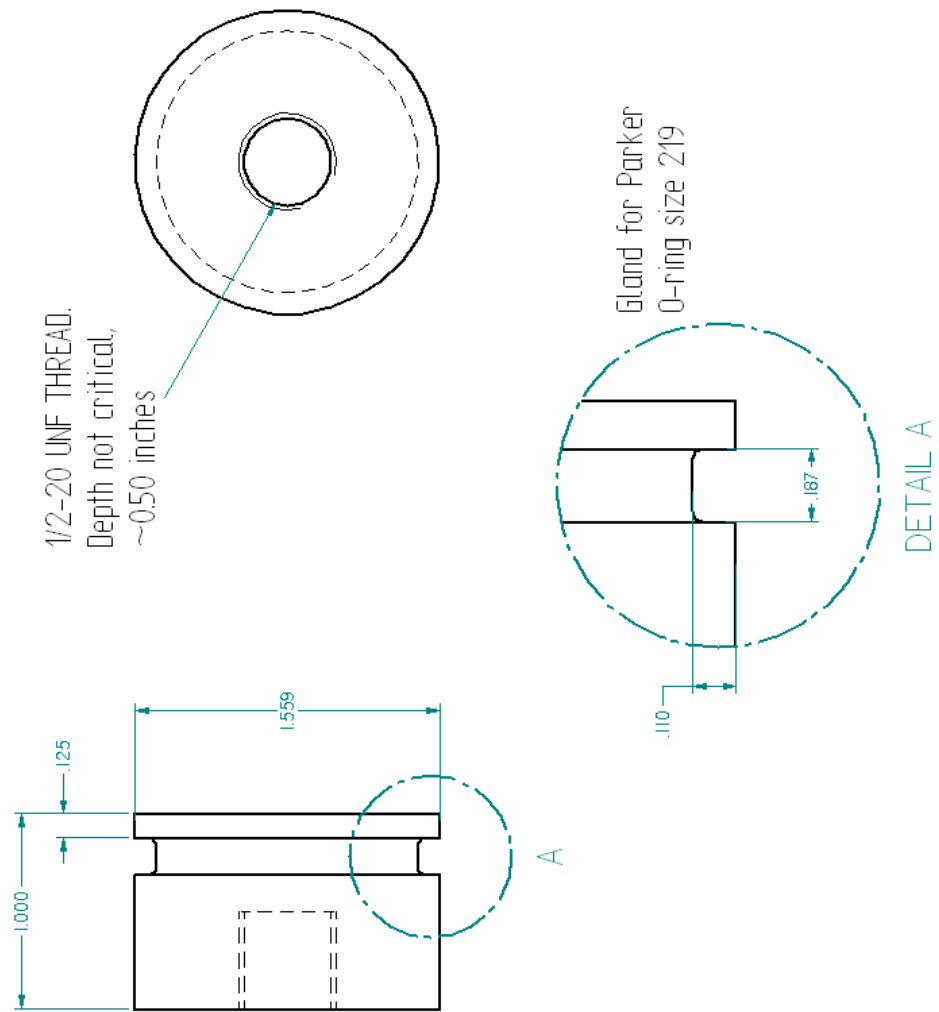


Figure A.19: Piston (aluminum)

APPENDIX B

PROGRAM DETAILS

B.1 Labview

B.1.1 MTS and Solenoid Controlled Actuation Program

LabVIEW (version 6i) is a programmable user interface that can be used in data acquisition (DAQ) and control applications. For the purpose of this research, it was used to simultaneously collect data from two separate DAQ systems, compile results into a single file for later post-processing, and control the timing of the valve solenoids. In order for LabVIEW to accomplish this task, the program shown in Fig. B.1 was developed along with the associated user display interface (panel) shown in Fig. B.2.

The outline of the program is as follows. Identification numbers are assigned to direct the program to the two DAQ cards. One points to a National Instruments card connected to the universal compression-tension machine's load cell and position transducer (q134,1,0), the other to a USB-based Measurements Computing Corporation (MCC) Personal Measurement Device (PMD-1208FS) card which has 4 differential inputs and 2 analog outputs. Each input signal is routed to a sampling block, which records the current value to a single valued array. Each single valued array is merged into a new array containing data from each input channel. The merged array is divided to plot real-time graphs of the recorded signals in the display panel. The current load cell value is converted to engineering units (lbf) and run through output control blocks. A constant bias force of approximately 28 lbf

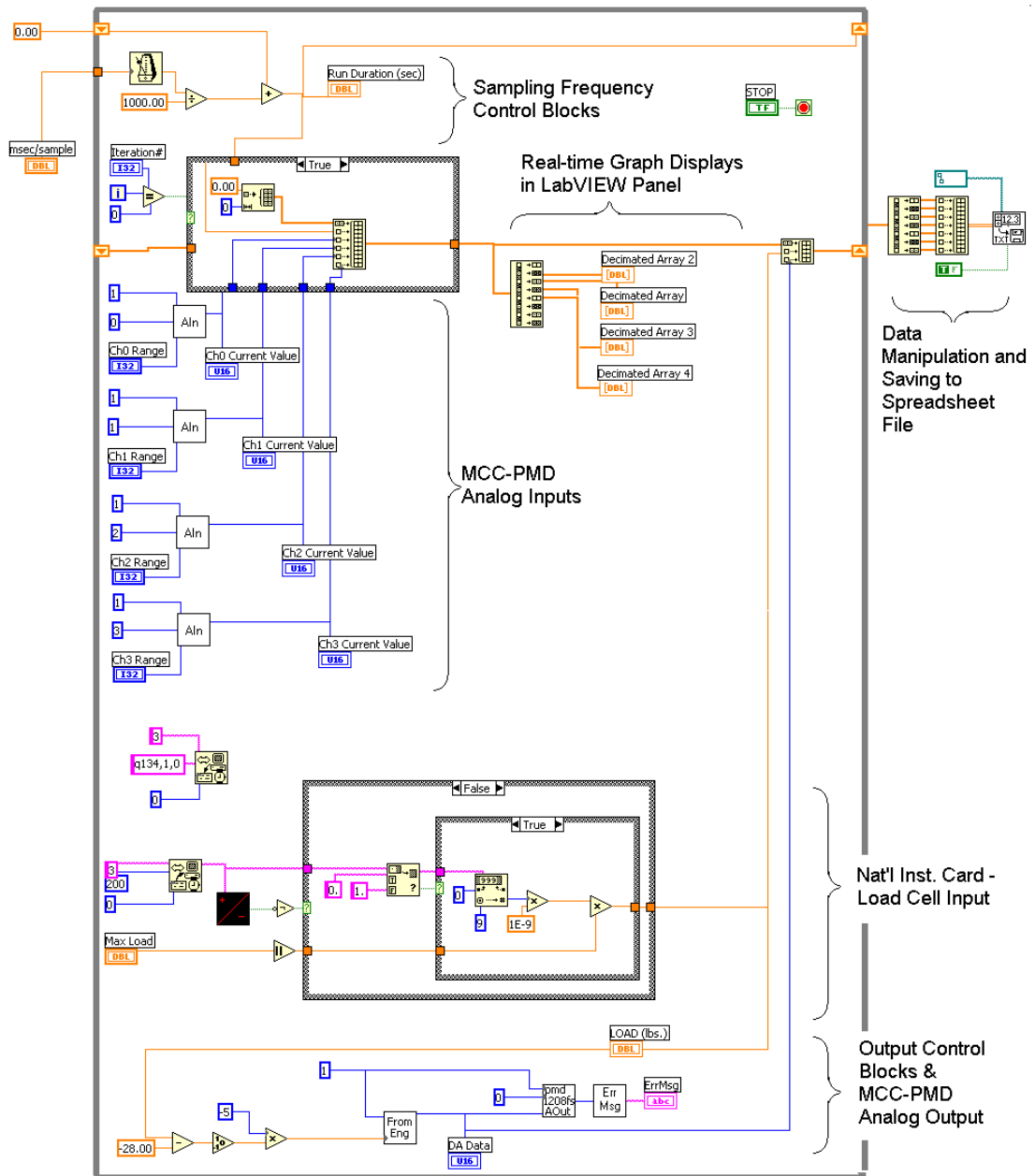


Figure B.1: Screen capture of LabVIEW program developed and used for controlled actuation of the MR fluid valve's solenoids.

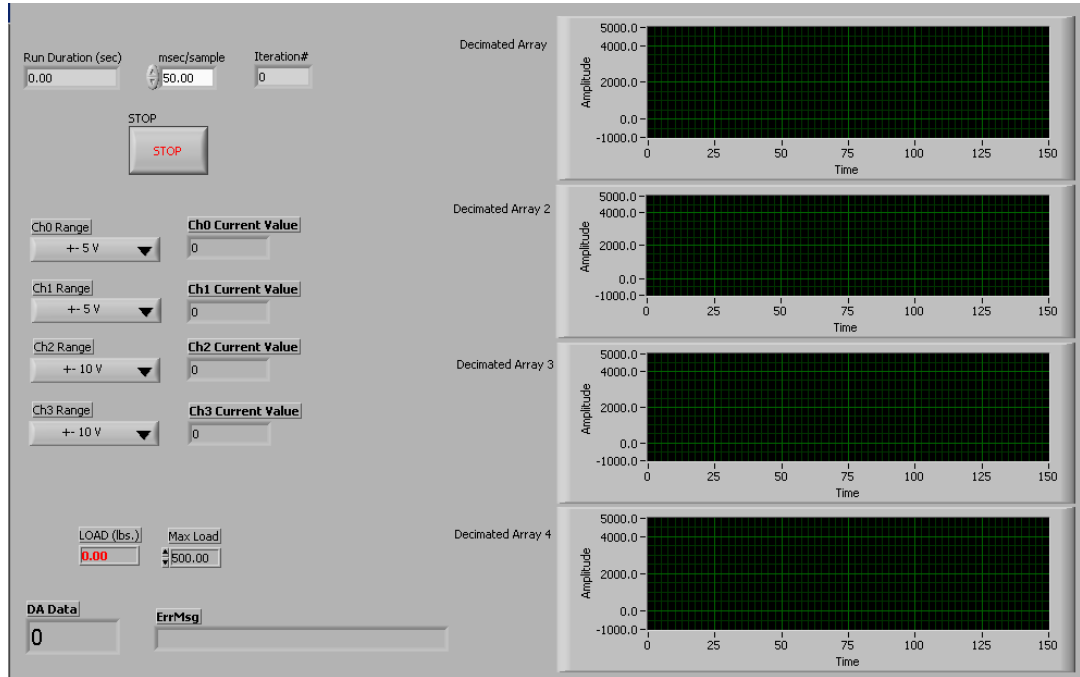


Figure B.2: Screen capture of LabVIEW interface panel that accompanies the controlled actuation program.

was observed in the system, which was removed by a subtraction block. The sign of the force was then taken, and multiplied by -5. When converted back to a 12-bit signal (From Eng), this effectively produces an output number of 4095 for a negative load and 0 for a positive load. The PMD analog output block, sends a 0 mV and 4095 mV output signal for the 0 and 4095 values, respectively.

This completes the first iteration of the program, and the running while-loop returns to the beginning. Based on a user-defined time delay, the sampling frequency can be easily adjusted. After the time delay has expired, a new set of data points are collected and merged to the previous data samples. This loop continues to run until the manual stop button is clicked. The program then takes the recorded data array, reorganizes the data into a 2-D array, and saves it to a file that can be opened in a spreadsheet. It is noted

that this program was aided from pieces of existing programs and the assistance of Steve Martisauskas.

From trial and error, it was observed that simultaneous measurements of the universal compression-tension machine's load and position slowed the LabVIEW program to an unusable level (less than 1Hz sampling rate). The cause of this performance drop is unknown. This limits the use of the program to a recording of four inputs through the PMD and either the load or position.

B.1.2 Variable Resistance Measurement Program

For fluid valve resistance measurements, an alteration of the controlled actuation program was developed as shown in Figs. B.3(a) and (b). For this experiment, only two input pressure sensor signals needed to be acquired through the MCC-PMD. Therefore, two analog input blocks were removed from the previously presented program. To complete the data set for resistance calculations, the MR fluid volume flow rate through the valve was needed. The input piston force recording from the previous program was replaced with the MTS input (hydraulic cylinder) position. This data set was converted into engineering units (inches) before being merged with compiled data array.

B.1.3 Terfenol-D Pump Controlled Actuation Program

Another variation of the LabVIEW program was developed for use in controlled actuation experiments which incorporate the unidirectional Terfenol-D transducer for input MR volume flow rate and pressure. The program is shown in Fig. B.4. For these runs, there are no MTS load or position waveforms to be acquired. The above programs must be modified to produce a control signal completely independent of the four input signals. This is accomplished by the generation of a square waveform array before entering the continuous while-loop. Each loop iteration reads the corresponding iteration index number from the square waveform array. In other words, the first loop reads the first waveform array

value and the n^{th} loop iteration reads the n^{th} waveform array value. This effectively mates the independent input and output functions into a single program. The square waveform must be constructed properly to match the while-loop sampling frequency. The number of data values per cycle should correspond to the sampling frequency. For a 0.50 Hz square waveform input and a 0.025 msec/sample sampling rate, each square wave cycle should consist of 80 values.

$$\frac{1sample}{0.025sec} \times \frac{2sec}{1sqr.cycle} = \frac{80samples}{1sqr.cycle}. \quad (B.1)$$

There are three output square waves for this controller, two of which are in phase, and the third is 180-degrees out of phase. This is manually constructed from the generated square waveform using a simple subtraction of 4095 (binary amplitude of square wave form) and a multiplication by -1. For square wave input values of 4095, this algorithm outputs 0. For the square waveform minimum value of 0, this algorithm outputs 4095. This approach significantly reduces the number of input settings.

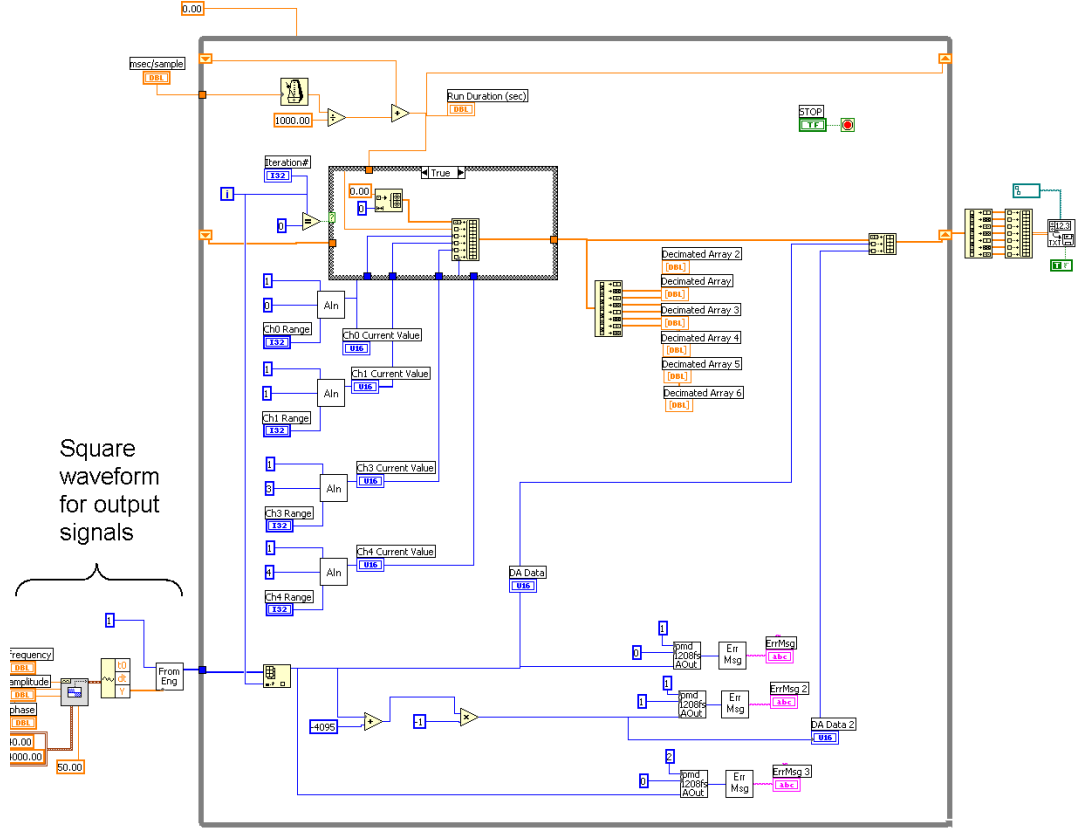


Figure B.4: Screen capture of LabVIEW program developed for hybrid actuator control (unidirectional fluid pump).

B.2 Finite Element Modeling

The program used for all magnetic finite element analysis is Finite Element Method Magnetics (FEMM) version 3.4. It was used in this study to calculate the magnetic flux through the MR fluid valve design. Every model created was a 2-dimension, y-axis symmetric sketch with defined material properties, boundary conditions, and mesh sizes.

To begin modeling, a semi-circle with the flat face vertical and left must be created as shown in Fig. B.5. The flat surface is the axis of revolution, and the curved surface sweeps the enclosed volume to be solved. According to the program guide, the boundary properties for this swept sphere should have a c_0 coefficient of 1693498 to represent infinite

Material	Relative μ_r	Relative μ_f
MR Fluid	0.11459	0.11459
Aluminum, 1100	1	1
Air	1	1
26 AWG (magnet wire)	1	1
Steel, 1018	529	529

Table B.1: Magnetic properties assigned to material definitions in FEMM.

space. To further avoid result distortion due to boundary conditions, the part of interest, shown in Fig. B.6, should be sufficiently far from the external boundaries.

All material properties, except MR fluid, are defined in the FEMM library of materials. For consistency, the MR fluid was defined identical to that of the original FEMM analysis performed by Brett Burton, as shown in Table. B.1. These values are from the linear B–H (magnetic induction–magnetic field) relationship of the respective material.

Solenoids were created by assigning the material property 26 AWG to a 2-D element, and subsequently adding the element to an electrical circuit. To create the alternating directions of current flow, two circuits were constructed and labeled “minus” and “plus.” Equal but opposite amperage (± 10 A) was applied to each circuit to turn “on” the solenoid during the finite element solving process. To turn all solenoids “off” during a run, the amperage was reduced to zero.

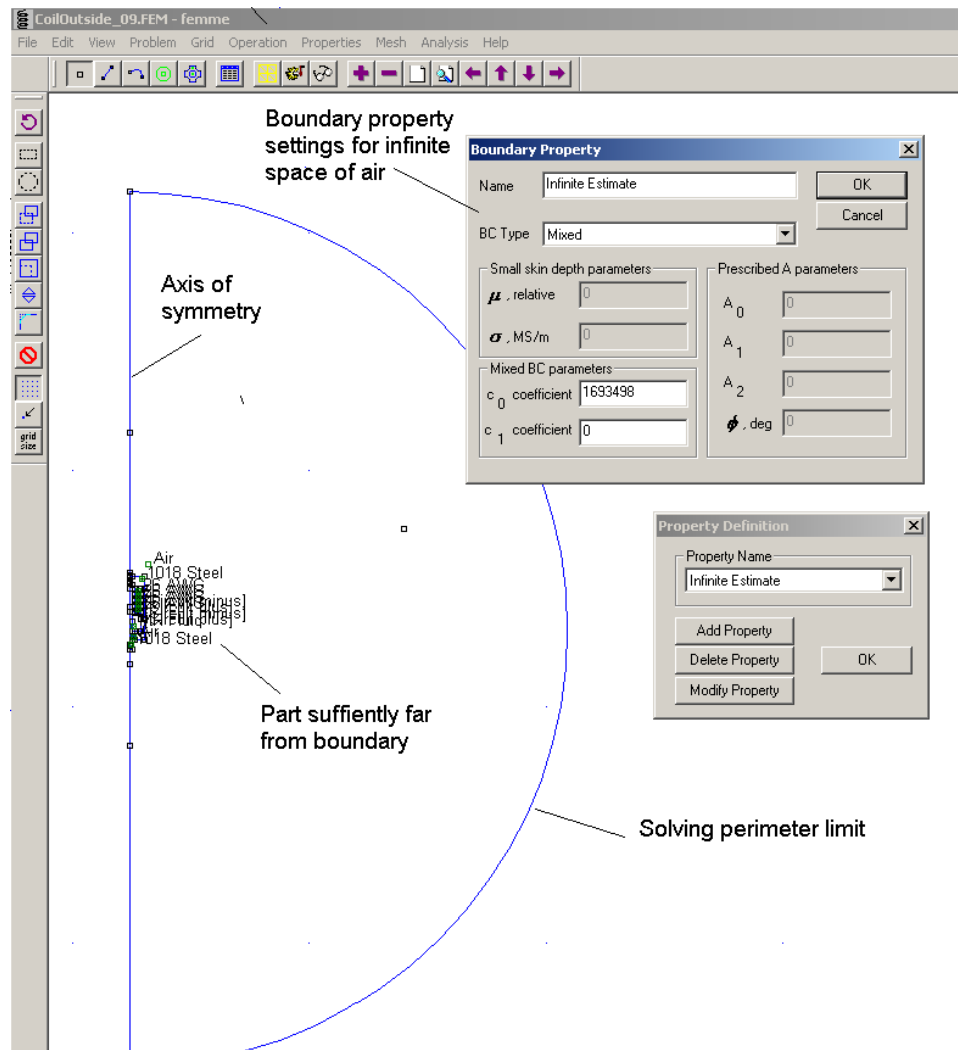


Figure B.5: Screen capture of FEMM solver boundaries.

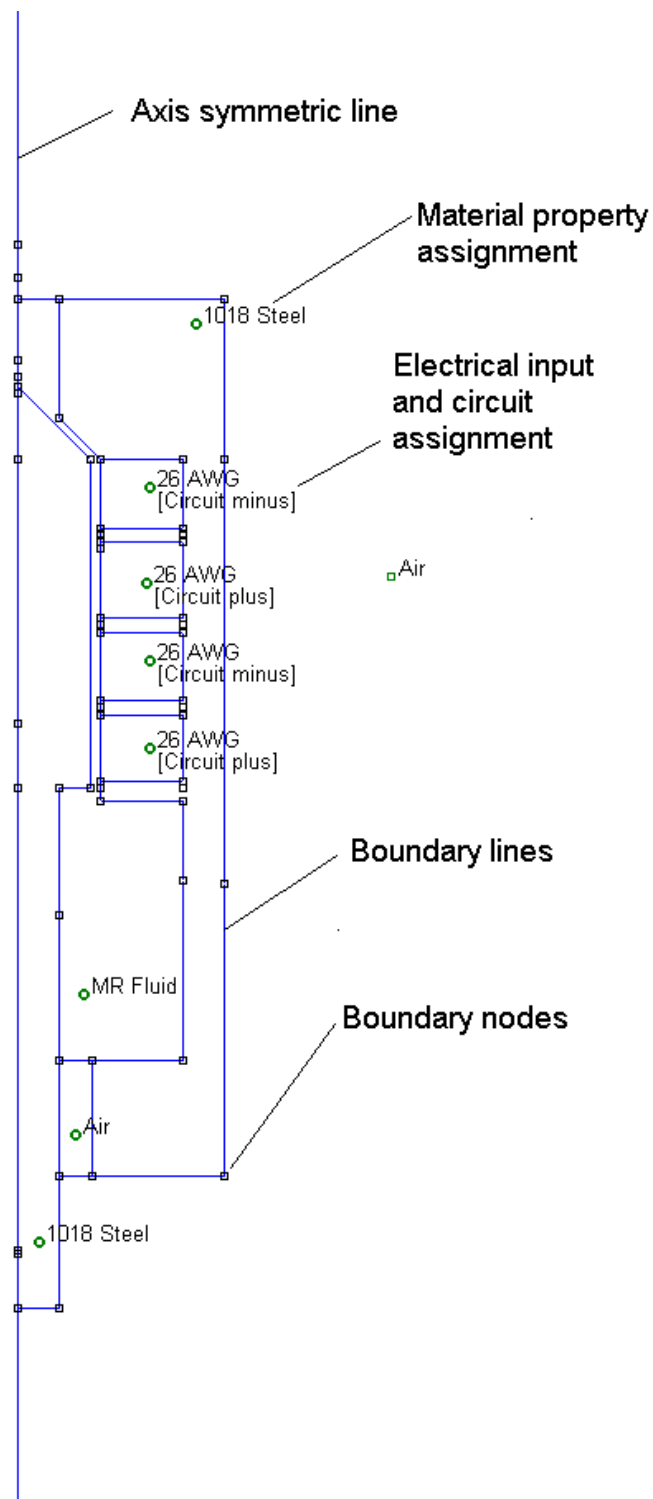


Figure B.6: Screen capture showing details of an actual FEMM model.

B.3 Matlab

B.3.1 System Model #1 Details

This section provides additional details of the Matlab-Simulink programming of system-level model #1. The equation set was divided into five sets to facilitate viewing and troubleshooting. Fig B.7 is the outer program which contains three subprograms and one sub-subprogram. The four user defined inputs are produced from signal generator blocks with the appropriate magnitude and phase. Table B.2 provides the settings used in the results presented previously in Fig.5.3. These inputs are routed to the valve fluid resistance subprogram and flow routing subprogram.

The valve fluid resistance subprogram is shown in Fig.B.8. This subprogram uses inputs of voltage and valve position to determine the fluid resistance through the valve by means of a look-up table. The approximated values are summarized in Table B.3 for the left valve. The right valve look-up table uses identical numerical values, but with the maximum closure resistances occurring at $+0.25$ in. It is noted that closure occurs at 0.25 in from the center location. The ± 0.50 in from center range is to assure interpolation between defined values.

The fluid routing subprogram is shown in Fig. B.9. This block inputs MR total volume flow quantities along with the variable valve resistance values. Using the flow divider equations previously presented, flow rate quantities through the two paths, left and right, are calculated.

The third subprogram within the main program shell is the mechanical valve system shown in Fig.B.10. This subprogram combines all force equations which act on the fluid valve. A low-pass filter was added to smooth the step response change in frictional forces due to the highly oscillatory direction changes when the valve closes. The non-linear spring

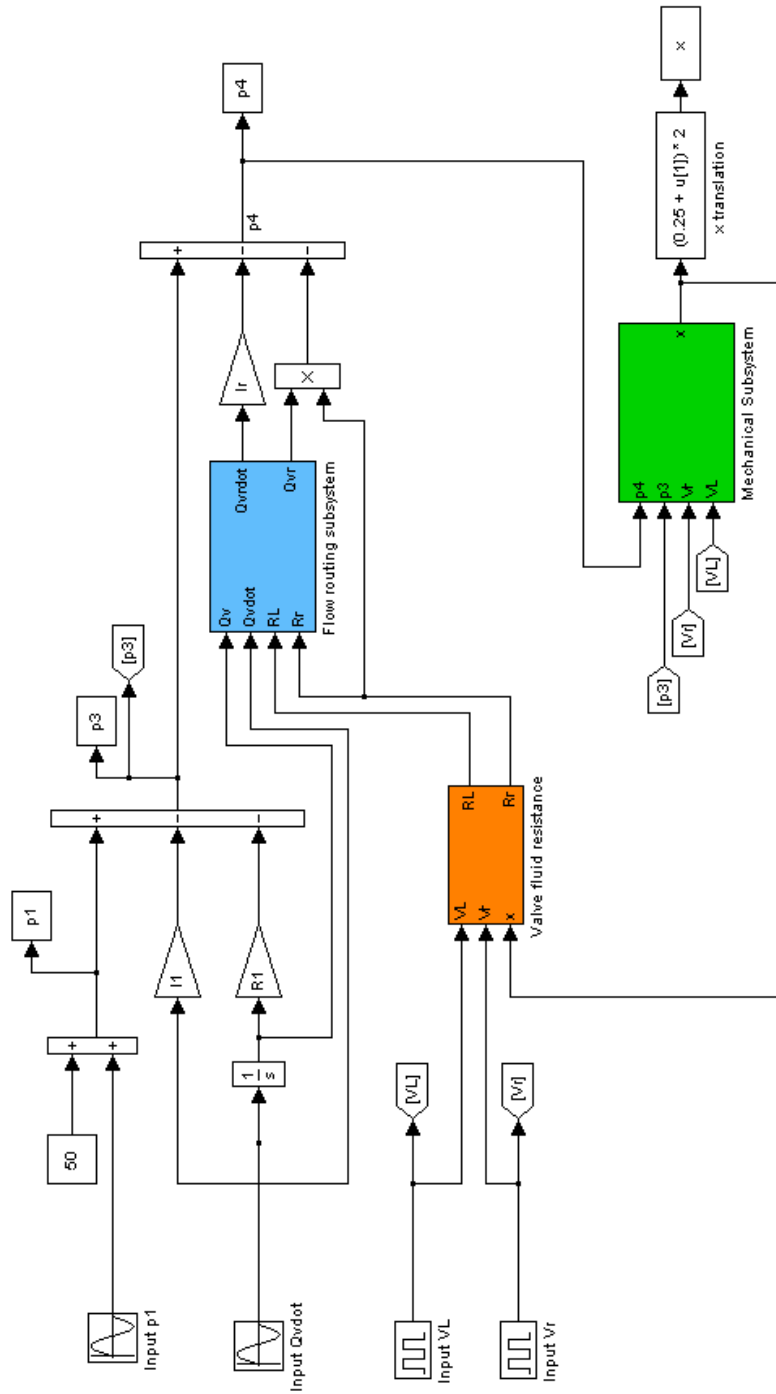


Figure B.7: Outside program shell for system-level model #1, with 3 subprograms (Valve fluid resistance, Flow routing, and Mechanical).

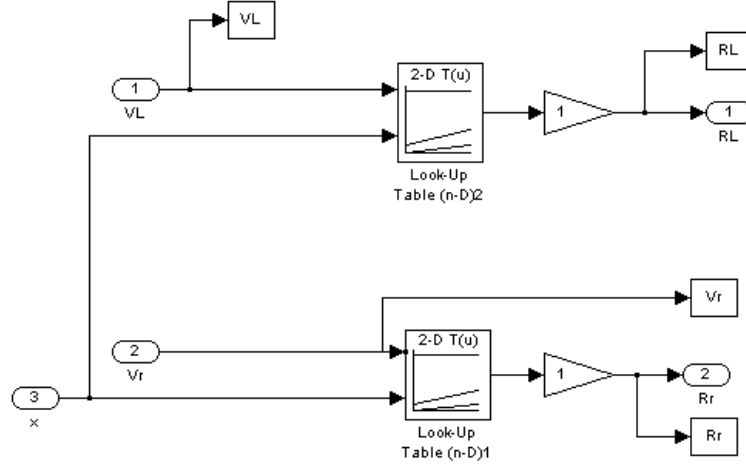


Figure B.8: Valve fluid resistance subprogram for system-level model #1.

Input	Waveform	Magnitude	Phase
Pressure, p_1	sine	50	$3 \pi/2$
Flow rate, \dot{Q}_v	sine	1	$\pi/2$
Left solenoid voltage, V_L	square	1	π
Right solenoid voltage, V_r	square	1	0

Table B.2: System inputs for model #1.

and damper have significant effects in close proximity to the rigid housing constraints, and minimal effect elsewhere. The highly nonlinear coefficients are summarized in Table B.4.

The valve shear forces produced by flowing fluid are calculated from the fourth subprogram labeled damping coefficients. This program is shown in Fig. B.11. The inputs are valve velocity and input voltage. The input voltage is assigned a corresponding magnetic field. The magnetic induction and valve velocity are used with best-fit approximations of previously presented data in Fig. 2.5 to calculate the yield and shear stress. After a unit conversion to remain consistent and multiplication by the effective shear area, the output forces are sent back to the mechanical system.

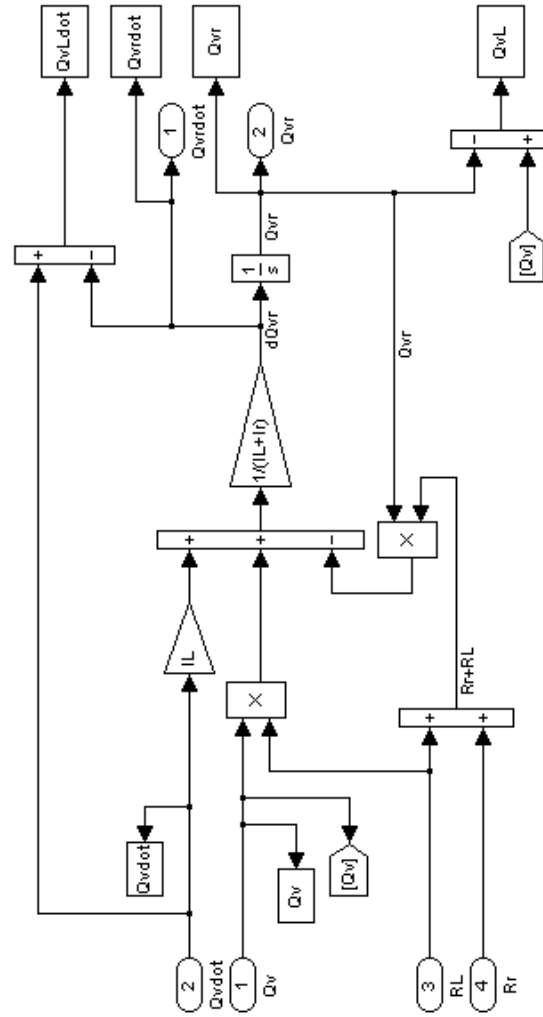


Figure B.9: Flow routing subprogram for system-level model #1.

To simplify variable assignments and program execution, the script file shown in Fig. B.12 was developed. The displayed values are those used in presented data.

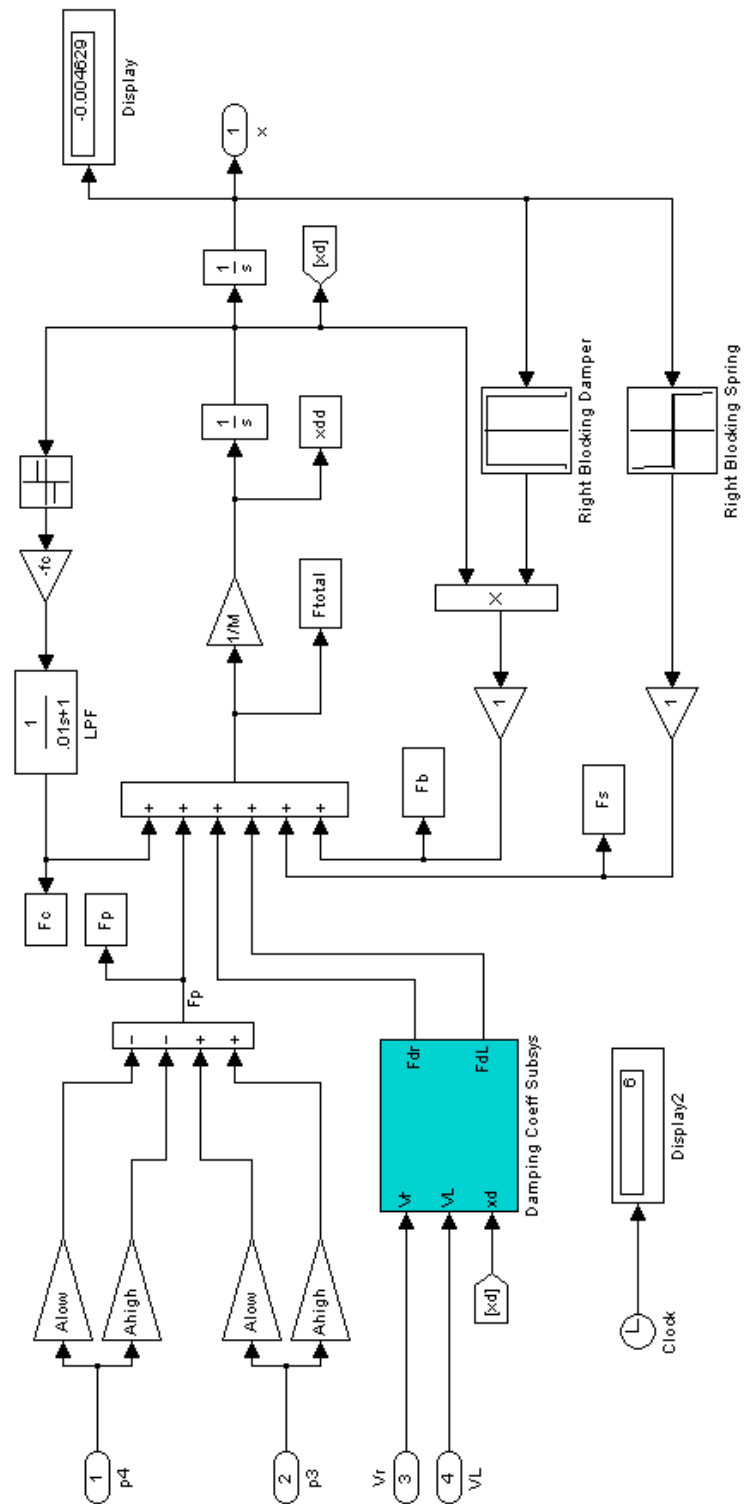


Figure B.10: Mechanical subprogram for system-level model #1, with 1 subprogram (damping coefficients).

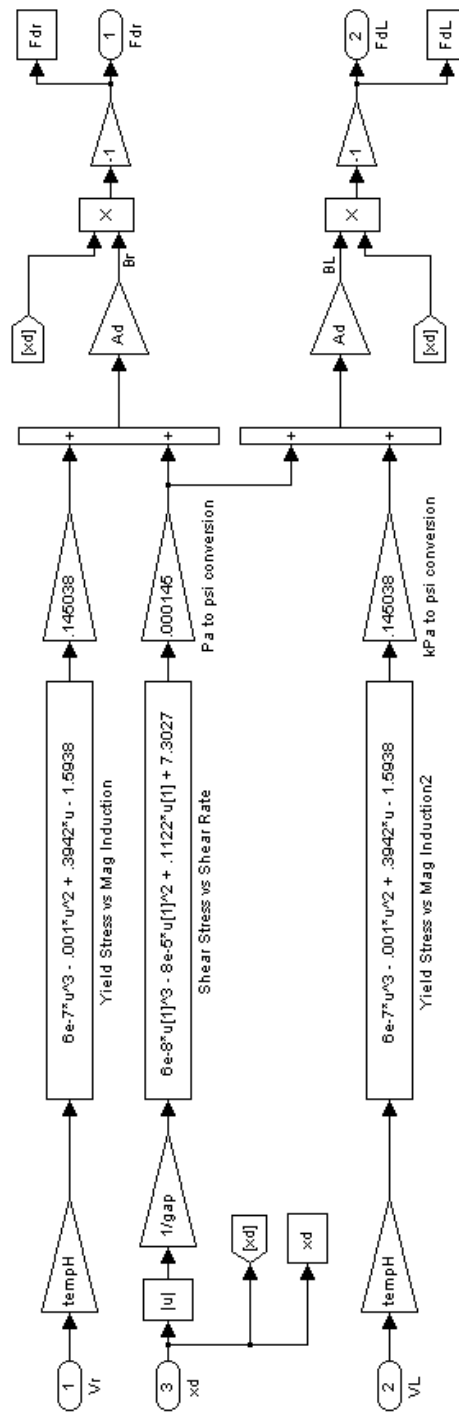


Figure B.11: Damping coefficients subprogram for system-level model #1, using the Bingham viscoplastic model.

	Valve Position (in)				
Voltage Input	-.50	-.25	0.00	+.25	+.50
On, 1	8000	8000	1000	100	100
Off, 0	8000	8000	3000	1000	1000

Table B.3: Relative approximations for variable left valve resistances. The right valve is similar.

Valve Position, y	-.26	-.24	-.235	+.235	+.24	+.26
Spring Coefficient, $k(y)$	10000	5000	5	0	5	-10000
Damping Coefficient, $c(y)$	-10	-10	0	0	10	10

Table B.4: Spring and damper (rigid housing constraint) look-up table values.

```

1  %%%%%%%%%%%%%%%%%%%%%%%%%%%%%%%%%%%%%%%%%%%%%%%%%%%%%%%%%%%%%%%%%%%%%%%%%
2  % Dave Nosse
3  % Script to run DEV SIMULINK Simulation
4  % Revised Date: 2004 April 25
5  %%%%%%%%%%%%%%%%%%%%%%%%%%%%%%%%%%%%%%%%%%%%%%%%%%%%%%%%%%%%%%%%%%%%%%%%%
6
7  close all; clear all; clc;
8
9  %%% Model parameters based off of experimental model %%%
10 f = 1; % System input frequency [Hz]
11 amp = 1;
12
13 Ap = (1^2)*pi/4; % Hydraulic piston C.S. area [in*in]
14 Ahigh = pi/4*((1.505)^2-(7/8)^2); % Mechanical system projected pressure surface areas
15 Alow = pi/4*(1.505)^2;
16 Ad = 2*pi*1.505; % Damping (Shear) surface area = circum.*length
17 M = .33; % Mass of valve rod [slugs]
18
19 I1 = 1.225; % Inertia approximations (line 1, 2, left valve and right valve)
20 I2 = 1.791;
21 IL = 2.167;
22 Ir = 2.167;
23
24 R1 = 56.6; % Flow resistance approximations
25 R2 = 82.8;
26
27 gap = .03; % Distance between cylindrical valve end and main housing
28
29 tempH = 30; % H created from voltage application input
30 fc = 30; % Coulomb friction coefficient
31
32 %%% Run Simulation %%%
33
34 sim DEV_Model_1_4
35

```

Figure B.12: Script file used to run Simulink program for system-level model #1 with defined coefficients

B.3.2 System Model #2 Details

This section provides additional details of the Matlab-Simulink programming of system-level model #2. Similar to model #1, the equation set was divided to facilitate viewing and troubleshooting. Fig B.13 is the outer program which contains three subprograms. The four user defined inputs are produced from signal generator blocks with the appropriate magnitude and phases. Table B.5 provides the settings used in the results presented in Fig.5.6. These inputs are routed to the valve fluid resistance subprogram and flow routing subprogram.

The valve resistance subprogram is shown in Fig. B.14. The major difference between this subprogram and that of model #1, is the addition of a flow direction dependance to the left valve. Only the left valve was given this dependance because the left valve is solely responsible for enforcing the motion constraints. Assigning the following values per condition,

$$V_L(on) = +1,$$

$$V_L(off) = 0,$$

$$|Qv_L|(+) = 0,$$

$$|Qv_L|(-) = +2,$$

the four combinations of voltage and flow direction produce look-up table index numbers ranging from 0–3 as summarized in Table B.6. The corresponding variable valve resistance look-up table is shown in Table B.7. It is noted most values are from the experimental results presented in Sect. 4.3. Only the order of magnitude larger resistance values were model approximations to simulate rigid constraints.

The flow divider subprogram is shown in Fig. B.15. This system of equations is essentially identical to that presented for model #1. The third subprogram models both the valve position and output piston position through volume stored calculations, as shown in

Input	Waveform	Magnitude	Phase
Force, F_1	sine	100	0
Acceleration, \ddot{x}	sine	10	$\pi/2$
Left solenoid voltage, V_L	square	1	0
Right solenoid voltage, V_r	square	0	π

Table B.5: System inputs for model #2.

Voltage Input, V_L	Direction Qv_L	Table Index
Off, 0	(+), 0	0
On, 1	(+), 0	1
Off, 0	(-), 2	2
On, 1	(-), 2	3

Table B.6: Variable left valve resistance look-up table index numbers based on flow direction and solenoid voltage.

Table Index	Valve Position						
	-.20	-.18	-.1025	-.075	+.05	+.18	+.20
0	500	50	12	12	12	12	12
1	750	75	46	53	50	40	40
2	50	12	12	12	12	12	12
3	75	75	46	53	50	40	40

Table B.7: Relative approximations for variable left valve resistances. The right valve is similar.

Fig. B.16. Through elementary math and calculus operations, the respective quantities are easily solved.

To simplify variable assignments and program execution, the script file shown in Fig. B.17 was developed. The displayed values are those used in presented data.

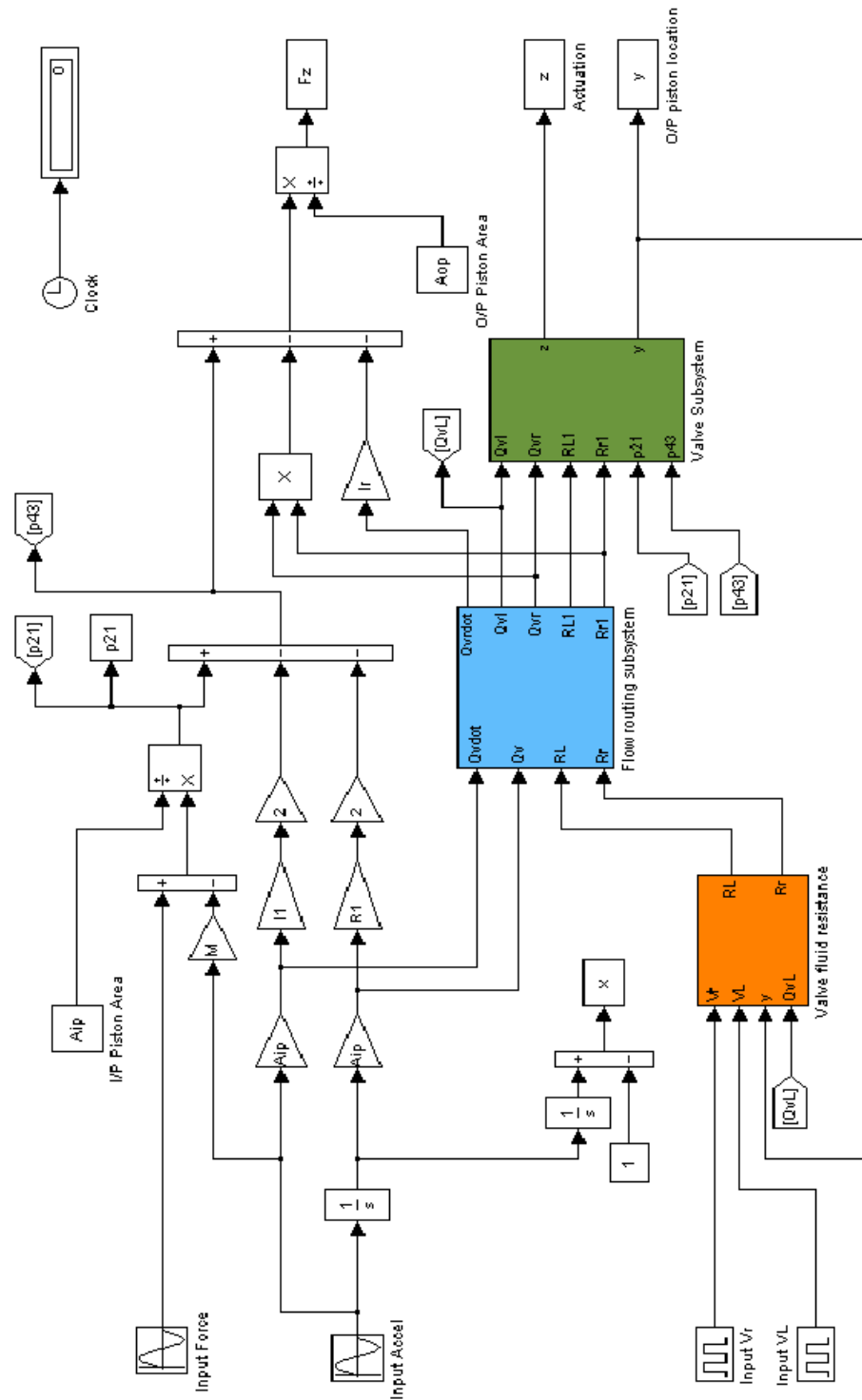


Figure B.13: Outside program shell for system-level model #2, with 3 subprograms (Valve fluid resistance, Flow routing, and Valve subsystem).

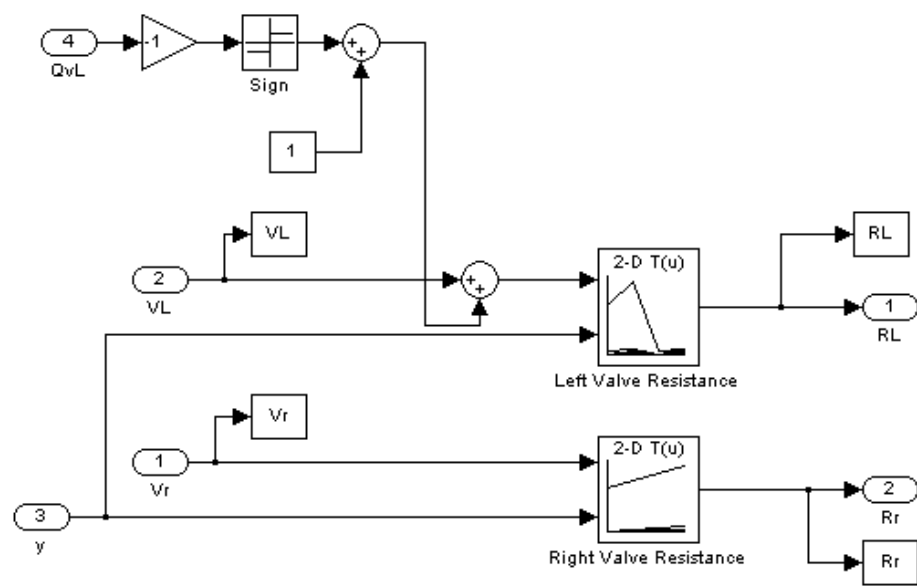
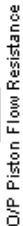


Figure B.14: Valve fluid resistance subprogram for system-level model #2.



136

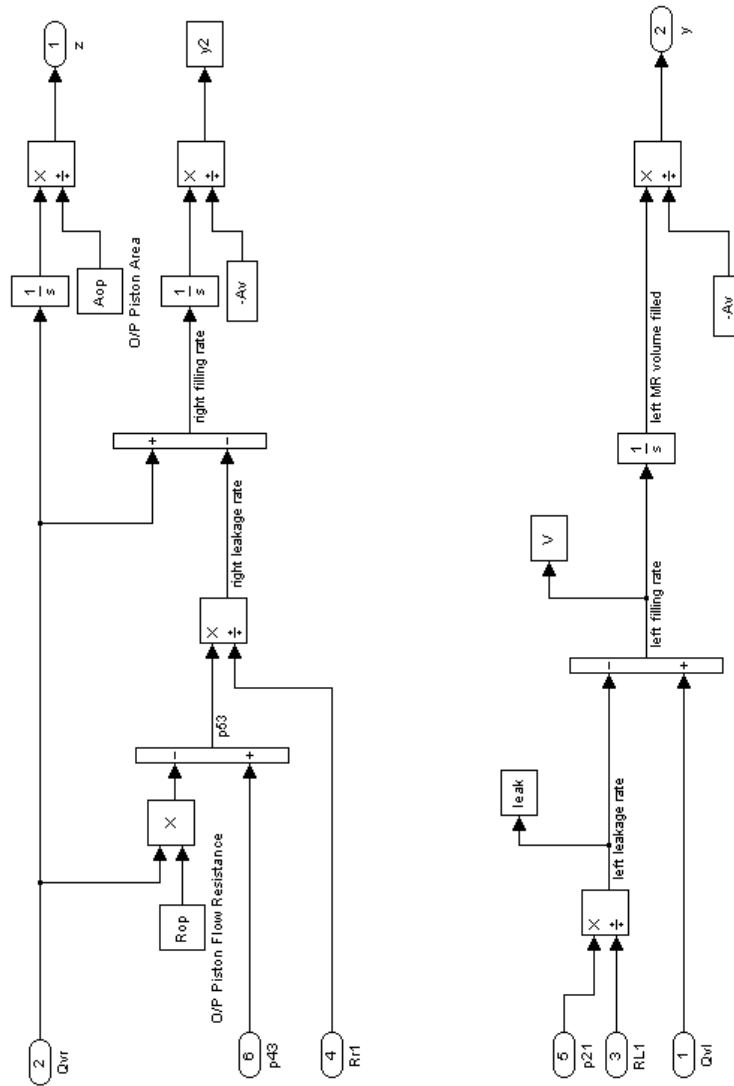


Figure B.16: Valve motion subprogram for system-level model #2.

```

4 - close all; clear all; clc;
5
6 - Aip = (pi/4)*(1.5^2 - (7/16)^2);           % Input piston area
7 - Av  = (pi/4)*(1.5^2 - (7/8)^2);           % Valve CS area
8 - Aop = (pi/4)*(0.875^2 - (.25)^2);         % Output piston area
9
10 - I1 = 0.63;                                % Inertia approximations (line 1, 2, left valve and right valve)
11 - I2 = 0.63;
12 - IL = 2.167;
13 - Ir = 2.167;
14
15 - R1 = 20;                                   % Flow resistance approximations
16 - R2 = 20;
17 - Rop = 18;
18
19 - M = .1;                                   % Mass approximation I/P piston
20
21 - %%% Run Simulation %%%
22 - f = 0.5;                                  % Frequency
23 - amp = 1;
24 - delay = 0;
25
26 - sim ActuatorModel_2_7
27

```

Figure B.17: Script file used to run Simulink program for system-level model #2 with defined coefficients

BIBLIOGRAPHY

- [1] T. Akuta. “Rotational type actuators with Terfenol-D rods”. In *Proc. 3rd Inter. Conf. New Actuators*, pages 244–248, Bremen, Germany, 1992.
- [2] K. Bridger, J. M. Sewell, A. V. Cooke, J. L. Lutian, D. Kohlhafer, G. E. Small, and P. M. Kuhn. “High-pressure magnetostrictive pump development: a comparison of prototype and modeled performance”. In E. H. Anderson, editor, *Smart Structures and Materials 2004: Industrial and Commercial Applications of Smart Structures Technologies*, volume 5388 of *Proc. SPIE*, pages 246–257, 2004.
- [3] J. L. Butler, S. C. Butler, and A. L. Butler. “Hybrid magnetostrictive/piezoelectric tonpilz transducer”. *Journal of the Acoustical Society of America*, 94:636–641, 1993.
- [4] F. T. Calkins, R. C. Smith, and A. B. Flatau. “Energy-based hysteresis model for magnetostrictive transducers”. *IEEE Transactions on Magnetics*, 36:429–439, 2000.
- [5] D. Carlson, D. M. Catanzarite, and K.A. StClair. “Commercial magneto-rheological fluid devices”. In W. Bullough, editor, *Proceedings 5th Inter. Conf. on ER fluids, MR suspensions and associated technology*, pages 20–28, 1996.
- [6] M. Dapino. ME794M course notes, 2005.
- [7] M. J. Dapino. “On magnetostrictive materials and their use in adaptive structures”. *Journal of Structural Engineering and Mechanics*, 17:303–329, 2004.
- [8] M. J. Dapino. “Magnetostrictive materials: their use in smart structure applications”. In M. Schwartz, editor, *Encyclopedia of Smart Materials*. John Wiley and Sons, 9999.
- [9] M. J. Dapino, R. C. Smith, and A. B. Flatau. “Structural magnetic strain model for magnetostrictive transducers”. *IEEE Transactions on Magnetics*, 36:545–556, 2000.
- [10] P. Downey. “Hybrid PMN-PT/Terfenol-D broadband transducers in mechanical series configuration”. Master’s thesis, The Ohio State University, Columbus, Ohio, 2003.
- [11] J. J. Epps and I. Chopra. “Comparative evaluation of shape memory alloy constitutive models with test data”. *38th American Institute of Aeronautics and Astronautics Structures*, 1997.
- [12] D. R. Gamota and F. E. Filisko. “Dynamic mechanical studies of electrorheological materials: moderate frequencies”. *Journal of Rheology*, 35:399–425, 1991.

- [13] J. C. Garcia. “Active helicopter rotor control using blade-mounted actuators”. Master’s thesis, Massachusetts Institute of Technology, 1994.
- [14] S. R. Hall, K. Y. Yang, and K. C. Hall. “Helicopter rotor lift distributions for minimal induced power loss”. *Aircraft*, 31:837–845, 1994.
- [15] M. R. Jolly, J. W. Bender, and J. D. Carlson. “Properties and applications of commercial magnetorheological fluids”. In L. Porter Davis, editor, *Smart Structures and Materials 1998: Passive Damping and Isolation*, volume 3327 of *Proc. SPIE*, pages 262–275, 1998.
- [16] H. J. Jung, B. F. Spencer Jr, Y. Q. Ni, and I. W. Lee. “State-of-the-art of semiactive control systems using MR fluid dampers in civil engineering applications”. *Journal of Structural Engineering and Mechanics*, 2002.
- [17] C. Kormann, M. Laun, and G. Klett. In H. Borgmann and K. Lenz, editors, *4th Inter. Conf. on New Actuators*, volume 271 of *Actuator 94*, 1994.
- [18] L. Kvarnsjo. “On characterization, modeling, and application of highly magnetostrictive materials”. PhD thesis, Royal Institute of Technology, Stockholm Sweden, 2003.
- [19] D. G. Lee, S. Wing, and G. P. Carman. “Design of a piezoelectric-hydraulic pump with active valves”. *Journal of Intelligent Material Systems and Structures*, 15:107–115, 2004.
- [20] L. D. Mauck and C. S. Lynch. “Piezoelectric hydraulic pump development”. *Journal of Intelligent Material Systems and Structures*, 11:758–764, 2000.
- [21] J. E. Miesner and J. P. Teter. “Piezoelectric/magnetostrictive resonant inchworm motor. In *Proc. of SPIE*, pages 520–527, 1994.
- [22] T. A. Millot and P. P. Friedmann. “Vibration reduction in helicopter rotors using actively controlled partial span trailing edge flap located on the blade”. Technical Report 4611, NASA, 1994.
- [23] J. Park, G. P. Carman, and H. T. Hahn. “Design and testing of a mesoscale piezoelectric inchworm actuator with microridges”. *Journal of Intelligent Material Systems and Structures*, 11:671–684, 2000.
- [24] E. F. Prechtel and S. R. Hall. “Design of high efficiency, large stroke, electromechanical actuator”. *Smart Materials and Structures*, 8:13–30, 1999.
- [25] I. H. Shames and F. A. Cozzarelli. “*Elastic and inelastic stress analysis*”. Taylor and Francis, 1997.
- [26] J. L. Shearer, B. T. Kulakowski, and J. F. Gardner. “*Dynamic modeling and control of engineering systems*”. Prentice Hall, 2nd edition edition, 1997.

- [27] J. Sirohi and I. Chopra. “Design and development of a high pumping frequency piezoelectric-hydraulic hybrid actuator”. *Journal of Intelligent Material Systems and Structures*, 14:135–147, 2003.
- [28] R. Smith. “*Smart material systems: model development*”. Frontiers in applied mathematics, 2005.
- [29] B. F. Spencer, S. J. Dyke, M. K. Sain, and J. D. Carlson. “Phenomenological model of a magnetorheological damper”. In *Journal of Engineering Mechanics, ASCE*, volume 123, pages 230–238, 1997.
- [30] R. Venkataraman, W. P. Dayawansa, and P. S. Krishnaprasad. “The hybrid motor prototype: design details and demonstration results”. Technical Report CDCSS T.R. 98-2, University of Maryland, 1998.
- [31] R. Wall. “DARPA eyes materials for ‘morphing’ aircraft”. *Aviation Week and Space Technology*, April 2004.
- [32] G. Washington. ME774 course notes, 2004.
- [33] G. Yang. “*Large-scale magnetorheological fluid damper for vibration mitigation: modeling, testing and control*”. PhD thesis, Univ. of Notre Dame, Notre Dame, Indiana, 2001.
- [34] J-H. Yoo, J. Sirohi, N. M. Wereley, and I. Chopra. “A magnetorheological hydraulic actuator driven by a piezopump”. In *Proc. of IMECE*, 2003.
- [35] J-H. Yoo and N. M. Wereley. “Performance of a magnetorheological hydraulic power actuation system”. *Journal of Intelligent Material Systems and Structures*, 15:847–857, 2004.